UNIVERSITÀ DEGLI STUDI DELL'INSUBRIA

Facoltà di Scienze Matematiche, Fisiche e Naturali - Como

Anno Accademico 2011-2012

Laurea Specialistica in Fisica

SILICON PHOTOMULTIPLIERS FOR TOTALLY ACTIVE SCINTILLATING DETECTORS

Laura Stoppani
Matricola 703464

Tutor:	Dr.ssa Michela Prest
	Università degli Studi dell'Insubria
Co-tutor:	Dr. Alessandro Berra
	Università degli Studi dell'Insubria

A te, Pins

Contents

Riassunto della tesi

In diversi campi della fisica, dalla fisica delle alte energie alla fisica dello spazio, la rivelazione di luce rappresenta uno degli elementi chiave di molti esperimenti: le particelle cariche possono infatti essere rivelate tramite il deposito di parte della loro energia in materiali in grado di produrre a loro volta fotoni nella regione del visibile e dell'ultra-violetto. Questi fotoni devono poi essere rivelati da un $photodetector$, un dispostivo in grado di convertire la luce in un segnale elettrico.

Rutherford, durante il suo esperimento per lo studio della struttura interna del nucleo, utilizzò il primo photodetector della storia della fisica delle particelle: l'occhio umano. Successivamente, nel 1913 fu inventato il primo tubo fotoelettrico da Elster e Geitel e ci vollero ben 20 anni prima che il primo fotomoltiplicatore fosse prodotto e lanciato sul mercato; ad oggi i fotomoltiplicatori sono tra i rivelatori di luce più diffusi nella fisica delle alte energie. Tuttavia, nuovi photodetector caratterizzati da un ampio range dinamico, dalla capacità di lavorare anche in presenza di campi magnetici e da un basso costo saranno necessari per gli esperimenti di nuova generazione.

Sono proprio queste richieste che hanno portato allo sviluppo di sistemi di rivelazione di luce alternativi ai fotomoltiplicatore (PMT): i cosiddetti photodetector a stato solido. Tra questi nuovi photodetector i Silicon PhotoMultiplier (SiPM) rappresentano l'alternativa più valida ai PMT. Il SiPM è una matrice di pixel (tipicamente la densità è di 500-4000 pixel/mm^2) con dimensioni variabili tra i 20 e i 200 μm e connessi in parallelo ad un unico output comune. Ogni pixel è indipendente dagli altri e lavora come un Single Photon Avalanche Photodiode (SPAD) nella cosiddetta zona di Geiger Mode limitata: in altre parole, ogni pixel rappresenta un device binario (o digitale) in quanto produce un segnale non proporzionale all'energia rilasciata dal fotone, ma ne registra solamente il passaggio. L'informazione analogica viene riottenuta (per un numero limitato di fotoni) dalla somma dei segnali di tutti i pixel, la quale risulta essere proporzionale al numero di pixel colpiti e dunque all'energia depositata dalla particella incidente.

Come mostrato nel capitolo 1 (nel quale le strutture e i principi di funzionamento dei diversi photodetector vengono descritti), i principali vantaggi dei SiPM rispetto ai PMT sono:

- un elevato fattore di guadagno (dell'ordine di 10^6);
- un'alta efficienza di rivelazione, compresa tra il 25% e il 50%;
- una tensione di alimentazione dell'ordine delle decine di V (che deve essere confrontata con quella necessaria ai PMT che è dell'ordine dei kV);
- un'ottima risoluzione temporale (inferiore al ns);
- la capacità di operare anche in presenza di campi magnetici.

I principali limiti di questi dispositivi sono rappresentati da un elevato rate di conteggi di buio (che per il singolo fotone è dell'ordine del MHz in confronto a quello del PMT solitamente inferiore al kHz) e dal basso fill factor (definito come il rapporto tra l'area attiva del detector e la sua area geometrica). Diversi gruppi di ricerca stanno studiando la possibilità di superare questi limiti, che annoverano anche una limitata radiation hardness, per procedere al disegno di nuovi dispositivi caratterizzati da grande range dinamico, basso rumore e capacità di rivelazione nell'UV. Tra questi gruppi vi è la collaborazione italiana FACTOR (Fiber Apparatus for Calorimetry and Tracking with Optoelectronic Read-out) ora diventata TWICE (Techniques for Wide-Range Instrumentation in Calorimetry Experiments) finanziata dall'Istituto Nazionale di Fisica Nucleare. Il progetto si avvale di un'attiva collaborazione con FBK-irst (Fondazione Bruno Kessler) per lo sviluppo e la produzione di nuove tipologie di SiPM per applicazioni in ambito di fisica delle alte energie e dello spazio.

Questo lavoro di tesi si è svolto nell'ambito della collaborazione FACTOR/ TWICE con lo scopo di valutare le performance di un elevato numero di SiPM ($\sim$200) e confrontare il loro comportamento con quello di fotomoltiplicatori multianodo (MAPMT). Per i test presentati in questa tesi sono stati utilizzati due diversi prototipi dell'Electron Muon Ranger (il calorimetro/tracciatore per l'identificazione di elettroni e muoni dell'esperimento MICE), entrambi costituiti da barre scintillanti estruse lette da MAPMT e SiPM. I segnali dei due diversi sistemi di rivelazione di luce sono stati processati attraverso una FrontEnd Board il cui elemento principale è l'ASIC MAROC (Multi Anode ReadOut Chip), un ASIC inizialmente progettato per la lettura di MAPMT a 64 canali ma che può adattarsi anche alla lettura di SiPM. Questo ASIC è in grado di fornire contemporaneamente un'uscita multiplexata analogica e 64 segnali digitali: ogni canale consiste in un pre-amplificatore con guadagno variabile, due shaper (uno per i segnali analogici e l'altro per quelli digitali), un circuito di sample&hold e un discriminatore.

Nel capitolo 3 di questa tesi vengono presentati i risultati dei test con raggi cosmici del prototipo di EMR di piccole dimensioni, che è un rivelatore formato da 8 piani (posti in configurazione $x - y$) di 10 barre a sezione rettangolare. Durante questi test, 8 barre del primo piano sono state interfacciate ad un doppio sistema di rivelazione di luce basato su un fotomoltiplicatore a 64 canali dell'Hamamatsu e 8 SiPM da 1 mm di diametro prodotti da FBK-irst. I risultati dell'analisi dati hanno mostrato un peggiore rapporto segnale rumore nel caso dei SiPM dovuto all'elevato rumore intrinseco di questi photodetector, mentre sono stati ottenuti valori comparabili sia in termini di risoluzione spaziale ($\sim$6.8 mm) che di efficienza di rivelazione (stimata essere dell'ordine del 94%). Per quanto riguarda la risoluzione temporale, il valore misurato è dell'ordine di 2.5 ns in entrambi i casi: tuttavia, questo risultato deve essere considerato come un limite superiore in quanto è la somma di diversi fattori come la risoluzione intrinseca dei photodetector, le caratteristiche temporali dello scintillatore e delle fibre e anche il tempo di processamento dell'elettronica. La migliore risoluzione temporale intrinseca dei SiPM è stata dimostrata misurando la differenza dei tempi di arrivo della luce dalle due diverse estremità delle barre.

Il cuore di questo lavoro di tesi è rappresentato dello studio delle performance dei 192 SiPM di LEP: infatti, questo rivelatore è costituito da 192 barre (organizzate in 48 piani) interfacciate a 3 MAPMT a 64 canali (da una parte) e a 192 SiPM prodotti da FBK-isrt con un diametro di 2.8 mm (dall'altra). Nel capitolo 4 viene presentata la procedura di assemblaggio del detector e la fase di commissioning durante la quale le prime 64 barre di LEP sono state testate con raggi cosmici. In questa fase sono state valutate le diverse impostazioni dei parametri dell'ASIC e si è ottenuta una buona stabilità dell'intero sistema. Dopo questa prima fase, il prototipo è stato testato con un fascio di pioni, muoni ed elettroni da 6 GeV/c su una linea estratta del CERN e caratterizzato in termini di risoluzione spaziale ed efficienza di rivelazione come viene mostrato nel capitolo 5 di questa tesi. In particolare, si sono misurati valori di risoluzione spaziale compresi tra 4.0 e 7.5 mm per tutti i 48 piani di LEP e ne è stato osservato un peggioramento all'aumentare del numero di layer (effetto dovuto al multiplo scattering). Un'efficienza superiore al 97% è stata misurata per tutti i piani nel caso dei fotomoltiplicatori, mentre per i SiPM si è osservata un perdita di efficienza nei piani dell'ultimo blocco: in ogni caso, tutti i piani presentano un'efficienza superiore al 90%.

Questo calo di efficienza di rivelazione dei SiPM è da imputare principalmente all'elevato rumore di questi photodetector interfacciati con l'ASIC MAROC: come dimostrato dai risultati presentati in questa tesi, cambiando i diversi parametri dell'ASIC (come ad esempio le impostazioni del circuito di feedback dello shaper) è possibile aumentare il rapporto segnale rumore dei SiPM. Per questo motivo, l'idea alla base dello sviluppo futuro è la modifica dell'elettronica basata sull'ASIC MAROC in modo da ottimizzarne le caratteristiche nel caso di segnali provenienti da SiPM. Parallelamente, nuovi test verranno condotti su un nuovo tipo di ASIC, specificatamente sviluppato per la lettura dei SiPM e chiamato EASIROC (Extended Analogue Si-pm Integrated ReadOut Chip). I principali vantaggi di questo

ASIC sono un ampio range dinamico (che permette di risolvere i problemi di saturazione) e la possibilità di aggiustare la tensione di overvoltage di ogni singolo canale.

Introduction

Light detection is one of the key elements in many experimental physics fields, from high-energy physics to astro-particle and medical physics: particles deposit energy in materials which in turn produce photons in the UV/visible range that can be detected by photodetectors. The first photodetector for particle physics was the human eye in Rutherford's experiment for the nucleus discovery to see the light produced by alpha particles hitting a ZnS detector once scattered by a gold foil. In 1913 Elster and Geitel invented the first photoelectric tube but then it took more than 20 years for the first PhotoMultiplier Tube (PMT) to be produced by the RCA laboratories in 1936 and put on the market. If on one hand, PMTs are at present the most widespread photodetectors, on the other the new generation experiments requirements are increasingly demanding from the point of view of large dynamic range, insensitivity to magnetic fields and low cost given the large volumes involved. These requirements can be met by solid state photodetectors which are becoming an alternative to the standard photodetector.

Among these new photodetectors, Silicon PhotoMultipliers (SiPMs) represent the solid state alternative to the PMTs. A Silicon PhotoMultiplier is a semiconductor device consisting of a matrix of pixels (whose typical dimensions are in the 20-200 μm range) joined together in parallel on a common Silicon substrate. Each SiPM pixel works as an independent Single Photon Avalanche Photodiode (SPAD) operated in limited Geiger mode; the sum of all the SiPM pixels outputs is proportional to the number of fired pixels and thus to the energy deposited by the particle. The main advantages of SiPMs compared to PMTs are a high internal gain (of the order of 10^6), a very low bias voltage, a very good time response (below 1 ns) and the insensitivity to magnetic fields.

Several research groups are working on the improvement of the SiPM features (in terms of noise, detection efficiency and radiation hardness) and on the design of new devices for dedicated applications such as the ones requiring large dynamic range and UV detection. Among these groups, the FACTOR (Fiber Apparatus for Calorimetry and Tracking with Optoelectronic Read-out) collaboration (now TWICE, Techniques for Wide-Range Instrumentation in Calorimetry Experiments) is being supported by the Italian Institute of Nuclear Physics for the development of scintillator systems readout by SiPMs for space and high energy applications. The project actively collaborates with FBK-irst (Fondazione Bruno Kessler) for the SiPM design and production. This thesis work has been performed in the framework of the FACTOR/TWICE collaboration to evaluate the performance of a large number of SiPMs (~200) as a readout system for scintillating bars detectors and compare their behaviour with the Multi Anode PhotoMultiplier Tubes one. The tests have been performed with two different detectors, which are both prototypes of the MICE Electron Muon Ranger and have been developed by the Como/Trieste group. The first one (the small scale EMR prototype) has been assembled to study the EMR tracker capability, while the second one (the Large EMR Prototype, LEP) has been used to evaluate the EMR performance as a calorimeter.

The prototypes are based on scintillating bars whose light is carried out by WaveLength Shifter fibers and readout both by MAPMTs and SiPMs. The small scale EMR prototype consists of 8 layers in the $x - y$ geometry, each one composed by 10 19.1 cm long extruded scintillating bars with a rectangular cross-section of 1.9×1.5 cm^2. For the tests presented in this thesis, the first layer of the prototype has been equipped with a double readout system: the bars are readout on one side by a MAPMT and on the other by 8 1 mm diameter SiPMs manufactured by FBK-irst. The Large EMR Prototype consists of 48 planes of the same scintillating bars (4 per plane) organized in three blocks of 16 layers along one single orientation. The scintillating light is carried out by two 0.8 mm diameter WLS fibers which have been glued in the bar hole: on one side the fibers are interfaced with three Hamamatsu 64 channel MAPMTs, while on the other side with 192 2.8 mm diameter FBK-irst SiPMs. The readout electronics of the two prototypes is based on the EMR FrontEnd Board hosting the MAROC3 ASIC, which is the third version of the ASIC developed by the Omega group for the ATLAS luminometer. Each ASIC channel consists of a preamplifier with a variable gain, two shapers (a slow one for the analog readout and a fast shaper for the digital output), a sample&hold circuit and a discriminator. The MAROC3 ASIC provides one multiplexed analog output and 64 digital ones at the same time.

The first chapter of this thesis presents a brief review of photodetectors, starting from PhotoMultiplier Tubes and then concentrating on solid state ones.

In chapter 2 the mechanism of the light emission in scintillator materials (both inorganic and organic ones) is introduced focusing on the plastic scintillators given they are the ones used in this thesis work. In the second part of the chapter, three experiments based on scintillating bars detectors will be presented: the MINERνA experiment, the ASACUSA tracker and the neutrino beam monitor of the T2K experiment. This last experiment will be discussed in detail since all its detectors are based on scintillators readout by a large number of Silicon PhotoMultipliers.

Chapter 3, after a brief review of the MICE experiment, describes the small scale EMR prototype and the cosmic ray test results: the performance of the 8 SiPMs has been evaluated in terms of Signal to Noise Ratio, spatial resolution, detection efficiency and timing resolution.

Chapter 4 and 5 deal with the Large EMR Prototype from the assembly and the commissioning phases to the tests performed on the T9 beamline at the PS CERN East Area. Chapter 4 presents the analysis results of the preliminary tests performed with cosmic rays whose main goals were the study of the MAROC ASIC parameters setting and the evaluation of the system overall stability. After the commissioning phase, the prototype has been tested at CERN with a pion/muon beam of 6 GeV/c: chapter 5 describes the experimental setup, the data taking procedure and the analysis results in terms of spatial resolution and detection efficiency for all the 48 LEP layers comparing the performance of the two readout systems.

Chapter 1

The Photodetectors

In physics many applications need to detect a very small number of photons thus requiring the use of very sensitive photodetectors. Photomultiplier tubes are nowadays the most common light detectors in high energy physics thanks to their high gain, their robustness and their being easy to use. They are ideal to be coupled to plastic scintillators for very different applications ranging from particle physics (where they are used to generate the trigger or measure the time of flight) to neutrino physics (for the next generation totally active scintillating detectors) and medical physics (to develop scintillating fiber dosimeters).

However, in recent years an alternative to the photomultiplier tube has been proposed with the solid state photodetectors which are very compact, have a large enough gain and a high detection efficiency, a fast timing response and a low bias voltage. Moreover, they are insensitive to magnetic fields. Among these new photodetectors, Silicon PhotoMultipliers, the main topic of this thesis work, can be listed.

This chapter is an introduction to the different types of photodetectors. After having summarized the main features of an ideal photodetector, a detailed description of the structure of a typical PhotoMultiplier Tube and its working principle are presented (a more detailed description of PMTs can be found in [1–3]). In the second part of the chapter solid state photodetectors are introduced; for a detailed description see [4, 5].

1.1 The Ideal Photon-Electron Converter

The goal of a photodetector is to convert the incoming photons into a detectable electrical signal. In principle, an ideal photoconverter should have the following features:

- a high sensitivity, that is the capability to generate a detectable signal starting from a small number of photons, without the need of a preamplifier (which increases the noise);

- a good spectral matching between the incoming photons wavelength and the sensitivity of the photodetector window;
- a good timing resolution (typically of the order of a ns) and a small dead time to allow to detect a high rate of photons;
- magnetic field insensitivity;
- compactness and low cost.

There are several types of photodetectors on the market [6] which can be divided into two main categories:

- the vacuum photodetectors in which photons are converted into electrons through the photoelectric effect and multiplied via the secondary emission in dedicated electrodes biased at increasing voltages: the PhotoMultiplier Tube is the most representative example;
- the solid state photodetectors in which the electrons produced by the incident photons through the photoelectric effect are collected directly (no signal multiplication) or after the multiplication via a suitable mechanism. This category, in fact, features both PIN diodes (without any signal multiplication) and the Avalanche PhotoDiodes and the Silicon PhotoMultipliers (where the avalanche multiplication is used).

1.2 The PhotoMultiplier Tubes

A PhotoMultiplier Tube is a typical example of a vacuum phototube. It represents one of the most common light detectors for the readout of scintillators. In fact, it is capable to convert light into a detectable electrical signal: the photoelectron produced by the incoming photon is multiplied thanks to the secondary emission of electrons. As shown in figure 1.1, a typical photomultiplier tube consists of the following elements [7]:

- a glass vacuum tube;
- an input window, which has to be crossed by the visible/UV photons;
- a photocathode (made of photosensitive material), where the incoming light flux is converted into an electric flux;

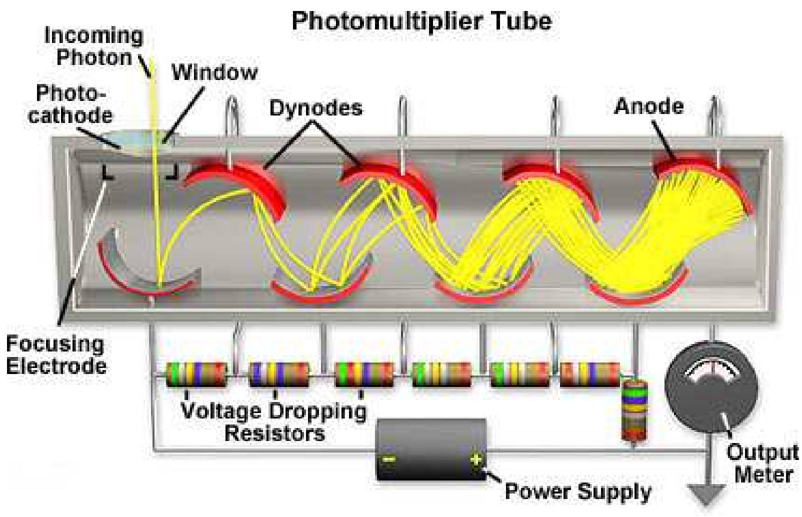

Figure 1.1: Scheme of a photomultiplier tube [7].

- an electron multiplier, which consists of a series of secondary emission electrodes;
- an anode which collects the electron flux.

As mentioned above, the two fundamental phenomena for the operation of a photomultiplier are the photoemission and the secondary emission [3]. The incident light (produced for example by a scintillator) excites the electrons in the photocathode so that photoelectrons are emitted in vacuum (photoemission process). Thanks to an electric field, each emitted photoelectron is accelerated and focused by the focusing electrode onto the first dynode (see section 1.2.2) where it extracts more electrons; this process is repeated at each of the following dynodes creating an avalanche of secondary electrons (secondary emission). At the end of the electron multiplier stage, the electron cascade is collected by the anode. The resulting electric current is proportional to the number of incident photons.

The different components of a typical photomultiplier are described in the following sections.

1.2.1 The Photocathode

The photomultiplier photocathode has to convert the energy of the incident photons into photoelectrons via the photoelectric effect. Since most photocathodes are made of semiconductor materials, the semiconductor band theory can be used to describe the photocathode working principle.

Figure 1.2 presents a schematic view of the semiconductor (i.e. the photocath-

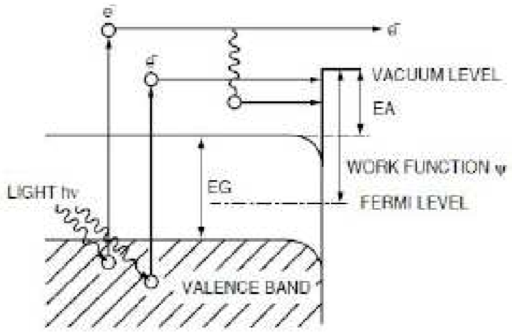

Figure 1.2: Energy band structure of a semiconductor: the main characteristics such as the valence and conduction band and the energy gap are indicated together with the electron affinity, the vacuum level and the work function.

ode) band model. It is characterized by three fundamental quantities:

- the $forbidden\ band$ (the $energy\ gap\ E_g$, where there are no available energy levels): in a semiconductor this is the energy region that separates the $valence\ band$ (where the electrons are bound to the atoms of the crystal) from the $conduction\ band$ (where electrons are free to migrate through the crystal). The width of the band gap is determined by the lattice space between the atoms thus it depends on the temperature (it decreases when the temperature increases[1]) and the pressure [5];
- the $electron\ affinity$ (EA), which represents the distance between the conduction band and the vacuum level (i.e. the energy level of a free electron outside the crystal);
- the $work\ function$, that is the minimum energy needed to move an electron from the Fermi level into vacuum. The Fermi level is determined as the energy value where the probability of occupancy by an electron is 50%; in an intrinsic semiconductor it is placed in the middle of the band gap (the position of the Fermi level is a crucial factor in determining the electrical properties [8]).

When a photon with an energy $E > E_g$ is absorbed by an electron of the valence band, the electron gets excited and moves into the conduction band. If the electron

[1]The relationship between the band gap energy and the temperature can be described by the following empirical relation:

$$E_g = E_g(0) - \frac{\alpha T^2}{T + \beta}$$

where $E_g(0)$, α and β are parameters which depend on the material [5].

has enough energy to overcome the vacuum level, it will be emitted in the vacuum as a photoelectron.

Photocathodes are typically made of alkali metals with a small work function (of the order of 5-6 eV). There are two different types of photocathodes: the semi-transparent and the opaque one. In the first case (figure 1.3(a)), the photocathode is

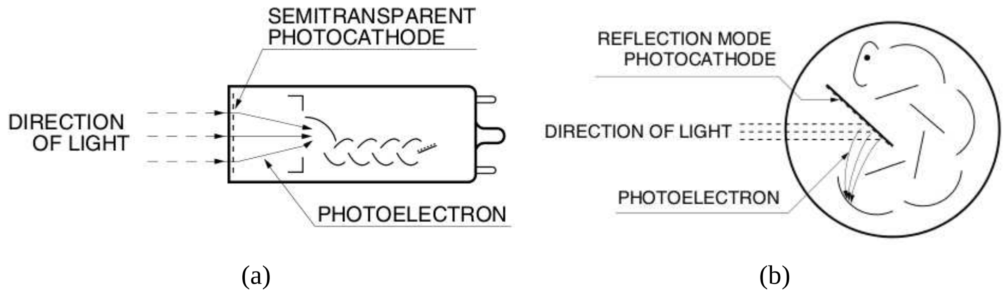

Figure 1.3: Photocathode types: a) the semi-transparent and b) the opaque one.

placed directly on the input window of the PM tube and the electrons are emitted from the side opposite to the one where the incident photons arrive; it is also called transmission-mode photocathode. The opaque photocathode (also called reflection-mode) is deposited on a metal electrode inside the tube and the electrons are emitted by the same surface hit by the photons as shown in figure 1.3(b). Semi-transparent photocathodes are normally more common in photomultiplier tubes designed to be used with scintillation detectors.

The photocathode conversion efficiency is closely related to its material and to the incident light wavelength: this dependence on the light wavelength is also called spectral sensitivity. The low limit of the sensitivity is due to the material of the input window (typically made of borosilicate glass, UV-transparent glass or quartz), while the upper limit depends on the photocathode material.

The spectral sensitivity is usually expressed in terms of $quantum\ efficiency$ (QE), which represents a measurement of the incident photons fraction that results in a detectable output. QE is defined as

$$QE = \frac{number\ of\ emitted\ photoelectrons}{number\ of\ incident\ photons} \tag{1.1}$$

and it is usually expressed as a percentage.

QE would be 100% for an ideal photocathode, but only recently values larger than 43% have been achieved [9]. This means that almost 60% of the photons that hit the photocathode surface do not produce a photoelectron and thus are not detected.

The light wavelength dependence is shown in figure 1.4, where the quantum efficiency is plotted as a function of the light wavelength for some of the most common photocathode materials [10]. Most photocathode materials have a good

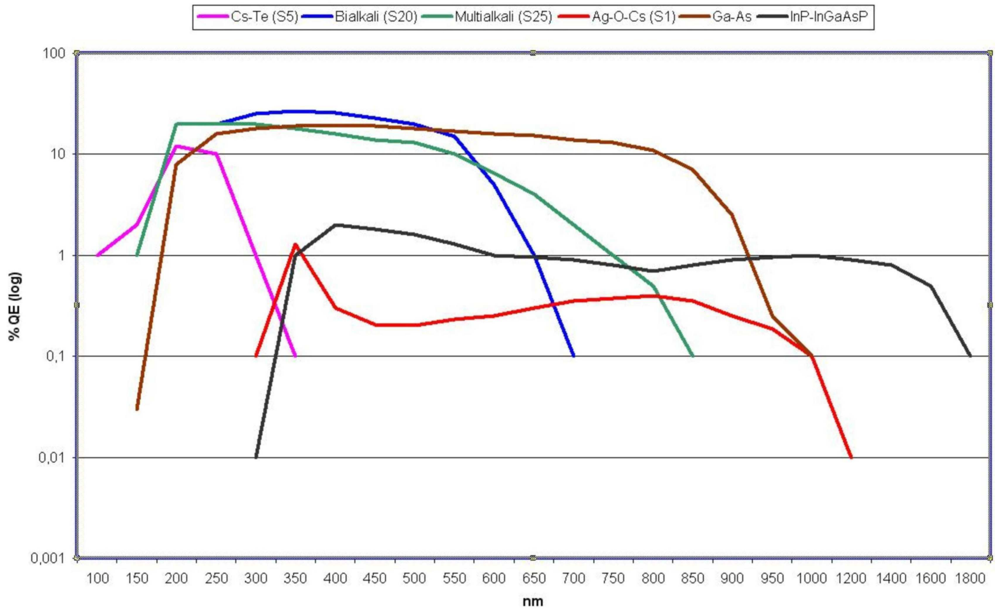

Figure 1.4: Quantum efficiency for several photocathode materials [10].

response in the shorter wavelength regions of the visible and ultraviolet spectrum (in the 200-500 nm range). Photomultipliers that have photocathodes made of bialkali and multialkali materials have a higher quantum efficiency in the green region (∼550 nm).

1.2.2 The Electron Multiplier

The number of photoelectrons emitted by the photocathode is not enough to have a measurable electrical signal apart from the case in which there is a very high incident flux (vacuum photodiodes [11, 12]). For this reason, after the emission, the photoelectron is collected and focused onto the first stage of the electron multiplier section. Figure 1.5 presents a schematic view of the electron-optical input system [2]. It consists of an electrode (at the same potential of the first electron multiplier) and a focusing electrode, which is placed on the side of the glass tube.

The electron multiplier consists of a series of stages (normally more than ten) of secondary emission electrodes, called *dynodes*. Each dynode is biased at a more positive voltage than the previous one and they are arranged such that the electric field causes the electron secondary emission: in this way the number of electrons increases from dynode to dynode.

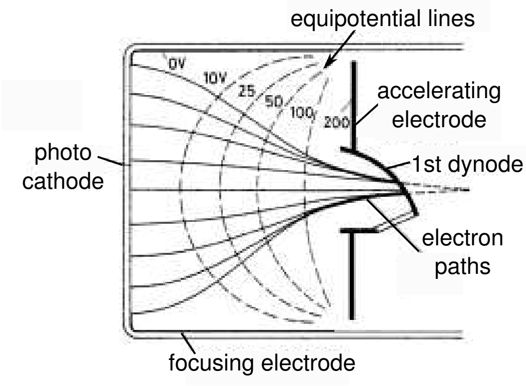

Figure 1.5: Schematic view of the electron-optical input system of a photomultiplier tube [2].

The main materials used for the dynodes are bialkali antimonide, beryllium oxide or magnesium oxide and they are usually covered with a nickel substrate.

Different dynode chain configurations are possible depending on the structure and the number of stages [13], as shown in figure 1.6:

- $circular - cage\ type\ structure$: it is very compact and allows for a very good time resolution; it is used with reflection photocathodes (figure 1.6(a));
- $box - and - grid\ type\ structure$: it has a good collection efficiency, but poor time characteristics (figure 1.6(b));
- $linear{-}focused\ type\ structure$: it has a good time resolution (figure 1.6(c));
- $venetian - blind\ type\ structure$: it has a large collection efficiency and gain, but mediocre time characteristics because the dynodes are placed with an angle of 45° with respect to the cascade axis (figure 1.6(d)).

1.2.2.1 The Gain

If N is the number of dynodes in the electron multiplier, the overall gain for a photomultiplier tube is given by

$$M = \prod_{i=1}^{N} \delta_i \tag{1.2}$$

where δ_i is the secondary emission factor (i.e. the number of the emitted secondary electrons).

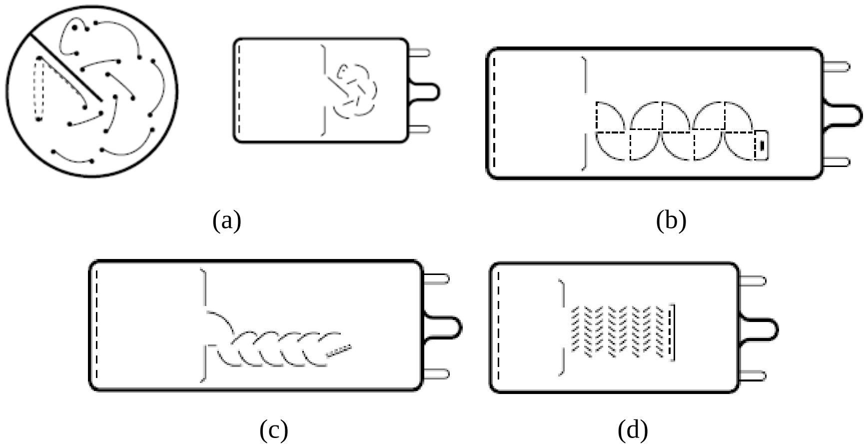

Figure 1.6: Dynode structures: a) circular-cage type; b) box-and-grid type; c) linear-focused type; d) venetian-blind type [13].

Since not all the electrons emitted by one dynode reach the next one thus not contributing to the multiplication, the $collection\ efficiency\ n_i$ has to be taken into account:

$$M = \prod_{i=1}^{N} g_i \tag{1.3}$$

where g_i is the gain of the ith-dynode:

$$g_i = \delta_i n_i \tag{1.4}$$

The most common photocathode materials have δ equal to 5 and $n_i \approx 1$ which, for a number of stages of 10, allow to reach a gain of $5^{10} \sim 10^7$.

1.2.2.2 Magnetic Field Effects

The photomultiplier tubes are typically very sensitive to the magnetic field; even the influence of the Earth one is enough to produce an effect on the PMT performance [14].

The most sensitive part of the photomultiplier is the collection system: in fact, a small magnetic field is enough to deviate the electron cascade from its optimum trajectory. The electron emitted by the photocathode may not reach the first dynode and in this way the efficiency of the PMT could be reduced.

The efficiency loss depends on the type of the photomultiplier (mainly on the dynodes structure) and also on the orientation of the photomultiplier itself in the magnetic field. Figure 1.7 shows the effects of a magnetic field on a photomultiplier oriented along the three axes: the relative gain has been plotted as a function

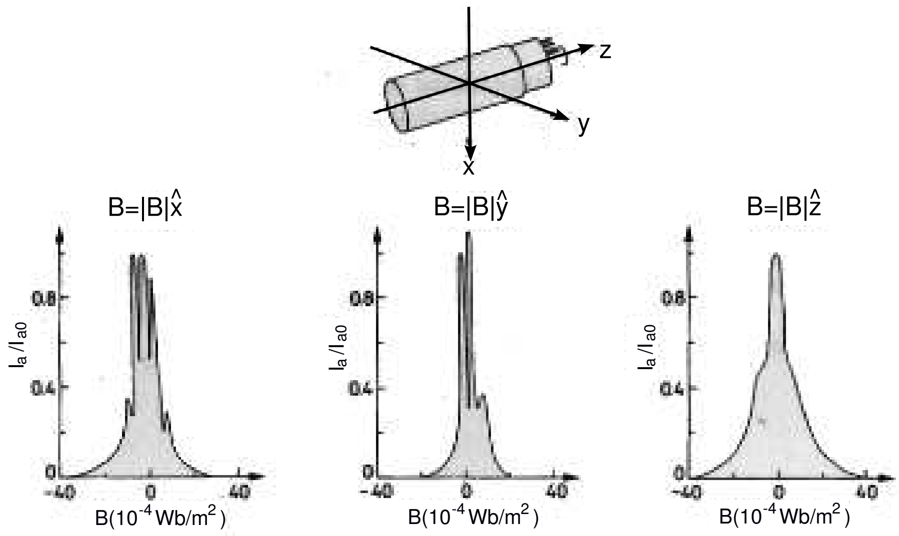

Figure 1.7: Effect of the magnetic field on the anode current of a PMT for different field orientations [2].

of the magnetic flux. It is possible to note that in all the three cases the anode current decreases as the magnetic flux increases, and the effect is the smallest when the field is oriented along the axis of the PMT.

In order to shield the effects of the magnetic field, a μ-metal screen can be placed around the PM tube: transverse fields up to 300 Gauss and axial ones up to 100 Gauss can be tolerated with a shielding of 4 cm around the photocathode [15].

1.2.3 The Anode

The anode of a photomultiplier tube is an electrode placed at the end of the dynode section which collects the secondary electrons produced by the dynodes. The anode current is proportional to the incident light (i.e. the number of incident photons).

1.2.3.1 The Dark Current

The current of the photomultiplier when it is not coupled to a scintillator detector is called $dark\ current$ (figure 1.8). Its value represents the detection lower limit.

The most significant source of dark current is due to the thermoionic electrons which are emitted spontaneously (via thermal agitation) by the photocathode. In applications where a single photon has to be detected, the dark current signal cannot be distinguished from real signals. The rate of this noise contribution depends

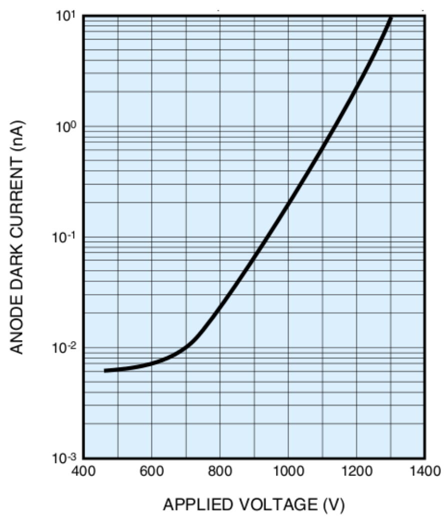

Figure 1.8: The anode dark current as a function of the bias voltage [13].

on the photocathode area, on its material and on the temperature. The rate of thermoionic electrons emission can be drastically reduced by cooling the tube.

A second source of dark current can be identified in the radioactive emission of the tube materials, especially the glass housing.

1.2.4 The Multi-Anode PMTs

When the number of channels increases dramatically (as it usually happens in a tracker or in a large area segmented calorimeter), a compact and multichannel device for the light readout is a desirable option. In the late '80s, a new photomultiplier tube appeared on the market, the Multi-Anode PhotoMultiplier.

The Multi-Anode PhotoMultiplier (MAPMT) is equivalent to many PMTs hosted in a single housing. It consists of a single vacuum tube with a photocathode (flat in most cases), an electron multiplier with the dynodes divided in different channels and a segmented anode [16]. The dynode system is very different from the one of the conventional single-anode PMTs, as presented in figure 1.9.

The gain of a MAPMT is usually smaller (of the order of 10^5) than the one of a standard PMT. Moreover, when using a MAPMT, one has to take into account both the gain dispersion between the channels and the crosstalk effect between adjacent pads. The first effect may be corrected calibrating each MAPMT channel response. As far as the crosstalk is concerned, the three main processes causing it (i.e. an electric signal on a nearby cell with respect to the one hit by a photon) are the following:

- the photoelectrons produced by the incident light can be multiplied in the

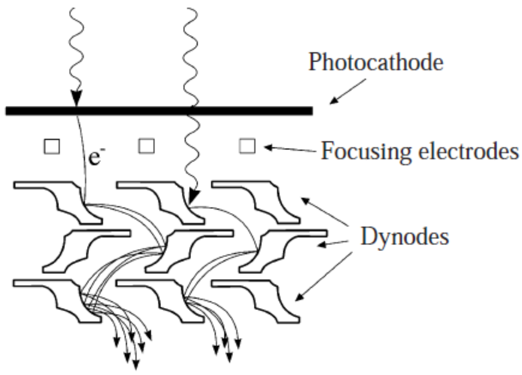

Figure 1.9: The dynodes structure of a Multi-Anode PhotoMultiplier.

wrong dynode chain if the photon reaches the wrong region of the photocathode. This effect is possible considering both the divergence of the light which exits from the scintillator (typically the light exits a fiber with a large divergence cone) and the thickness of the entrance glass window that separates the light emitting surface from the photocathode;

- a photoelectron created in the boundary region of the cell can be focused on the wrong first dynode: this effect is due to the shape of the electric field in the boundary region of the cells. In fact it can have a small component parallel to the plane of the photocathode;

- a sort of charge sharing between nearby channels may be produced by some of the electrons that can be collected by the wrong dynodes during the multiplication process.

The first two effects are referred to as "optical crosstalk" and the photoelectron they produce generates a false signal which cannot be distinguished from the true signal. The importance of the optical crosstalk effect depends mainly on the geometry of the photocathode. On the other hand, the last effect is referred to as "electrical crosstalk" and produces a much smaller electric signal than the single photoelectron one.

1.3 The Solid State Detectors

Photomultiplier tubes have pros (the capability to detect very low light fluxes, high sensitivity and high gain) and cons (the sensitivity to magnetic fields, a low quantum efficiency and the need of high voltage). For these reasons, in the early

’70s a new type of photodetector has been developed based on solid state devices, that is the semiconductor photodiode.

In this section, three kinds of solid state photodetectors are described: the PIN photodiode, the Avalanche PhotoDiode (APD) and the Silicon PhotoMultiplier (SiPM).

Before analyzing their features a brief introduction of the working principle of a semiconductor junction will be given; for a complete description see [4, 5].

1.3.1 The Intrinsic and Doped Semiconductors

Semiconductors are materials with an energy band structure which behave not quite like conductors nor insulators. A conductor (i.e. a metal) is characterized by the partial overlapping of the valence and the conduction bands, as shown in figure 1.10(a). When a valence electron is excited, it “jumps” from the valence to the conduction band: in this way, the electron becomes free to drift in the atomic lattice. On the other hand, an insulator has a very large energy band gap (with typical values in the 5-10 eV range) as shown in figure 1.10(b): when an electron is thermally excited it does not have energy enough to overcome the energy gap and reach the lower energy level of the conduction band. Consequently, in insulators the conduction band is completely empty. Semiconductors have an energy gap

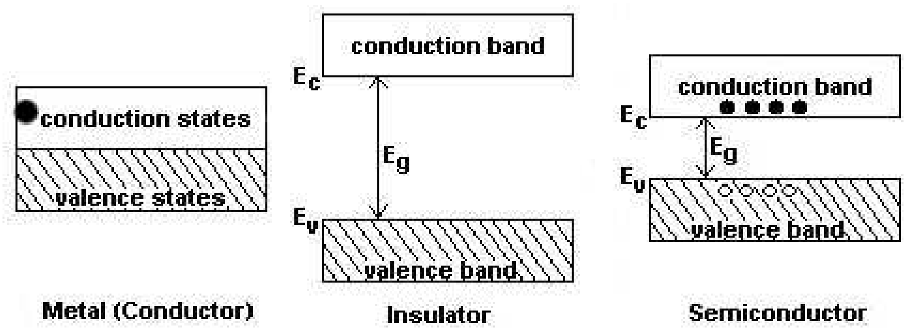

(a) (b) (c)

Figure 1.10: Energy band structure of a) conductors where the valence and conduction bands are partially overlapped, b) insulators with a large E_g (typically $>$5 eV) and c) semiconductors which have $E_g \leq$1 eV.

value which is intermediate between the conductors and the insulators ones (as shown in figure 1.10(c)) and depends on the temperature. At small temperatures an electron has not enough energy to move across the band gap (around 0 K the Silicon energy gap is equal to 1.17 eV while the Germanium one is 0.75 eV) while at higher temperatures the electron can be thermally excited. The semiconductor energy gap, in fact, decreases with temperature: at 300 K the Silicon E_g is 1.12 eV and the Germanium one 0.67 eV [2].

When an electron of the semiconductor valence band is excited (thermally or by an incident photon) into the conduction band, it leaves a hole in its original position. This means that in a pure semiconductor (i.e. without impurities), the number of holes in the valence band is equal to the number of electrons in the conduction band:

$$n = p = n_i \tag{1.5}$$

where n and p are the concentrations of electrons in the conduction band and holes in the valence one. Such a material is called an $intrinsic$ semiconductor and n_i is the intrinsic carrier density (which is equal to 1.45×10^{10} cm^{-3} in Silicon and 2.4×10^{13} cm^{-3} in Germanium at T=300 K).

This equilibrium can be changed introducing a small quantity[2] of impurity atoms called $dopants$: the semiconductor becomes $extrinsic$. In general, the dopant can have one more ($donor$) or one less ($acceptor$) valence electron in its outer atomic shell.

As an example, let us consider the Silicon case, which is a tetravalent element, and assume that the impurity is a pentavalent atom (such as Arsenic or Antimony). The impurity occupies the place of a Silicon atom. Since the valence electrons of the impurity are five, one of them cannot form a covalent bond with the surrounding Silicon atoms (as shown in figure 1.11(a)). This electron is easily excited into the conduction band (without a corresponding hole generation): in fact, the replacement of a Silicon atom by a dopant atom is accompanied by the creation of energy levels in the forbidden band gap. These levels are extremely close to the conduction band (being separated by only 0.05 eV in Silicon and 0.01 eV in Germanium) and are completely ionized at room temperature. An impurity of this type is called $donor$ and the doped semiconductor is referred to as $n - type$.

On the other hand, if the impurity is a trivalent atom, there are not enough electrons to form bonds with the surrounding Silicon atoms and therefore one covalent bond cannot be formed (figure 1.11(b)). This involves the creation of energy levels which are separated of only 0.04 eV from the valence band. This type of doped semiconductor is called $p - type$ and is obtained using elements such as Gallium and Boron.

At the thermal equilibrium the action mass law holds:

$$np = n_i^2 \tag{1.6}$$

where n_i is the intrinsic concentration. Since the semiconductor is neutral, the positive and negative charge densities have to be equal:

$$N_D + p = N_A + n \tag{1.7}$$

[2]The typical dopant concentrations are of the order of a few times 10^{13} atoms/cm^3.

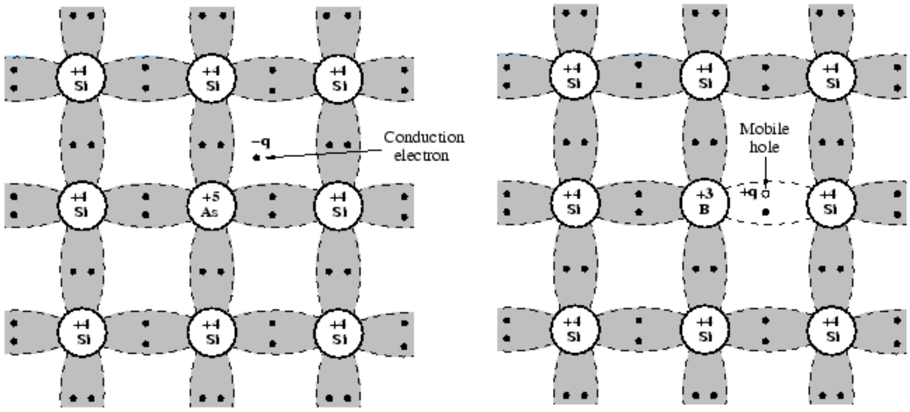

(a) (b)

Figure 1.11: Two-dimensional schematic bonds representation of a) a $n - type$ and b) a $p - type$ Silicon [5]. In the first case an atom of Silicon is replaced with an Arsenic atom (which has five valence electrons), while in the second one with a Boron atom (which is trivalent).

where N_D and N_A are the donor and acceptor concentrations respectively. In a n-type material, where N_A=0 and $n \gg p$, the electron density is practically $n = N_D$: in other words, the electron (the $majority\ carrier$) density is approximately the same as the dopant concentration, while the hole (the $minority\ carrier$) concentration is $p = \frac{n_i^2}{N_D}$.

In a p-type semiconductor N_D=0 and $p \gg n$ which means that the hole (the $majority\ carrier$) density is the same as the acceptor one ($p = N_A$), while the electron (the $minority\ carrier$) one is $n = \frac{n_i^2}{N_A}$.

1.3.2 The p-n Junction

To build a semiconductor detector, it is necessary to use a $p - n$ junction, that is to join a p-type and a n-type semiconductor as shown in fig 1.12.

When the two blocks of material get in touch, the large carrier concentration gradients of the contact region cause an initial carrier diffusion: holes from the p-side diffuse into the n-side while electrons diffuse towards the p-region. In this way, the diffusing electrons fill up holes in the p-side, while the diffusing holes capture electrons on the n-side. The effect of the charges recombination is to build up a negative space charge on the p side and a positive space charge on the n side of the junction as shown in figure 1.13(a).

The space charge (figure 1.13(b)) generates an electric field which in turn creates a drift current in the opposite direction with respect to the diffusion one

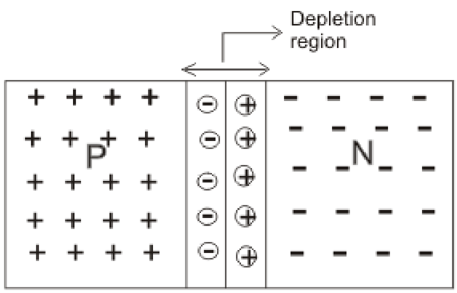

Figure 1.12: Schematic diagram of a $p-n$ junction.

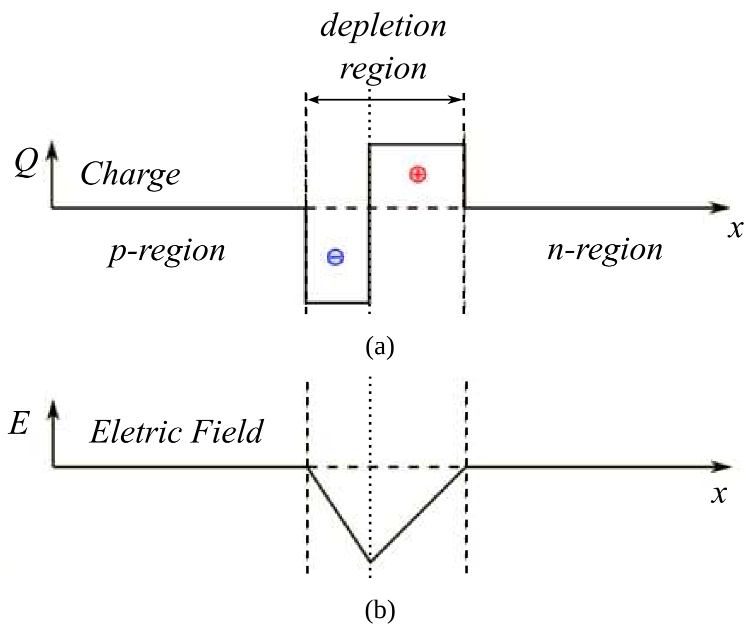

Figure 1.13: a) Charge density and b) the corresponding electric field intensity in a $p-n$ junction [2].

for each charge carrier type, as shown in figure 1.14. The overall result is that the electric field inhibits any further diffusion thus creating a region free of charge carriers. In other words, a potential barrier is generated, whose height (the so-called $built-in\,potential$, indicated as V_{bi}) is given by the following relation:

$$V_{bi} = \frac{kT}{q} \ln \frac{N_A N_D}{n_i^2} \tag{1.8}$$

where k is the Boltzman constant, T the temperature and q the electron charge; N_A is the acceptor concentration, N_D the donor one and n_i the intrinsic carrier density. For a Silicon $p-n$ junction with typical values of doping concentrations (i.e

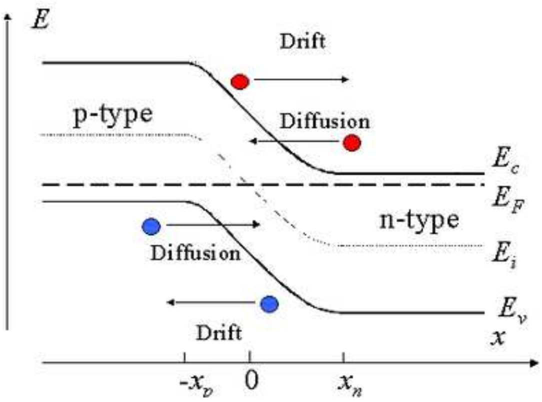

Figure 1.14: Energy band diagram of the diffusion and drift currents in a $p-n$ junction.

N_A=2×10^{16} cm^{-3} in the p-region and N_D=10^{17} cm^{-3} in the n-type region), the built-in potential at room temperature is equal to 0.77 V [17], while in Germanium junctions V_{bi} varies in the 0.2-0.3 V range.

This region depleted of free carriers is called $depletion\ region$ and it extends into both the p and the n sides of the junction. If electron/hole pairs are created in the depletion region by the incident radiation, they are swept out of this zone by the electric field and their motion produces an electrical signal. The width of the depletion region (W) in thermal equilibrium is given by the following equation [17]:

$$W = \sqrt{\frac{2\epsilon}{q}\frac{N_A + N_D}{N_A N_D}V_{bi}} \tag{1.9}$$

where ϵ is the semiconductor permittivity (for Silicon is equal to 12 times the permittivity of free space).

1.3.2.1 The Junction Bias

The $p-n$ junction can be biased in two different ways as shown in figure 1.15.

As already described, when there is no external bias (i.e in the thermal equilibrium condition), the potential barrier is qV_{bi} (where V_{bi} is given by equation 1.8) as shown in figure 1.15(a). The width of the depletion region (figure 1.15(d)) is described by equation 1.9 and it is proportional to $\sqrt{V_{bi}}$.

If a positive voltage V_f is applied to the p-side with respect to the n-side, the $p-n$ junction becomes $forward\ biased$. In this case, if the external voltage (V_f) gets larger than V_{bi}, the potential barrier is destroyed and the current starts to flow

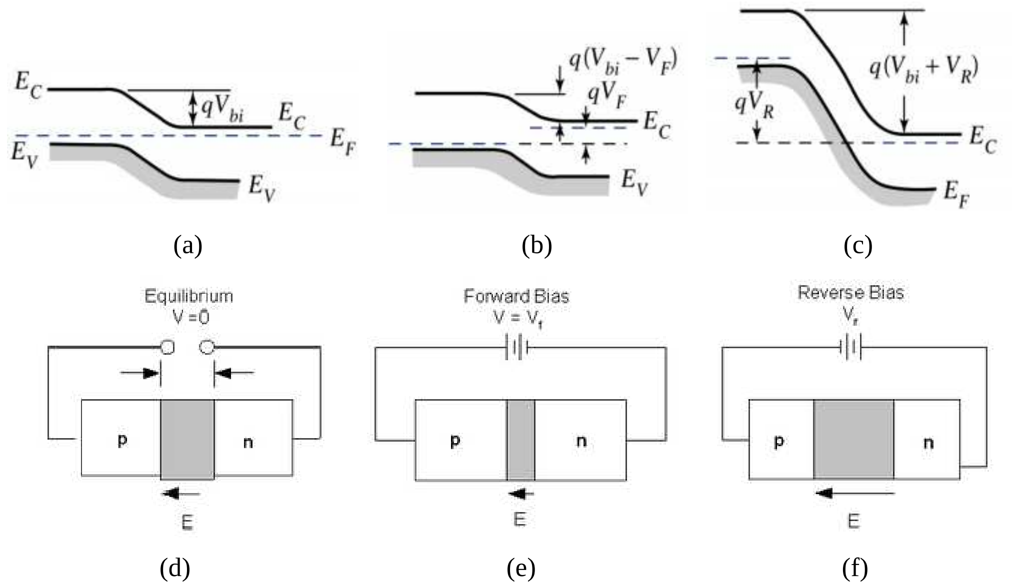

Figure 1.15: Different $p - n$ junction biasing conditions: a) and d) thermal equilibrium; b) and e) forward bias; c) and f) reverse bias [5]. The depletion region width (the grey area in figures d), e) and f)) depends on the bias condition.

(figure 1.15(b)). Taking V_f into account, equation 1.9 becomes:

$$W = \sqrt{\frac{2\epsilon}{q}\frac{N_A + N_D}{N_A N_D}(V_{bi} - V_f)} \tag{1.10}$$

and the depletion region width decreases as shown in figure 1.15(e).

On the other hand, when a $p - n$ junction is biased in a $reverse$ condition (that is the n-side is more positive than the p-side), the free carriers in the non-depleted regions are attracted by their corresponding electrodes. The result is that a higher potential barrier (proportional to $q(V_{bi} + V_r)$ with V_r the reverse bias, figure 1.15(c)) is created and the thickness of the depletion region (given by equation 1.10 substituting $V_{bi} - V_f$ with $V_{bi} + V_r$) increases, as shown in figure 1.15(f).

1.3.2.2 The Junction Breakdown

The relationship between the bias voltage and the current flowing in the $p - n$ junction is given by the Shockley diode equation [17]:

$$I = I_0(e^{\frac{V}{\eta V_T}} - 1) \tag{1.11}$$

where I_0 is the leakage current (i.e. the current that flows when the diode is reverse biased), V the applied voltage, η a constant depending on the material (typically

$1 \leq \eta \leq 2$) and V_T the thermal voltage defined as $V_T = \frac{kT}{q}$ ~25 mV at T=300 K.

A typical current-voltage curve of a $p-n$ junction is presented in figure 1.16. When the forward bias is applied, the current does not flow until the V_f value

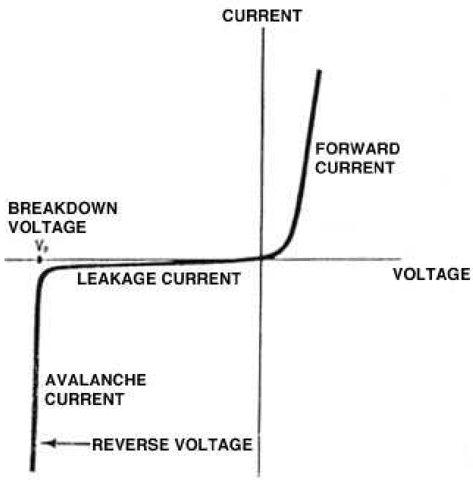

Figure 1.16: Typical $I-V$ curve of a $p-n$ junction.

gets larger than the potential barrier (V_{bi}) of the $p-n$ junction: this represents the so-called $voltage\ drop$. After this region, the current increases exponentially with the voltage. On the other hand, if the junction is reverse biased, for small voltage values only the leakage current (which is caused by the movement of the minority carriers) flows [18]; increasing V_r, the electric field becomes so high that an electrical breakdown of the junction occurs and the reverse-bias current increases dramatically. The breakdown voltage is defined as

$$V_{br} = \frac{\epsilon\,(N_A + N_D)}{2qN_AN_D}E^2_{max} \tag{1.12}$$

where E_{max} is the maximum electric field[3] before the breakdown occurs.

The breakdown of the junction is mainly due to two different mechanisms: the tunneling effect and the avalanche multiplication. The breakdown mechanism for junctions with a breakdown voltage smaller than about $4E_g/q$ (that is below a few Volts) is due to the tunneling effect, while if the breakdown occurs for

[3]For typical Silicon junctions, the maximum field at the breakdown can be expressed by the following empirical relation [5]:

$$E_{max} = \frac{4 \times 10^5}{1 - \frac{1}{3}\log_{10}(\frac{N}{10^{16}}\ \mathrm{cm}^{-3})}$$

which gives a value of the order of 10^5 V/cm.

voltages larger than $6E_g/q$, the mechanism which causes the junction breakdown is the avalanche multiplication. For intermediate voltages, both the mechanisms are involved [5].

When a large reverse bias is applied to a junction, the distance between the p-side valence electrons and the empty states in the n-side conduction band is very small. Therefore, if the reverse voltage is enough, a valence electron of the p-type semiconductor can move to an empty energy level in the conduction band of the n-side semiconductor (figure 1.17(a)). In other words, the potential barrier can be overcome via the quantum mechanical tunnelling process if a very high electric field (of the order of 10^6 V/cm or more for a Silicon junction) is applied.

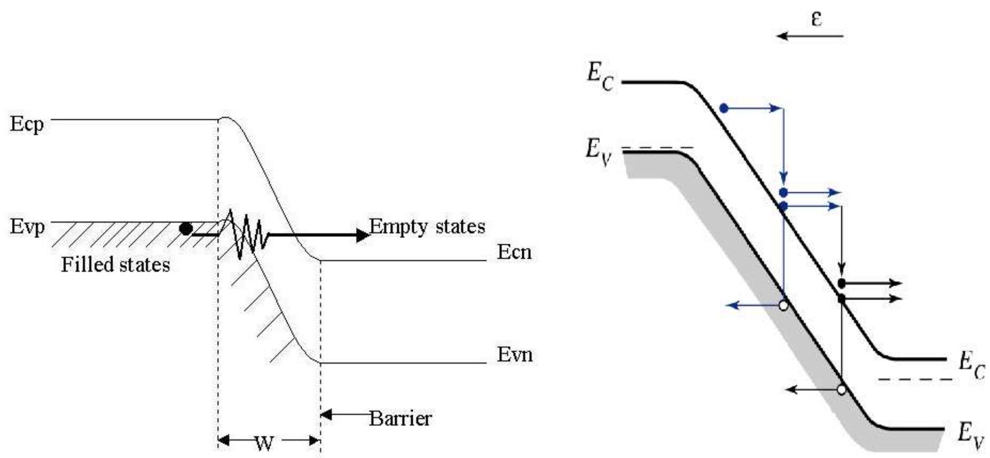

(a) (b)

Figure 1.17: a) The tunneling effect and b) the avalanche multiplication in a $p-n$ junction operating in a breakdown condition.

The avalanche multiplication mechanism is presented in figure 1.17(b): the multiplication occurs when both types of charge carriers (electrons and holes generated either thermally or via the photoelectric effect due to the incident photons) increase their kinetic energies under the effect of the electric field. If the field reaches a value of the order of 10^5 V/cm, the multiplication process starts: electrons and holes can gain enough energy to create through the impact ionization a secondary electron/hole pair colliding with a lattice atom. These new generated pairs can acquire (under the electric field effect) kinetic energy and produce additional electron/hole pairs: the result of this process is an avalanche multiplication. The multiplication process is characterized by a multiplication factor:

$$M = \frac{1}{1 - (\frac{V_r}{V_{br}})^k} \tag{1.13}$$

where V_r is the reverse bias, V_{br} the breakdown voltage and k is a parameter with values in the range 2-6. For values of V_r close to V_{br}, the multiplication factor tends to infinity: this means that each initial electron (produced in the junction) generates an infinite number of secondary electron/hole pairs in the depletion region.

The probability that a multiplication process is started depends on the electric field value and also on the spatial extension of this electric field (i.e. the region in which the charge carriers can gain energy between collisions).

1.3.3 The Photodiode

A reverse-biased $p-n$ junction can be used to detect light, i.e. to convert an optical signal into an electrical one: such a device is called photodiode. The operation of a photodiode involves three main steps [5]:

- the generation of the carriers by the incident light through the photoelectric effect;
- the carrier transport and multiplication;
- the production of an output signal.

The three solid state photodetectors described in this section operate in a different reverse bias region as shown in figure 1.18:

- the PIN photodiodes work at a low reverse bias below the avalanche region;
- the APDs are devices operated in a range of voltages where the avalanche multiplication process is linear;
- the SiPMs work with higher reverse voltages: each photon produces the junction breakdown.

1.3.4 The PIN Photodiode

One of the simplest kinds of photodiodes is the PIN photodiode: an intrinsic semiconductor (i) is placed between a heavily p^+-doped layer and a n^+-doped one (figure 1.19(a))

In a classical $p - n$ junction, the depletion region electric field is not uniform (figure 1.13(b)) and the width of the depletion region changes with the reverse bias. On the other hand, in a PIN photodiode the introduction of the intrinsic region brings two main advantages:

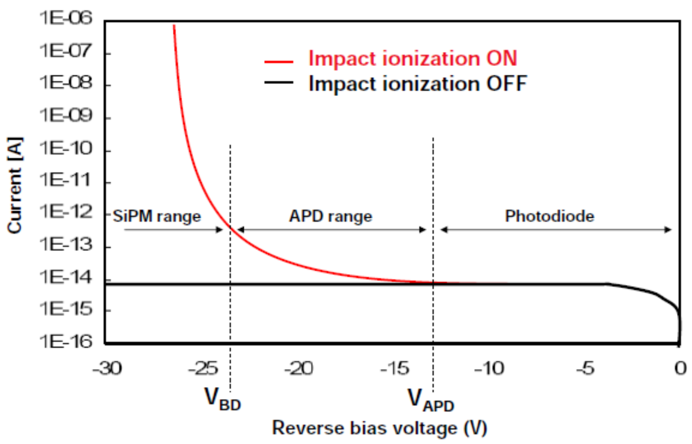

Figure 1.18: The current of a reverse biased semiconductor junction (i.e. a photodiode): the operating voltage regions of a PIN photodiode, an APD and a SiPM are indicated.

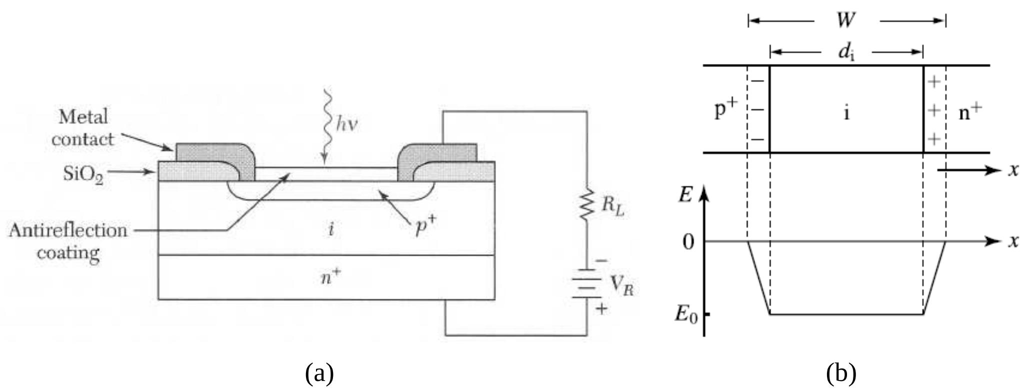

Figure 1.19: a) Schematic view of a PIN photodiode [5]; b) electric field in the PIN photodiode depletion region [11].

- the depletion region is completely defined by the intrinsic layer (i.e. the width of this region does not change significantly with the bias voltage);
- the electric field in the depletion region is uniform [11], as shown in figure 1.19(b).

The working principle of a PIN photodiode is the following:

- when there is no light on the detector, the only contribution to the current is the leakage one;
- when the light hits the detector, the incident photon is absorbed in the depletion zone of the $p-n$ junction. If the photon has enough energy, it excites

an electron from the valence band into the conduction one, leaving a hole in the valence band: an electron/hole pair has been produced. Under the effect of the reverse bias, electrons and holes drift to the anode and to the cathode respectively: this motion induces a current on the detector electrodes which is proportional to the incoming light.

The detection efficiency of a PIN photodiode is essentially equal to the quantum efficiency of the device, which is defined as the probability that a single incident photon generates an electron/hole pair (see equation 1.1). It is dominated by the band gap of the semiconductor: in fact, only the photons with an energy $E_{photon} > E_{gap}$ (where E_{gap} depends on the material[4]) create an electron-hole pair. Thanks to its small energy gap of the order of an eV, the detection efficiency of a Silicon PIN photodiode is very high (larger than 85%) over a large range (450-850 nm) of wavelengths [19], as shown in figure 1.20.

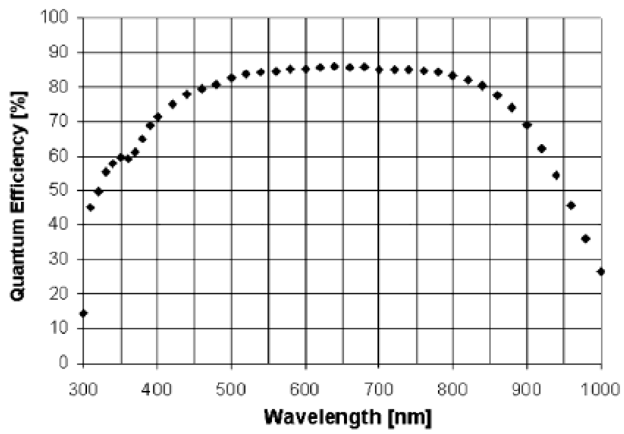

Figure 1.20: Quantum efficiency of a PIN photodiode as a function of the incident photon wavelength [19].

1.3.5 The Avalanche Photodiode (APD)

An avalanche photodiode (APD) is essentially a variation of the $p - n$ junction photodiode [20]: it detects light in the same way of a standard photodiode but it is reverse biased with a voltage large enough to generate the avalanche multiplication effect. In this way, the energy of an electron/hole pair (produced by the incident photon) increases under the effect of the electric field and secondary

[4] Among the typical materials one can list Germanium (E_{gap}=0.66 eV), Silicon (E_{gap}=1.12 eV) and Gallium Arsenide (E_{gap}=1.42 eV).

electron/hole pairs can be created via the impact ionization. The multiplication process gives to APDs an internal current gain (of the order of $\sim$100) maintaining the proportionality with the incident flux.

Figure 1.21 shows a typical cross-section of an APD. The photogeneration

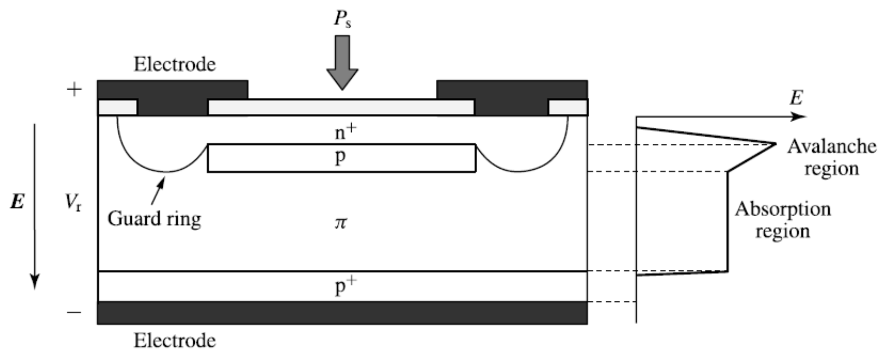

Figure 1.21: Schematic view of an APD with the electric field profile.

takes place in a region which is separated from the avalanche multiplication region[5]: the absorption region consists of a quite large intrinsic region (with a p^+-layer as a substrate) while the multiplication occurs in the $p - n$ junction (5 μm thick, where the electric field reaches values of $\sim 2\times10^5$ V/cm).

The detection efficiency of an APD is quite similar to the one of a PIN photodiode. Defining the PDE as the QE multiplied by the avalanche trigger probability (which is generally equal to 1, see section 1.3.6.2), the detection efficiency reaches values of the order of 80%.

However, the avalanche multiplication process has a random nature: each absorbed photon can produce a finite number (in the range of tens or hundreds) of secondary electron/hole pairs. But every incoming photon does not generate the same number of electron/hole pairs which implies that the multiplication process varies on an event by event basis. These fluctuations produce a noise factor called "excess noise factor" [8].

1.3.6 The Silicon PhotoMultiplier (SiPM)

Since the PIN photodiodes have no internal gain and the APDs have a very limited gain (typically around 100), an alternative to detect low light levels has been developed: the Silicon PhotoMultipliers (SiPMs) [21, 22]. From a certain point of view, SiPMs are the solid state alternative to PMTs.

[5]In principle, the avalanche multiplication can be produced also in a classical $p - n$ or PIN photodiode which works around its breakdown voltage; however, the effect would not be optimized because of the thickness of the sensitive area (which is of the order of 300 μm) [5].

A silicon photomultiplier can be described as a 2D array of pixels (typically 500-4000 pixels/mm^2 with a dimension in the 20-200 μm range) joined together in parallel on a common Silicon substrate [23]. Figure 1.22 presents a schematic view of a SiPM.

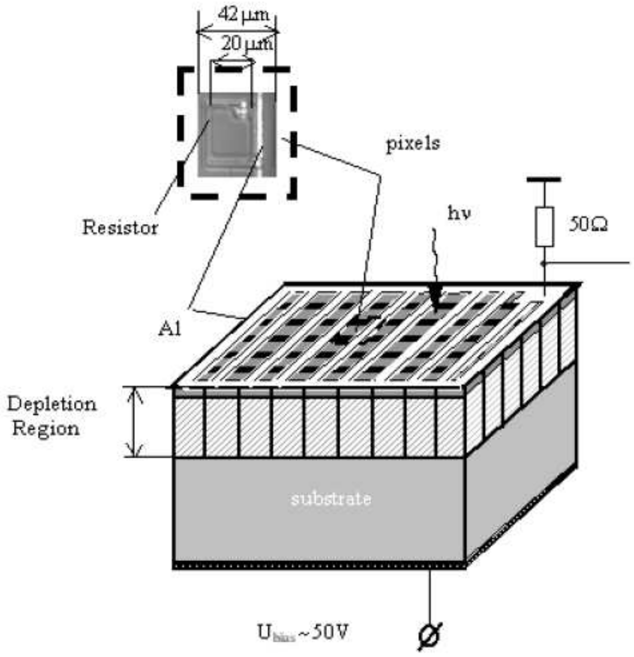

Figure 1.22: Schematic view of a SiPM [24].

Each SiPM pixel works as an independent Single Photon Avalanche Photodiode (SPAD) [24]: a SPAD is an APD biased with a voltage 10-15% higher than the breakdown voltage allowing it to work in the so-called Geiger mode (they are also called Geiger-Mode APDs, GM-APD). In this way, each pixel of the SiPM is a binary (or digital) device: this means that the output signal is not proportional to the energy released by the photon, but just registers its arrival.

The sum of all the SiPM pixels outputs is proportional to the number of fired cells: if N photoelectrons fire N pixels, the current response will be N times the single photoelectron response. In other words, the SiPM is able to provide an analog information.

1.3.6.1 The Quenching Mechanism

As it happens in an APD, when a photon hits the SPAD, it generates an electron/hole pair if its energy is larger than the energy gap. Under the effect of the electric field, secondary electron/hole pairs are produced through the impact ionization process.

In a standard APD the carrier multiplication is spontaneously suppressed after the charge collection on the electrodes, because the electric field is not large enough to create a self-sustaining avalanche which is in fact the case of a SPAD[6]. Thus, the multiplication process in a GM-APD would continue infinitely producing the breakdown of the junction. In this way, the number of electrons generated at the anode would not be proportional to the number of incident photons, as it happens in a Geiger-Mueller counter [25].

When an avalanche is triggered, the signal saturates to the maximum value. In order to detect the next incident photon, the current has to be quenched and the avalanche process stopped artificially. For this reason, a quenching mechanism able to suppress the avalanche is needed. There are two different quenching mechanisms:

- the active quenching, using an electronic circuit (as shown in figure 1.23(a)): it detects and quenches the breakdown reducing the voltage across the device for a certain time. After having stopped the avalanche, the bias voltage reaches again the operating value. This active quenching is not used with SiPMs because an electronic circuit would be required for each pixel (creating a large dead region);

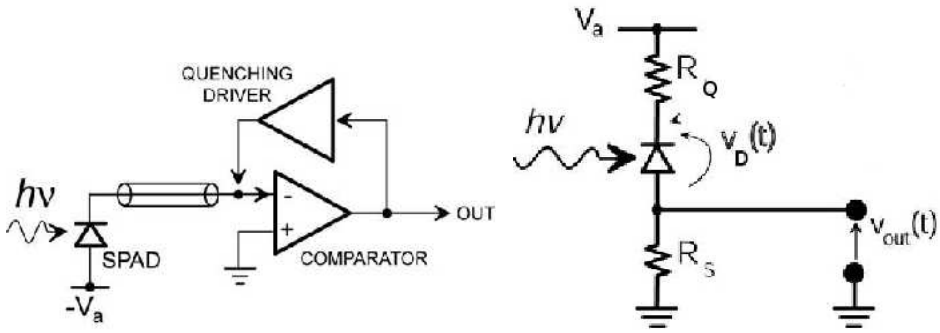

(a) (b)

Figure 1.23: a) Active and b) passive quenching circuit of a SPAD [23].

- the passive quenching (the mechanism used in a SiPM, figure 1.23(b)) consisting of a large resistor R_Q (from hundreds of kΩ to a few MΩ) in series with the photodiode. If the current through the diode is zero, the voltage

[6]The typical value of the SPAD electric field is $\sim 10^6$ V/cm to be compared with 10^5 V/cm of an APD.

across the diode is larger than the breakdown voltage (equal to the bias voltage). When a photon is absorbed and the avalanche triggered, a current on the series resistor is produced. Given the potential drop on the resistor, the bias voltage is not completely available on the junction and the avalanche multiplication phenomenon is suppressed because of the reduction of the applied bias. After the quenching phase, the voltage increases again to reach the value of the bias voltage; given the presence of the quenching resistor, the rise takes place with a time constant τ_{rec}:

$$\tau_{rec} = R_Q \cdot C_{pixel} \tag{1.14}$$

where C_{pixel} is the capacitance of the junction depletion region (with a typical value from tens to hundreds of fF).

τ_{rec} is the so-called recovery time: it represents the time needed by each pixel to recover from the discharge. In other words, this is the time during which the SiPM is insensitive to other incoming photons (dead time). From equation 1.14, it is evident that the dead time of the SiPM depends on the value of each junction capacitance and of the quenching resistor; a typical value is of the order of 10 ns [26].

1.3.6.2 The Photon Detection Efficiency

The Photon Detection Efficiency (PDE) represents the probability that an incident photon is effectively detected by the SiPM. In the SiPM case, the PDE is not just the quantum efficiency, but it is given by the product of the quantum efficiency ϵ_{QE}, the geometric efficiency ϵ_{geom} and the avalanche triggering probability $\epsilon_{trigger}$ [27]:

$$\epsilon_{PDE} = \epsilon_{QE} \cdot \epsilon_{geom} \cdot \epsilon_{trigger} \tag{1.15}$$

The quantum efficiency consists of two different components: the intrinsic QE and the extrinsic QE. The first represents the probability of an incident photon to be converted into a electron/hole pair in the depletion region of the SiPM. The second one is the transmission efficiency of the photon: it represents the number of photons that hit the detection region and do not reflect out of the device. This parameter depends on the wavelength of the incident photon ($QE(\lambda)$), the internal structure of the device and the diffusion length of electrons and holes. The SiPM quantum efficiency can reach values of 80%-90% (comparable with the APD ones).

The geometric efficiency (fill factor) is introduced because only a part of the whole pixel area is sensitive to the photon. This parameter is defined as the ratio between the active area of the detector and its whole area. The fill factor varies between 0.3 and 0.8, depending on the pixel geometry, the pitch and the size of the quenching resistor. It is evident that this parameter decreases when the density of the pixel increases [28], as shown in figure 1.24. A larger number of pixels,

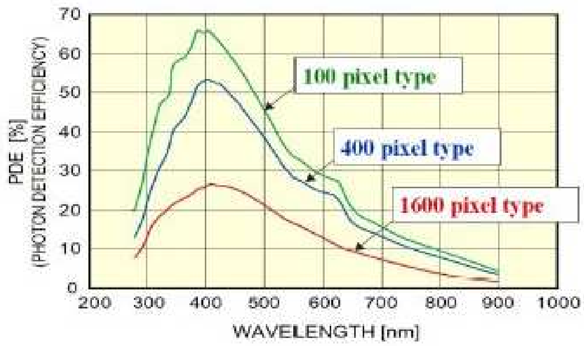

Figure 1.24: The PDE as a function of the incident photon wavelength for SiPMs with a different number of pixels [28].

in fact, means a larger number of quenching resistors on the SiPM surface: this increases the SiPM dead area. On the other hand, the minimal space between two pixels cannot be reduced without increasing the risk of having optical crosstalk effects (i.e. photons produced during a pixel avalanche process which can reach the adjacent ones, see section 1.3.6.5).

The avalanche triggering probability is the probability of a primary photoelectron (generated by the incident photon) to start an avalanche. If the reverse bias voltage is large enough, this parameter is close to 1. Moreover, it depends on the temperature.

The PDE of most SiPMs is optimized for the green or blue light region and reaches peak values of $\sim$50% [29].

1.3.6.3 The Gain

The gain of a device operating in Geiger mode is defined as the number of secondary electron/hole pairs generated during the Geiger cascade process. In particular, it is defined as the total charge produced by a single firing pixel (Q_{pixel}) divided by the electron charge (q_e):

$$G = \frac{Q_{pixel}}{q_e} \tag{1.16}$$

The gain is linearly dependent from the applied bias:

$$Q_{pixel} = C_{pixel} \cdot (V_{bias} - V_{break}) = C_{pixel} \cdot V_{over} \tag{1.17}$$

where the difference between the applied voltage (V_{bias}) and the breakdown voltage (V_{break}) is the overvoltage (V_{over}). A large pixel capacitance (typical of the SiPM pixels) has an important effect on the gain thus requiring the bias voltage to be as stable as possible.

Figure 1.25 shows the gain as a function of the bias voltage (for a constant breakdown voltage). In particular, the gain is constant at a value equal to 1 for a

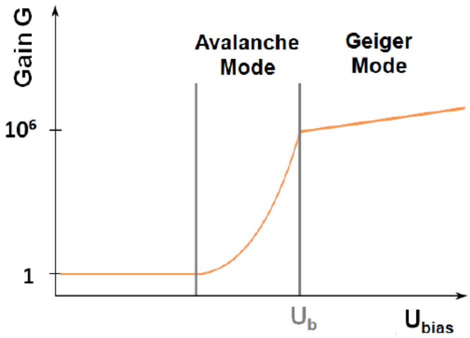

Figure 1.25: The photodetector gain as a function of the bias voltage.

bias voltage smaller than the breakdown voltage, then it increases quickly for bias voltages close to V_{break}. For V_{bias} larger than the breakdown voltage the device starts to work in Geiger mode and the gain reaches values of the order of 10^6 (a value comparable with the PMT gain). After the breakdown voltage, the gain increases linearly with the bias voltage.

1.3.6.4 The Dynamic Range

The dynamic range of a silicon photomultiplier represents the maximum number of photons which can be detected and is limited by the total number of pixels.

In a silicon photomultiplier, each pixel can detect a single photon: as long as the number of incident photons is smaller than the number of SiPM pixels, the number of fired pixels gives the number of incident photons. Considering a high intensity flux, the probability that several photons hit at the same time the same pixel increases. If an electron/hole pair is generated in a pixel that is recovering from the previous discharge, the pixel cannot fire again and these carriers do not contribute to the signal and the photon is lost. Thus, the number of firing pixels and the output signal are subject to saturation effects which become evident increasing the light intensity.

The number of fired pixels is given by the following equation:

$$N_{fired} = N_{total}\left[1 - e^{\left(\frac{-N_{ph}\cdot PDE}{N_{total}}\right)}\right] \tag{1.18}$$

where N_{ph} is the number of incident photons while N_{total} is the total number of pixels. Since the PDE is a function of the bias voltage and of the wavelength of the incident photons, the dynamic range of a SiPM is also a function of these parameters.

1.3.6.5 The Noise

As in the PMT case, the main source of noise which limits the SiPM performance is due to the random generation of thermal electrons. Even if no light is present, these carriers can trigger an avalanche which produces a current signal identical to the signal of a single photoelectron. This signal is called dark current. The rate of the emission of thermal electrons depends linearly on the applied bias, on the temperature [7] (as shown in figure 1.26) and also on the number of pixels. The dark

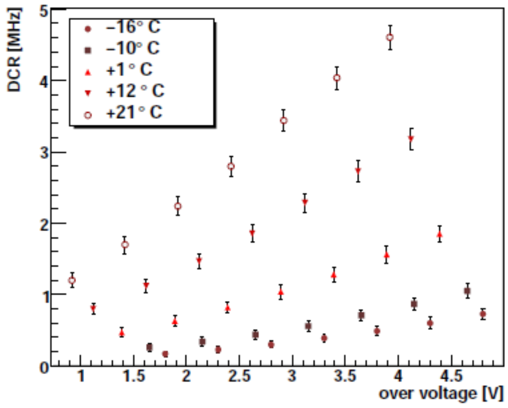

Figure 1.26: The dark count rate (DCR) as a function of the overvoltage for different temperatures [30].

rate of a typical SiPM (resulting from the sum of the dark pulses of each pixel) is in the range from 100 kHz to a few MHz per mm^2.

Another source of noise is the so-called afterpulsing. When a carrier is trapped by an impurity of the semiconductor during the avalanche, it can be released some nanoseconds later (the typical delay is 100 ns). If the time interval is longer than the recovery time of the pixel, another delayed avalanche may be triggered [22].

The last process that influences the noise of a SiPM is based on the production of photons during the avalanche multiplication. Figure 1.27 presents a schematic

[7] The probability of the thermal production of an electron/hole pair is a function of the temperature [30]:

$$p(T) = CT^{\frac{3}{2}} e^{-\frac{E_g}{2k_B T2}}$$

Thus the SiPM dark counts are reduced of a factor 2 when the temperature decreases of 8°C [19].

view of this process called optical crosstalk. The avalanche mechanism generates

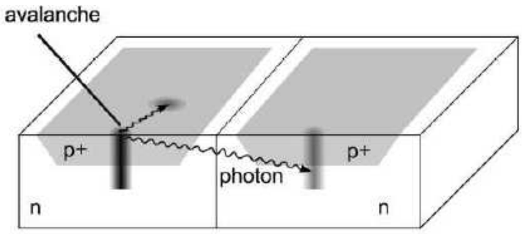

Figure 1.27: Scheme of the principle of the optical crosstalk.

approximately 30 photons with an energy large enough to reach one of the adjacent pixels [31] producing in this way a Geiger discharge. The resulting pulse is the sum of the signal of two pixels. This parameter is a function of the overvoltage and of the distance between neighboring pixels.

1.3.6.6 The Time Resolution

SiPMs have a very good time resolution, mainly because of the very small width of the depletion region ($\sim$2 μm). Two main parameters affect the timing performance:

- the avalanche propagation time, which is the time required for the Geiger avalanche process and depends on the hit position of the photon. The overall breakdown propagation time is of the order of hundreds of picoseconds ($<$500 ps);
- the carriers collection time: the carriers produced by a photon can take several tens of nanoseconds to reach the multiplication region and trigger an avalanche.

Figure 1.28 presents the single photoelectron (i.e. single pixel) timing resolution obtained with a very low intensity laser pulse characterized by a light pulse of 40 ps FWHM. The measured timing resolution of 123 ps FWHM includes also the laser pulse width and electronics contribution: after the subtraction of these contributions, the intrinsic SiPM single photoelectron timing resolution becomes $\sim$100 ps FWHM (which means $\sim$50 ps RMS) for photons absorbed in the depletion region [24].

1.4 PMT versus SiPM

The main characteristics of PMTs and SiPMs are summarized in table 1.1.

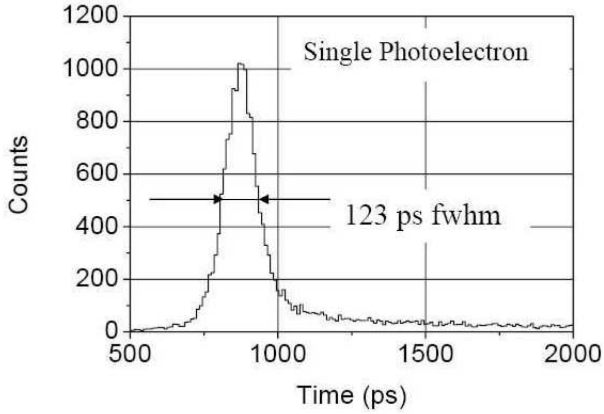

Figure 1.28: Single photoelectron timing resolution: the value includes also the laser pulse width and electronics contribution [24].

	PhotoMultiplier Tube (PMT)	**Silicon PhotoMultiplier (SiPM)**
Gain	10^6	10^6-10^7
Detection Efficiency	$\sim$40%	$\geq$50%
Timing Response	$\geq$ns	Hundreds of ps
Dark Count Rate	kHz	MHz
Bias Voltage	1-2 kV	20-60 V
Size	Not Very Compact (a few cm^2 - tens of cm^2)	Very Compact ($\sim$mm^2)
Magnetic Field	High Sensitivity	Insensitivity

Table 1.1: Comparison of the main features of PhotoMultiplier Tubes and Silicon PhotoMultipliers.

The main advantages of SiPMs compared to PMTs are a high internal gain, a high detection efficiency and a very low bias voltage (which has to be compared with the PMT need of a high bias voltage of the order of a kV). SiPMs are also characterized by a very good time response, mainly due to their small recovery time (below the ns), and, thanks to their small dimension, are also easy to be organized in arrays. The most important feature, however, is their insensitivity to the magnetic field.

On the other hand, the SiPM technology has to deal with two important limitations: the dark count rate (which is of the order of one MHz in comparison to the PMT one which is of the order of one kHz) and the fill factor.

Since they are used in many high energy physics experiments [32], many studies have been performed to investigate also the SiPM radiation hardness. Even if the damage depends on the flux, type and energy of the particles, the typical effect of the radiation is the production of new centers in the Silicon band gap which increase the thermal carrier generation and thus the dark counts.

The radiation damage caused by proton and neutron irradiation is evaluated in [33] on the Hamamatsu MPPCs (Multi Pixel Photon Counters). The main effect is the increase of the leakage current after both types of irradiation: figure 1.29(a) presents the variation of the leakage current as a function of the time in case of a MPPC irradiated with 2.3×10^5 protons/mm^2/s (with an energy of 53.3 MeV) corresponding to a 130 Gy/h dose rate. It is possible to note that at the beginning the leakage current is quite low ($\sim$0.05 μA) while during the proton irradiation (which lasts $\sim$10 min) it increases linearly with time. In the same way a drastic increase of

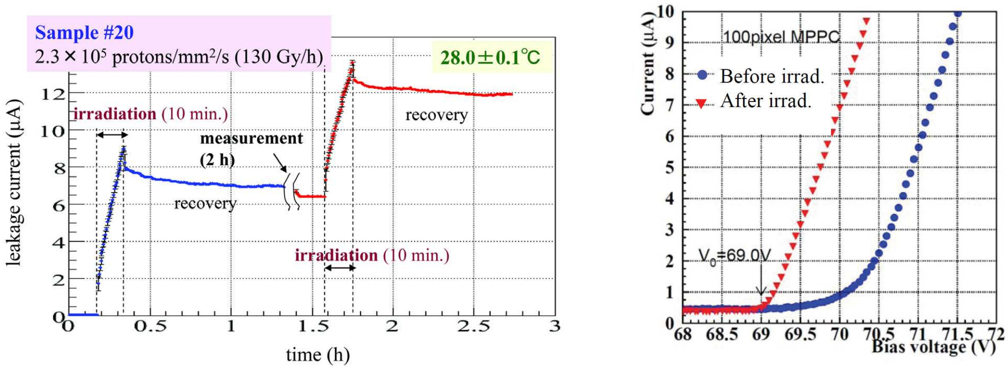

(a) (b)

Figure 1.29: The effect on the SiPM leakage current of a) proton and b) neutron irradiation [33].

the leakage current is observed after the irradiation with 10^9 neutrons/mm^2 (with an energy in a range of 0.1-1 MeV): as shown in figure 1.29(b), which presents the MPPC $I-V$ curve before and after the irradiation, the leakage current increases above the breakdown voltage (which is equal to 69 V).

The γ irradiation effects on a Hamamatsu SiPM have been studied using a ^{60}Co source, up to a total accumulated dose of 240 Gy (delivered in six steps of 40 Gy each) [34]. As shown in figure 1.30, increasing the radiation dose there is an increase in the leakage current and in the dark count rate (of a factor 1.5), while no significant changes are observed in the gain and optical crosstalk [34].

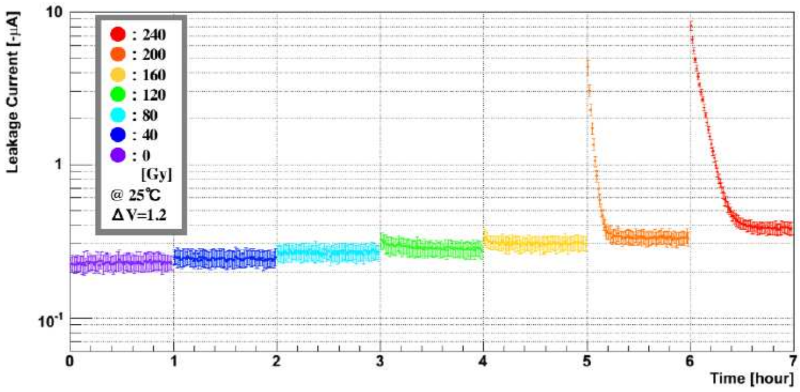

(a)

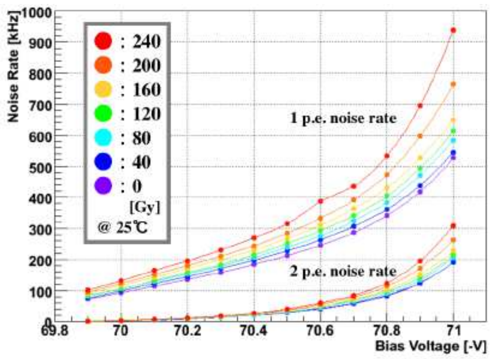

(b)

Figure 1.30: The γ irradiation effect on the SiPM a) leakage current and b) noise rate (which has been plotted as a function of the bias voltage) [34].

Chapter 2

The Scintillating Bars Detectors

Detectors based on the readout of scintillating light are very common in particle physics [2]. They are based on the fact that several materials, when excited by ionizing radiation, re-emit the absorbed energy under the form of light. The emitted photons have to be collected and converted into an electrical current by photodetectors.

This thesis work deals with the development of a totally active scintillating bar detector readout by SiPMs for future applications in particle and neutrino physics. While the first chapter has introduced the way light can be readout, the goal of the first part of this chapter is to introduce the theory of light emission in both inorganic and organic scintillator materials. For an exhaustive description of scintillators see [2, 35, 36].

In the second part of the chapter, three examples of particle physics experiments with scintillating bar detectors are presented to underline the pros and cons of these detectors.

2.1 The Scintillating Detector

The basic elements of a scintillation detector are the scintillating material (which will be described in this section) and the photodetectors (described in chapter 1), which have to be optically coupled either directly or via a light guide (section 2.1.4).

2.1.1 The Scintillator

A scintillator can be defined as a wavelength shifter [37]: in fact, it converts the energy (or wavelength) of the incident particles (which can be either charged or neutral particles) into photons in the visible range, which can be easily detected by photodetectors. If the light re-emission occurs immediately after the absorption of the radiation (more precisely within 10^{-8} s, which is the typical time of atomic transitions), the process is called $fluorescence$. On the other hand, the process is called $phosphorescence$ if there is a delay between the absorption and the light re-emission which is due to the excitation of metastable states. The delay time can vary (depending on the material) from a few microseconds to hours [35].

The time evolution of the photons emission process in a scintillator can be described as a first approximation with an exponential decay law [2]:

$$N = \frac{N_0}{\tau_d} e^{-\frac{t}{\tau_d}} \tag{2.1}$$

where N is the number of photons emitted at the time t, N_0 the total number of emitted photons and τ_d the decay constant. In this relation the rise time is not taken into account: in most materials the rise time from zero to the maximum is typically much shorter than the decay time (as show in figure 2.1).

A more precise description allows to identify two different exponential contributions:

$$N = Ae^{-\frac{t}{\tau_f}} + Be^{-\frac{t}{\tau_s}} \tag{2.2}$$

where τ_f and τ_s are respectively the decay constant of the fast and short components. The relative amplitude A and B of the two components depends on the

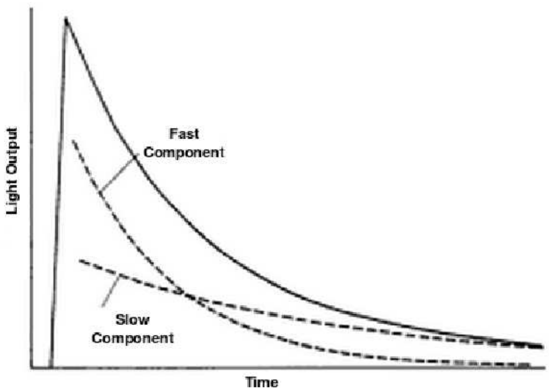

Figure 2.1: The scintillating light decay curve: the dotted lines represent the fast and short component contributions [2].

scintillating material, even if the fast component usually dominates. The technique of the pulse shape discrimination is based on the existence of these two components: the study of the emitted light pulse allows to distinguish the type of the incident particle.

Not all the scintillating materials can be used as detectors. A good scintillating detector in fact has to satisfy the following requirements [2]:

- it should have a high efficiency in the conversion of the incident radiation deposited energy in fluorescent light (minimizing the phosphorescence process, which is typically undesirable);

- it has to be transparent to the wavelength of its own emission allowing at the same time the light transmission;

- it should have a short decay constant for the luminescence to obtain fast signals;

- the emission light has to be in a spectral range compatible with the spectral response of the photodetector;

- it should have a good optical quality, good mechanical properties and be a workable material.

The materials used as scintillators can be divided in two main categories: inorganic and organic scintillators. They are both described in the following section with a particular attention on the organic ones since the detectors used for this thesis are plastic scintillators.

2.1.2 The Inorganic Scintillator

Inorganic scintillators are mainly crystals of alkali halides which contain activator impurity centres. Among the most important examples, one can list NaI(Tl) and CsI(Tl), where the impurity is Thallium (Tl). Non-alkali materials such as BGO (Bismuth Germanate), CsF and $PbWO_4$ (Lead Tungstate) are also used for positron emission tomography [38], for energy spectroscopy [39] and high energy physics [40]. Table 2.1 presents the main features of these inorganic scintillators.

Scintillator Material	**Density** (g/cm^3)	**Wavelength Emission** (nm)	**Decay Constant** (ns)	**Light Output** (% NaI(Tl))
NaI(Tl)	3.67	410	250	100
CsI(Tl)	4.51	565	1000	45
BGO	7.13	480	300	10
CsF	4.65	390	5	5
$PbWO_4$	8.28	480	2-11-98	0.8

Table 2.1: Properties of several inorganic scintillators; the light output is indicated as a percentage of the NaI(Tl) output which is chosen as a reference [35].

The scintillation mechanism in inorganic materials depends on the structure of the crystal lattice. In an inorganic scintillator impurities (the so-called $activators$) are commonly present in the crystal and they create special sites in the lattice modifying the band structure and creating energy states in the forbidden gap (figure 2.2).

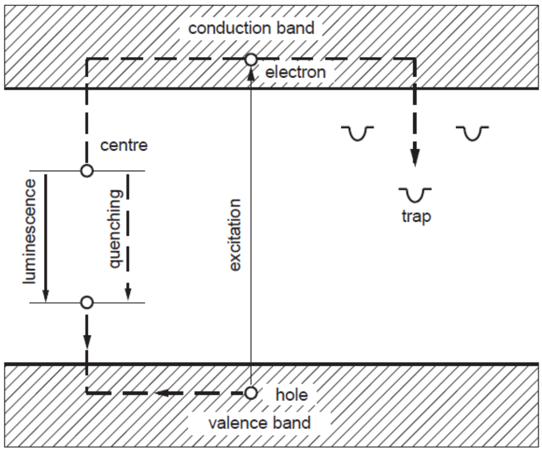

Figure 2.2: Energy band structure of an inorganic scintillator: states within the forbidden band are created by the added impurities [3].

When a particle hits a pure crystal two main processes may take place:

- if the particle energy is large enough, the particle itself can ionize the crystal by exciting a valence electron to the conduction band: thus, a free electron/hole pair is produced;
- if the energy of the incoming particle is smaller than the energy gap, the valence electron cannot reach the conduction band and it remains bound to the hole. In this way, an $exciton$ (i.e. a bound state of an electron and a hole) is created which remains de-localized and can move freely within the crystal in an energy level just below the conduction band (the so called $exciton\ band$).

The activation centres can be of three types [35] originating three different processes:

- the luminescence centres, in which the de-excitation to the ground state is accompanied by photon emission (with an energy smaller than E_{gap}). This is called $fluorescence$;

- the quenching centres, which are similar to the luminescence ones except that the excitation energy is dissipated as phonons instead of light. This is an unwanted effect which reduces the scintillator output;

- the traps centres, which are metastable states in which electrons and holes (or also excitons) can stay for a long time before acquiring enough energy to return to the conduction and valence bands or to move to a quenching or luminescence centre. This last process corresponds to a delayed photon emission which is called $phosphorescence$.

Impurities are usually introduced to increase the probability of the de-excitation process and to make the scintillator almost 100% transparent to its own emission spectrum.

The advantages of inorganic crystals over organic scintillators lie in their larger stopping power[1] (mainly due to their higher density and atomic number). Moreover, inorganic crystals have some of the largest light outputs among all the scintillators (of the order of 4×10^4 photons per deposited MeV): this results in a very high energy resolution. These features make inorganic scintillators suitable for the detection of X and γ rays, high-energy electrons/positrons (especially in diagnostic imaging applications [38]) and heavy charged particles (such as αs and protons).

On the other hand, inorganic scintillators are 2-3 orders of magnitude slower than organic scintillators: their time response is of the order of hundreds of ns (except for CsF). Some of them are also hygroscopic (such as NaI(Tl), CsI(Tl) and also CsF) thus requiring to be used in closed boxes.

2.1.3 The Organic Scintillator

The organic scintillators are aromatic molecular compounds with one or more benzene ring structures [35]. Figure 2.3 presents the molecular structure of Anthracene, which is a typical organic scintillator.

Whereas the scintillation mechanism in inorganic materials is based on the crystals electronic band structure, in organic materials the fluorescent mechanism arises from the energy levels transitions of a single molecule which can occur in the solid, liquid or vapor phase as well as in liquid or solid solutions and in plastic states [3].

The energy transitions are due to the free valence electrons of the molecules which occupy particular states known as $\pi - molecular\ orbitals$. Figure 2.4 presents a schematic view of the π-electron structure where the spin singlet states

[1] The stopping power is defined as the average energy loss of a particle per unit path length and depends on the nature of the incident particle and of the target material [1].

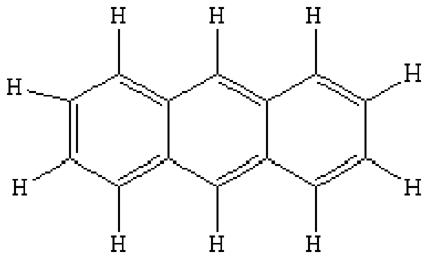

Figure 2.3: The Anthracene ($C_{14}H_{10}$) molecular structure.

(spin 0) are distinguished from the spin triplet states (spin 1). The ground state

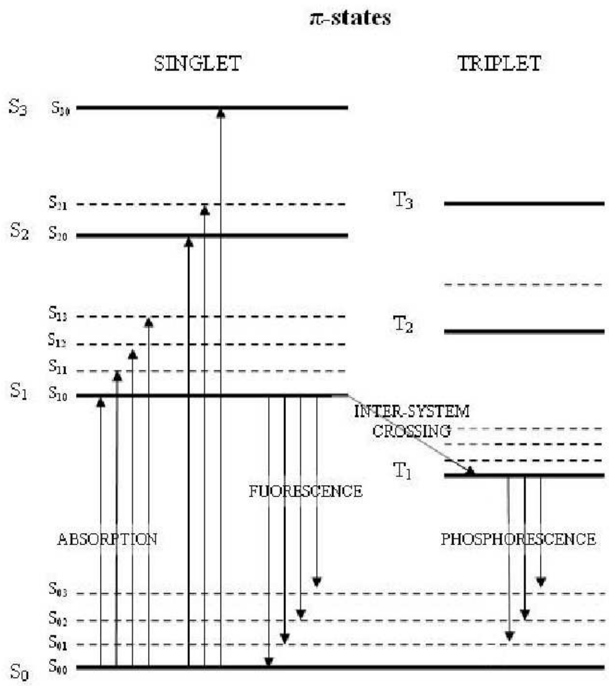

Figure 2.4: Schematic view of the energy levels of an organic molecule with a π-orbital structure [35]. The spin singlet and triplet states are indicated: S_0 is the ground state (which is a singlet spin state); S_1, S_2 and S_3 are the excited states of the spin singlet while T_1, T_2 and T_3 the excited triplet ones. The vibrational sub-levels are also indicated.

is a single spin state (called S_0) and its excited states are S_1, S_2, S_3 (spin singlet case) and T_1, T_2, T_3 (spin triplet case). At each electron level a fine structure is also associated which corresponds to the excited vibrational modes of the molecule. In a molecule of an organic scintillator, the typical energy spacing between S_0 and S_1 is of the order of 3-4 eV, whereas the spacing between the vibrational states is smaller (of the order of 0.15 eV). Given that the difference between S_0 and the first excited state is large compared with the thermal energy (which is $\sim$0.025 eV), all the molecules at room temperature are in the ground state S_0.

The energy deposited by a charged particle crossing the material excites both the electron and vibrational states. The higher singlet excitation level generally de-excites immediately ($\leq$10 ps, i.e a time comparable with the period of the molecular vibrations) to the S_1 state through the internal conversion without the emission of radiation. At this point, the probability to decay from S_1 to one of the vibrational levels of S_0 is very large: the transition occurs within a few nanoseconds. This de-excitation is the one originating the fluorescence process, which represents the fast component of equation 2.2.

The excited single state may be converted into the triplet state (the typical transition is $S_1 \rightarrow T_1$) through the inter-system crossing. Since the T_1 state cannot decay directly into the ground state (because of the spin selection rules), it decays by interacting with another excited T_1 molecule. The decay process is described by a triplet-triplet interaction [41]:

$$T_1 + T_1 \rightarrow S_1 + S_0 + \text{phonons} \tag{2.3}$$

This molecule interaction allows one of them to stay in the excited state S_1 whose decay causes the emission of radiation in the same way described above. Since the probability of this type of interaction is proportional to the square of the triplet state concentration [36], the lifetime of T_1 is long compared to the decay time of S_1. Therefore, the light is emitted after a delay time and generates the slow component of the light output of the scintillator, the one called phosphorescence.

Since S_1 decays to the excited vibrational states of S_0, the scintillator is transparent to its own radiation: in fact, the energy for the transition $S_0 \rightarrow S_1$ is larger than the energy emitted in the transition $S_1^* \rightarrow S_0^*$; in other words the emitted photons have a lower energy than the minimum required for the excitation.

Organic scintillators can be further divided into three main classes: organic crystals, liquid scintillators and plastic scintillators.

2.1.3.1 The Organic Crystal

The most common pure organic crystals are Anthracene ($C_{14}H_{10}$), Trans-Stilbene ($C_{14}H_{12}$) and Naphthalene ($C_{10}H_8$) [35]. Table 2.2 presents the main properties of these organic materials.

These crystals have the largest scintillation efficiency (defined as the fraction

Scintillator	**Density** (g/cm^3)	**Wavelength Emission** (nm)	**Decay Constant** (ns)	**Light Output** (% Anthracene)
Anthracene	1.25	448	30-32	100
Trans-Stilbene	1.16	384	3-8	46
Naphthalene	1.15	348	11	11

Table 2.2: Properties of several organic crystals [35]: in this case the light output is indicated as a percentage of the Anthracene one.

of the deposited energy that is emitted as radiation) of any organic scintillator [2] and also a fast time response of the order of a few nanoseconds (excluding Anthracene which has a decay time of the order of 30 ns).

Several drawbacks have to be listed:

- they have an anisotropic response due to the channeling effects; thus the response varies with the orientation of the crystal axis [2];
- they are hard crystals and relatively fragile;
- they are difficult to obtain in large sizes.

For these reasons, the most common use of the organic crystals is as solutes in liquid and plastic scintillators.

2.1.3.2 The Organic Liquid

The organic liquids are solutions of one or more organic scintillators (typically organic crystals) dissolved in an organic solvent. While the scintillation process is the same of the organic crystal one, the energy absorption mechanism is different. In solutions, in fact, the ionization energy is absorbed mainly by the solvent and then passed to the scintillation solute without radiation emission (non-radiative dipole-dipole interaction, known as Forster transfer). This transfer is very quick and efficient [42].

The most common materials used as solutes are p-Terphenyl ($C_{18}H_{14}$), PPO ($C_{15}H_{11}NO$) and POPOP ($C_{24}H_{16}N_2O_2$); among the solvents there are xylene, benzene and toluene [2]. The efficiency of liquid scintillators increases with the solute concentration.

This type of scintillators can be easily doped with other materials to increase the efficiency depending on the application. Materials which absorb light of one

[2] Anthracene is chosen as the reference to which the other scintillators light outputs are compared: thus the outputs are often expressed as a percentage of the Anthracene output.

frequency and re-emit it at another one (the so-called $wavelength\ shifters$) can be added in order to improve the compatibility with the spectral response of photodetectors. It is also possible to add atoms of boron in order to increase the efficiency for neutron detection. The doping may increase the decay time and decrease the light output due to a quenching effect.

Because of their lack of a solid structure which can be damaged by exposure to intense radiation, liquid scintillators are more resistant to radiation damage than crystalline or plastic scintillators [43].

2.1.3.3 The Organic Plastic

There are close similarities in the behavior of plastic and liquid scintillators. Plastic scintillators are similar in composition to the liquid ones being themselves solutions. The difference is that the solvent is a solid plastic material. The most efficient plastic solvents are the polymeric derivatives of alkyl benzenes (i.e. the most efficient liquid solvents) such as Polystyrene (PS), Polyvinyltoluene (PVT) and PolyMethylMethAcrylate (PMMA). Among the solutes one can list p-Terphenyl and PPO (like in liquid solutions); in order to increase the efficiency, a secondary solute (the POPOP) is often added in a small proportion for its wavelength shifting properties [35]. Table 2.3 presents the main properties of several organic plastic scintillators.

Scintillator	**Density** (g/cm^3)	**Wavelength Emission** (nm)	**Decay Constant** (ns)	**Refractive Index**
PS	1.05	492	3	1.60
PVT	1.03	423	2	1.58
PMMA	1.19	410	2.2	1.49
BC 414	1.03	434	1.8	1.58
BC 434	1.05	425	2.2	1.58

Table 2.3: Properties of some organic plastic scintillators [35]: the ones called BC 414 and BC 434 are produced by Bicron [44].

The main advantages of plastic scintillators are their fast response (∼2-3 ns, which allows to use them for trigger applications) and their flexibility. In fact they can be produced in a wide varieties of size and shape (such as bars, cylinders and also fibers).

Extruded Plastic Bars

As mentioned before, plastic scintillator detectors are one of the most used detectors in many applications of high energy physics. However, until the 1990s two main aspects made their use not convenient: the large construction cost even if the material was relatively inexpensive and the difficulty in collecting and transporting light (see section 2.1.4).

Motivated by the need of lower cost plastic scintillator for larger and larger detectors, many studies for improving the performance and quality of this type of scintillator have been performed since the end of the 1970s [45]. The extrusion technique has been introduced for the first time in 1980 and it is based on the passage of molten plastic through a die to obtain the desired cross-section shape and size. Every shape can practically be produced with the extrusion technique: figure 2.5 presents two examples of dies for the extruded bars production while

(a) (b)

Figure 2.5: Dies to produce the MINERνA a) triangular and b) rectangular bars [46].

figure 2.6 an example of the extruded bar.

The first polystyrene-based scintillators produced with this process resulted to have a good light yield but a poor attenuation length[3] [47]. This problem was solved in the early 1990s, when wavelength shifting (WLS) fibers became commercially available and were used in several scintillation detector applications: in this way the requirement for a long attenuation in the scintillator became less important.

[3]The attenuation length, or absorption length, is defined as the distance after which the light intensity is reduced of a factor $\frac{1}{e}$.

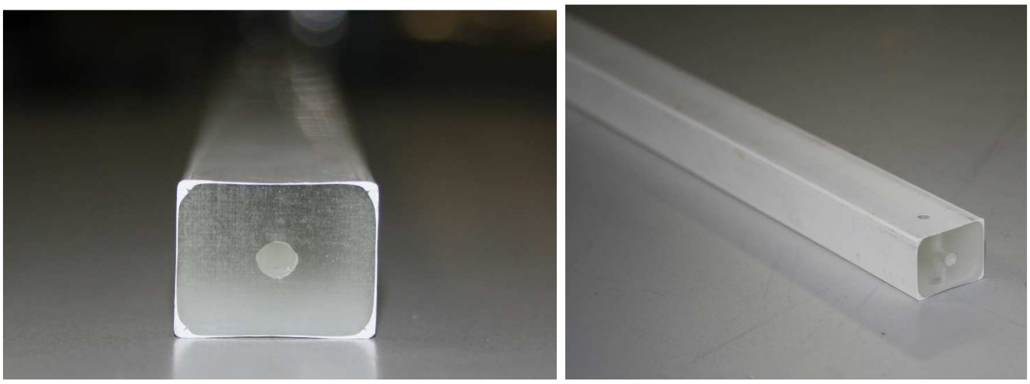

(a) (b)

Figure 2.6: An example of an extruded scintillating bar with a hole for the WLS fiber insertion.

The Scintillation Detector Development Technical Center at Fermilab has produced extruded plastic scintillators for several experiments such as MINERνA [46], T2K [48], MUSASHI [49] (discussed in detail in section 2.2) and EMR [50] (at MICE). For a detailed description of the manufacturing technique of extruded scintillators see [45, 51].

The extrusion technique is based on the use of pellets or powder made of polystyrene, which are rather inexpensive materials. Initially the extrusion process consisted in two steps: the dopants (typical quantities are 1% PPO and 0.03% POPOP) were added to commercial scintillating pellets in order to produce scintillating polystyrene pellets. These materials were pre-mixed and then added to the extruder with the desired shape and a hole in the middle (which can host the WLS fiber) [51]. Figure 2.7(a) presents a scheme of this first production method. An alternative method (figure 2.7(b)) is a continuous in-line compounding and extrusion process. In this case, polystyrene pellets and dopants are directly put into the extruder with the correct rate to obtain the required scintillator mixture: a particular scintillator profile is thus produced starting from polystyrene pellets [45]. This second method allows to produce plastic scintillators with a high quality and homogeneity.

2.1.4 The Light Collection

Once the scintillating light has been produced in the detector, it has to be transmitted as efficiently as possible to the photodetectors in order to create an electric signal. There are two effects that can reduce the light collection [1]:

- the light loss at the scintillator surfaces: since the light emitted by a scin-

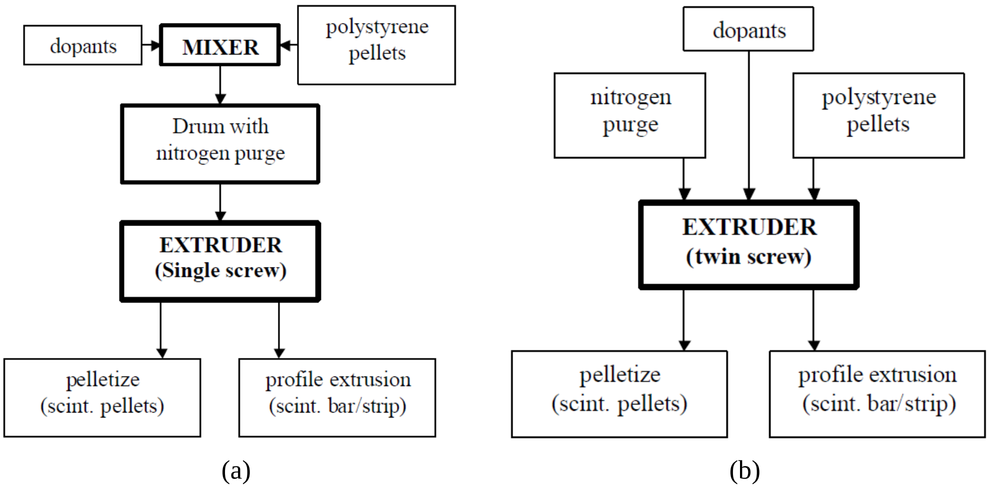

Figure 2.7: a) The two-steps extrusion technique and b) the continuous in-line extrusion process [45].

tillator is isotropic, only a limited fraction can travel directly to the surface where the photodetector is placed. A large fraction of the photons have to be reflected from the scintillator surfaces towards the correct direction. Considering a critical angle Θ_C defined by Snell's law:

$$\Theta_C = \sin^{-1}\frac{n_1}{n_0} \tag{2.4}$$

where n_0 is the refractive index of the surrounding material and n_1 the refractive index of the scintillating plastic, two different situations can occur (as shown in figure 2.8). When the light reaches the surface with an inci-

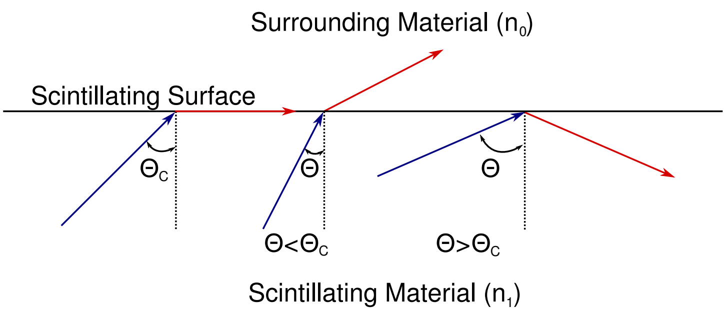

Figure 2.8: Schematic view of the two different situations at the scintillator surface: if $\Theta < \Theta_C$ the light escapes, while if $\Theta > \Theta_C$ photons are internally reflected.

dence angle Θ larger than the critical angle Θ_C, the total internal reflection occurs. On the other hand, if $\Theta < \Theta_C$ a partial transmission through the surface takes place and photons are lost. In order to recover at least part of the "lost" light, the scintillator surfaces are typically painted with a reflective material;

- the optical self-absorption. Even if the scintillation materials are reasonably transparent to their own radiation, if the detectors are very large self-absorption is not negligible. Defining the light attenuation length (l) as the distance after which the light intensity is reduced by a factor $1/e$, the light intensity can be expressed as

$$L(x) = L_0 e^{(-\frac{x}{l})} \tag{2.5}$$

  where x is the path length of the light and L_0 the initial light intensity. With a typical attenuation length of the order of 1 m or even more, only very large detectors are affected by such a problem. Moreover, this effect can be further reduced by adding a wavelength shifter component (able to absorb the scintillation light and shift it to a longer wavelength) to the basic scintillator one.

The layout of the experiment or the presence of a magnetic field may prevent from the possibility of coupling directly the photodetector to the scintillator, thus requiring the presence of a *light guide* [52] usually made of optical Plexiglas. The light guides can be of various shapes and sizes, as shown in figure 2.9.

Figure 2.9: Several examples of different shapes of light guides used for the collection of the light produced in a scintillating plastic detector [53].

2.1.4.1 The Scintillating Fibers

As mentioned before, in the early 1990s a new light collection method (used especially in extruded detectors) was introduced: the WaveLength Shifter (WLS) fibers. They are thin optical fibers [54] made of plastic scintillator, with a typical thickness from 0.25 mm to 5 mm and square or round cross-sections.

In general, a WLS fiber has a central core made of Polystyrene[4] (characterized by a refractive index n_{core}=1.60) and an outer cladding region made of PolyMethylMethAcrylate (PMMA), as shown in figure 2.10(a). The core of an optical fiber contains a wavelength shifter dopant: the light absorbed from the detector is then re-emitted isotropically with a different wavelength [55].

In order to allow the light transport via the total internal reflection inside the core, the cladding material has a lower refractive index (n_{clad}=1.49). In this way, the internal reflection occurs at the interface between the fiber core (the region with a high refractive index) and the fiber cladding (the low refractive index region), as shown in figure 2.10(b). The internal reflection is produced only if the

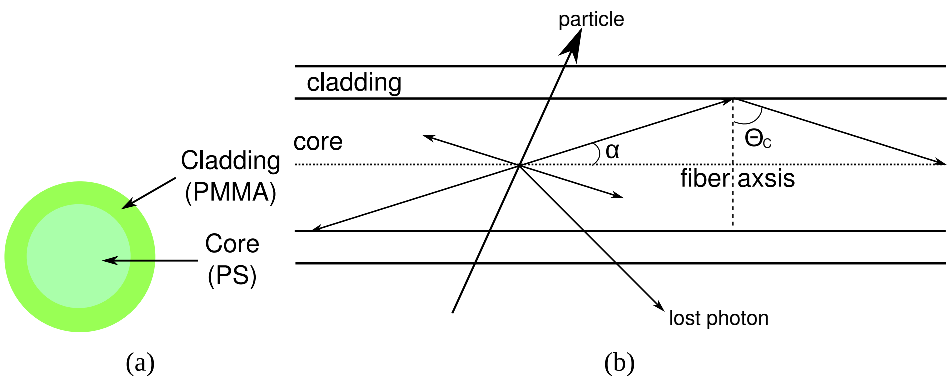

Figure 2.10: Schematic view of a) a single-cladding fiber and b) its light transport mechanism (internal reflection). The fiber core is made of Polystyrene (n_{core}=1.60) while the cladding of PMMA (n_{clad}=1.49).

angle of the light is larger than the critical angle (typically $\Theta_C \simeq 70°$). This angle is determined by equation 2.4 (Snell's law) using as n_0 the core refractive index and as n_1 the cladding one. In this way, just the photons emitted by the core with an angle (α) on the fiber axis less than $\alpha_C = \pi/2 - \Theta_C$ are reflected within the core. The light emitted with $\alpha > \alpha_C$ may exit from the core fiber and should be absorbed by an Extra Mural Absorber (EMA), which is an additional opaque layer whose function is to limit the crosstalk with the nearby fibers.

[4]Even if Polystyrene has a lower mechanical strength, the choice to use this material is due to its being easily extruded, simplifying the fiber production process.

In order to reduce the critical angle and increase the efficiency of the light collection, a particular type of scintillating fiber (the $double-cladding$ fibers) has been developed. A second cladding made of a material with a different refractive index (typically Fluor-Acrylic with $n_{clad\ out}$=1.42) is added to the standard fiber structure. Figure 2.11(a) presents a schematic view of the double-cladding section, while figure 2.11(b) shows the light transport mechanism of these fibers: in this way, Θ_C increases up to 73°.

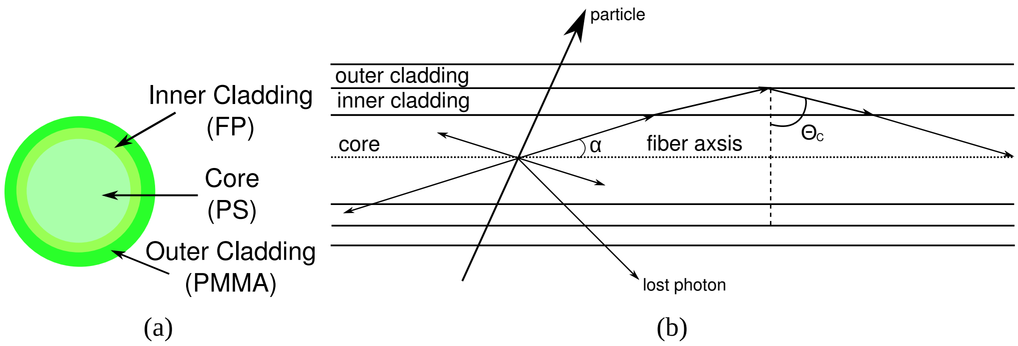

Figure 2.11: Schematic view of a) a double-cladding fiber and b) its light transport mechanism.

The intermediate cladding (called inner cladding) has to provide the mechanical bonding between the Polystyrene and the outer cladding: the reason for not applying the outer cladding directly on the Polystyrene core is the lack of adhesive force between this cladding and Polystyrene. The use of multi-cladding fibers offers two main advantages over single-cladding ones [56]:

- there is an improvement in the detection photoelectron yield;
- the double-cladding fibers are more flexible and robust.

The introduction of this new light collection method allows to separate the different tasks. While the detector performances are optimized for the radiation detection, the WLS fibers are used to collect the photons (produced by the scintillator itself), re-emit them at different wavelengths and transport the light to the photodetector: in this way, the collection efficiency increases considerably [55]. The use of scintillating fibers as a light collection system gives other advantages:

- the possibility to transfer the light at a long distance allowing the construction of very large detectors without the problem of light attenuation;
- a better matching with the very small area of some of the light detectors, thanks to the small diameter of the fibers themselves;

- the possibility to build compact detection systems without the use of light guides.

2.2 The Scintillating Bars Experiments

In this section, three detectors based on scintillating extruded bars are described:

- the MINERνA experiment [46, 57] for the study of the neutrino oscillation;
- the ASACUSA tracker [49, 58] for the reconstruction of the anti-hydrogen (or anti-proton) annihilation vertex;
- the monitor of the T2K neutrino beam features [48, 59].

The near detector of the T2K experiment will be discussed in detail since all its sub-detectors are based on scintillators readout by Silicon PhotoMultipliers.

2.2.1 The MINERνA Experiment

The NuMI neutrino facility at Fermilab (which is designed for the MINOS neutrino oscillation experiment [60] and based on the Main Injection (MI) accelerator) provides an extremely intense beam of neutrinos. MINERνA (figure 2.12(b)) is a high statistics neutrino scattering experiment installed on the NuMI beamline, more precisely it is placed directly in front of the MINOS Near Detector. Its main goal is the precise measurement of the quasi elastic neutrino-nucleus cross-section in the 1-10 GeV energy range [46], to improve the knowledge about neutrino interactions at low energy and their dependence on the mass number (A).

Figure 2.12(a) presents a front view of the MINERνA detector, which consists of a totally active scintillating bars detector (where precise tracking, low density of material and fine sampling allow to perform different measurements) and a calorimeter. The scintillator detector (called inner detector, ID), in fact, does not fully contain events (because of its low density and low Z) and therefore it is surrounded by a sampling calorimeter (the outer detector, OD), which is made of six trapezoidal towers of scintillator and steel layers [61]. The inner detector consists of several parts and sub-detectors with different functions (as shown in figure 2.13): the nuclear target, the fully active target, the downstream electromagnetic calorimeter (ECAL) and the hadron calorimeter (HCAL).

Both the inner and outer MINERνA detectors are made of extruded plastic scintillating bars which have a Polystyrene core (Dow Styron 663 W) doped with PPO (1% by weight) and POPOP (0.03% by weight) [46] and a reflective coating of TiO_2 to reflect the escaping light. The OD bars have a rectangular cross-section

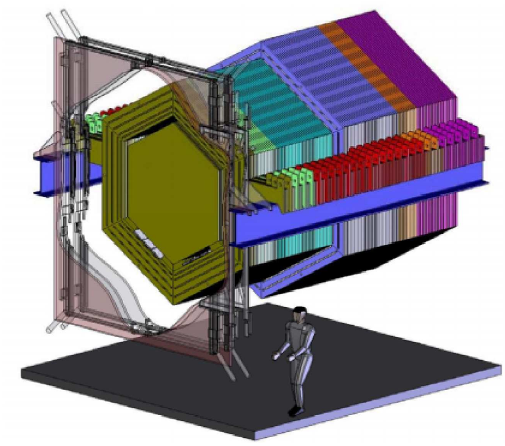

(a)

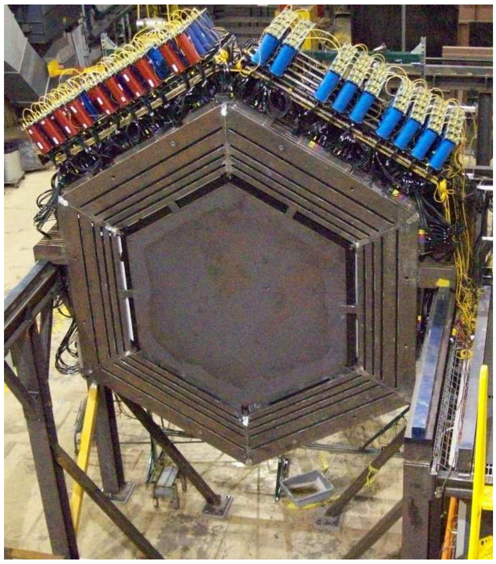

(b)

Figure 2.12: a) A 3D scheme and b) a front view photo of the MINERνA detector: it consists of a totally active scintillating bars detector surrounded by a sampling calorimeter made of trapezoidal towers.

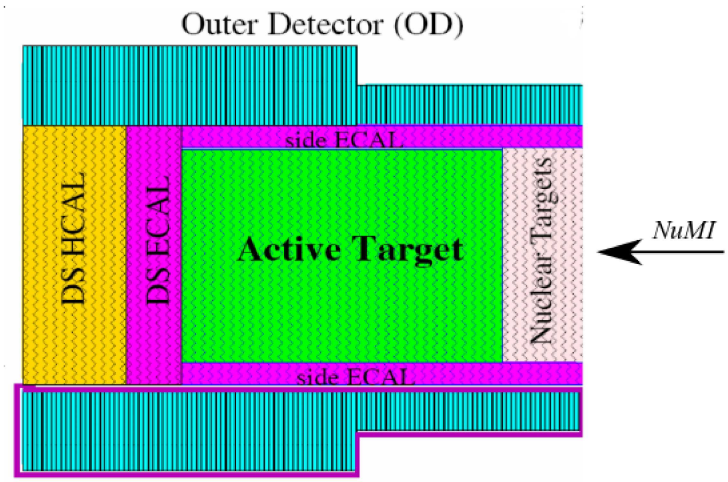

Figure 2.13: A 2D slice of the MINERνA OD and ID: all the ID sub-detectors are indicated [57].

of 1.9×1.5 cm^2; the active target bars have an isosceles triangular profile with a base of 3.3 cm and a height of 1.7 cm (figure 2.14(a)). In both cases, in the middle of the bar there is a 2.6 mm hole to insert the WLS fiber. The ID bars are cut at different lengths, arranged to form a hexagon and assembled as shown

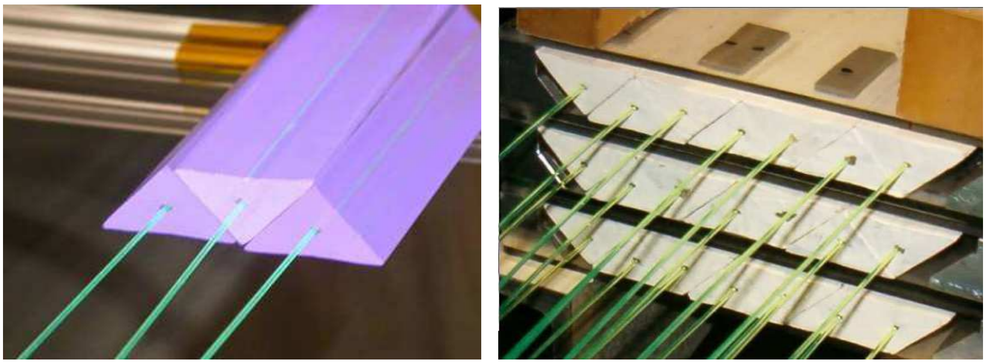

(a) (b)

Figure 2.14: a) The MINERνA scintillating bars with the wavelength shifter fibers and b) three ID layers.

in figure 2.14(b) in order to allow the charge sharing between the neighboring bars of a single layer: a spatial resolution of 2.65 mm (figure 2.15(a)) has been measured [57].

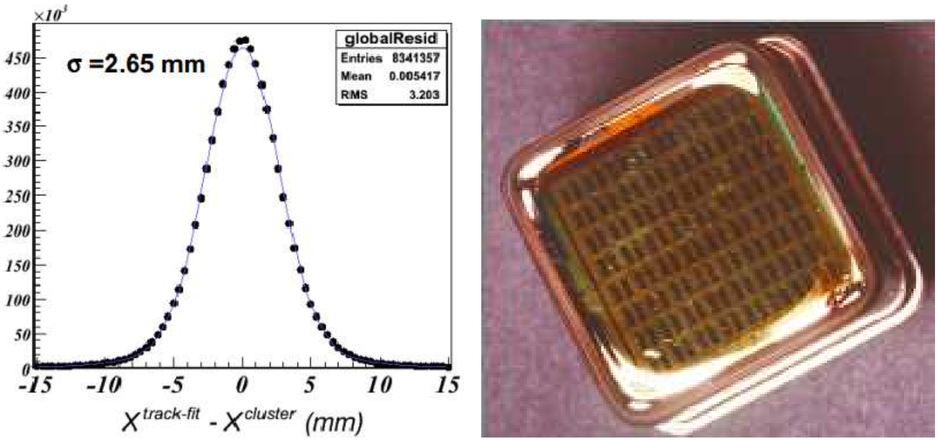

(a) (b)

Figure 2.15: a) The fully active detector spatial resolution and b) the Hamamatsu MAPMT used for the readout.

The scintillation light produced by an incident charged particle is collected by a wavelength shifter fiber, which is inserted and glued (with an optical epoxy glue increasing the light yield by a factor 1.5) in the hole of each bar. Only one fiber side is readout by 473 Hamamatsu 64-channels MAPMTs (figure 2.15(b)), while on the other side a mirror is placed in order to maximize the light collection.

The first MINERνA module was completed in the early 2006, and the first events were observed by the partially assembled detector in April 2009. From November 2009 to March 2010 MINERνA has run with a low-energy anti-neutrino beam while until March 2012 with a low energy neutrino beam. It is also scheduled that for the beginning of 2013 the beam energy will be increased.

2.2.2 The ASACUSA Experiment

ASACUSA (Atomic Spectroscopy and Collision Using Slow Antiprotons) is an experiment for the study of the antiproton-nuclei cross section and the high precision spectroscopy of anti-hydrogen atoms. The experimental setup for the anti-hydrogen synthesis is composed as follows [49] (figure 2.16):

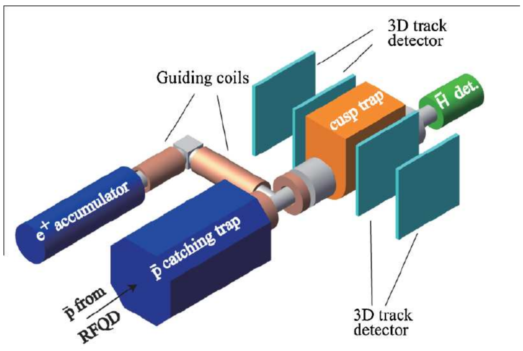

(a)

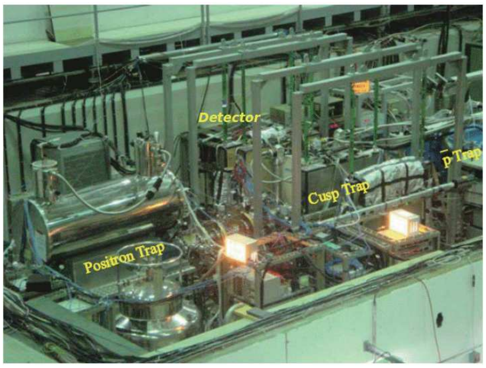

(b)

Figure 2.16: The ASACUSA experimental setup: a) a 3D schematic view and b) a top view photo. The main components are the MUSASHI anti-proton accumulator and the positron one, the cusp-trap and the 3D tracker detector [49].

- the MUSASHI anti-proton accumulator;
- the positron accumulator;
- the cusp-trap where (thanks to its trapping potential) anti-protons and positrons are captured and form the anti-hydrogen atoms;
- the 3D tracker detector used to monitor the annihilation position.

2.2.2.1 The 3D Tracker Detector

In order to reconstruct the exact cusp-trap conditions in which the anti-hydrogen synthesis can occur, an on-line monitoring of the particles behavior inside the trap has been developed. The 3D tracker is able to reconstruct the anti-hydrogen (or anti-proton) annihilation vertex in the cusp-trap detecting the annihilation products (which are typically π mesons) given that its 4 modules are placed in pairs on each side of the cusp-trap (figure 2.17).

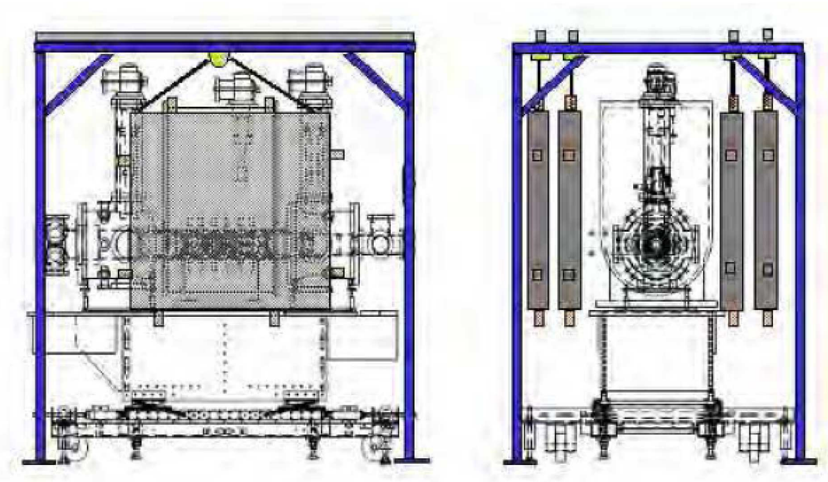

(a)

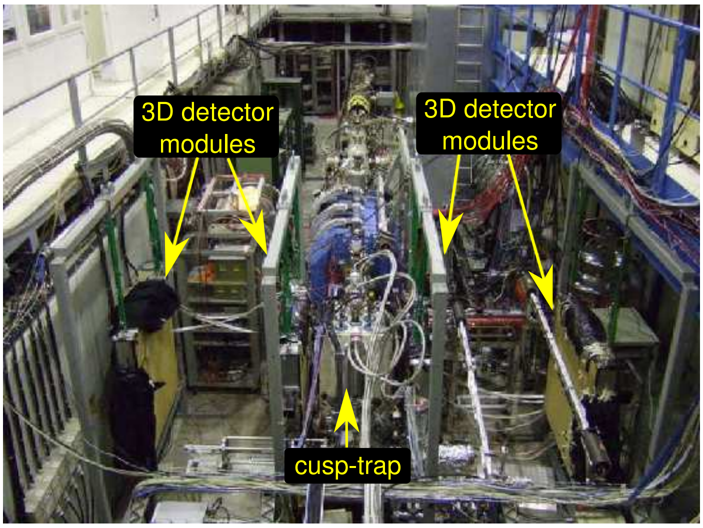

(b)

Figure 2.17: The ASACUSA 3D tracker: a) a sketch of the side and front view and b) a photo of the tracker modules placed in pairs on each side of the cusp-trap [49].

As shown in figure 2.18(a), each module consists of two layers in the $x - y$ configuration; each layer is made of 64 bars (the same of the MINERVνA ones) of plastic scintillator with a rectangular cross-section of 1.5×1.9 cm^2 and 96 cm long [58]. In each bar there is a central hole with a 2 mm diameter for the intro-

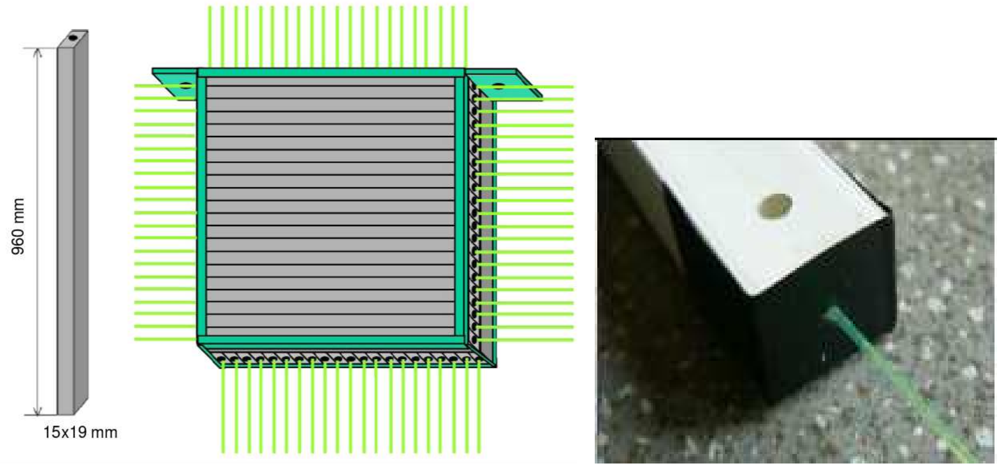

(a) (b)

Figure 2.18: a) The ASACUSA tracker module with its two layers in a $x - y$ configuration and b) a bar with a glued WLS fiber in the central hole.

duction of a WLS KURARAY green fiber which is used for the light collection (figure 2.18(b)).

The 64 fibers of one plane are readout with a single photomultiplier on one side while on the other one they are interfaced to two Hamamatsu 64-channel PMTs: in this way only 32 out of 64 available pads of the PMT are coupled to the fibers in order to reduce the crosstalk effects [53].

Before the assembly of the detector in the experimental area, the performance of all the 4 modules have been tested: figure 2.19(a) presents the spatial resolution ($\leq$ 1 cm) while figure 2.19(b) the efficiency of one module for different values of the PMTs bias [53].

2.2.3 The T2K Experiment

T2K (Tokai to Kamioka) is a long-baseline neutrino-oscillation experiment: its main goal is to precisely measure the neutrino oscillation parameters using an off-axis muon neutrino beam produced by the proton beam of the J-PARC synchrotron. Figure 2.20 presents the basic elements of the T2K experiment:

- a Near neutrino Detector (the ND280) placed at 280 m from the neutrino facility which measures the spectra and the fluxes of the muon neutrinos before they have the possibility to oscillate. It consists of two different detectors called on-axis and off-axis (which will be discussed in detail in this

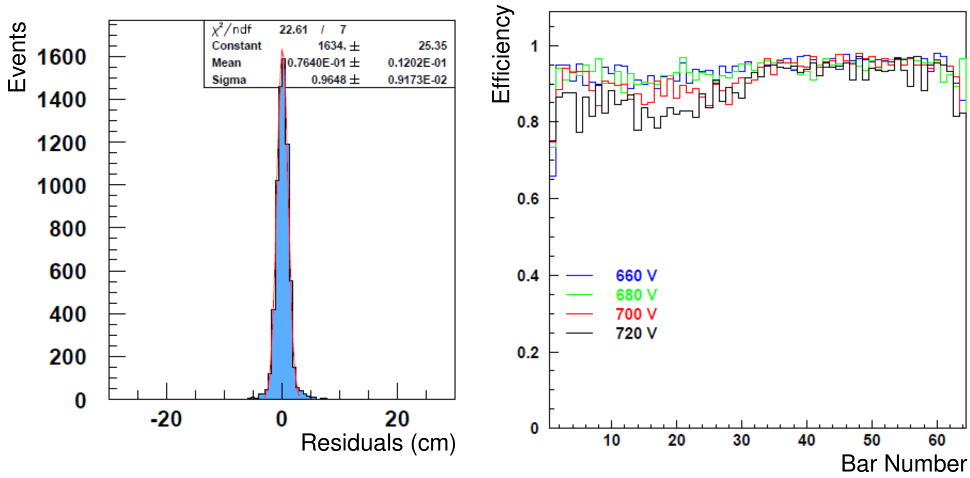

(a) (b)

Figure 2.19: A layer of the ASACUSA tracker: a) the spatial resolution and b) the efficiency (evaluated for different PMT bias voltages) [53].

section) [48] both based on scintillating bars detectors readout by Silicon PhotoMultipliers;

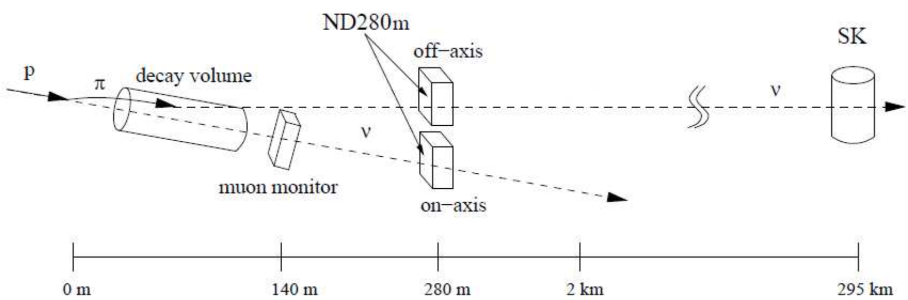

Figure 2.20: Schematic view of the T2K experiment: the basic elements are the neutrino beam line, the ND280 near detector and the Super-Kamiokande far neutrino detector [59].

- a far detector (called Super-Kamiokande) which is placed at 295 km from the beam production. It measures the unknown mixing angle θ_{13} by observing the $\nu_\mu \to \nu_e$ oscillation distinguishing ν_μ and ν_e through the Cherenkov emission of electrons and muons. The Super-Kamiokande detector, in fact, is a 50,000 tons ultra-pure water Cherenkov detector with 11,146 photomultiplier tubes [62].

2.2.3.1 The On-axis Near Detector

INGRID (Interactive Neutrino GRID) is the neutrino ND centered on the neutrino beam axis designed to monitor directly the ν_μ beam direction (with a precision better than 1 mrad) and intensity [63]. As shown in figure 2.21(a), the INGRID detector consists of 14 modules placed around the beam center and organized in two groups (7 modules are in the horizontal direction and 7 in the vertical one) and of other 2 modules placed off-axis with respect to the cross configuration. The overall area covered by the INGRID detector is about 10×10 m^2.

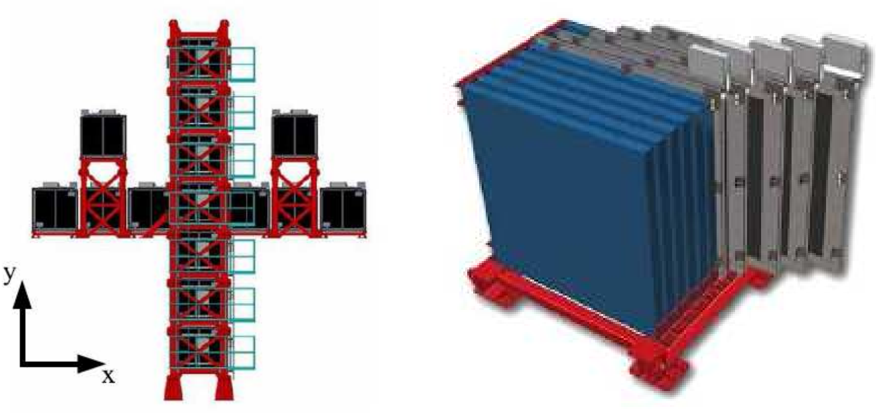

(a) (b)

Figure 2.21: a) The ND280 on-axis detector (INGRID) and b) a INGRID module where the tracking layers (in blue) and the iron ones are shown [48].

Each INGRID module consists of 11 tracking scintillator layers and 10 iron planes (with a dimension of 124×124 cm^2 and 6.5 cm thick along the beam direction) as shown in figure 2.21(b). On the top and sides of each module, other scintillating layers are used as a veto. Each tracking layer is composed of two layers (a vertical and a horizontal one) of 24 $1\times5\times120$ cm^3 extruded scintillator bars with a 3 mm hole in the middle [63]. The bars are made of Polystyrene doped with 1% PPO and 0.03% POPOP. The scintillation light collection is performed by 1 mm diameter KURARAY double-clad WLS fibers, which are characterized by an absorption spectrum centered at 430 nm (blue region) and an emission one centered at 476 nm (green region) [48]. Each fiber is readout by a Hamamatsu MPPC (described in section 2.2.3.3)

The INGRID modules have been tested with cosmic rays: the average light of each channel is measured to be larger than 10 photoelectrons per cm of MIP tracks and the timing resolution is about 3.2 ps [48]. Figure 2.22 presents a neutrino beam profile obtained with the INGRID detector.

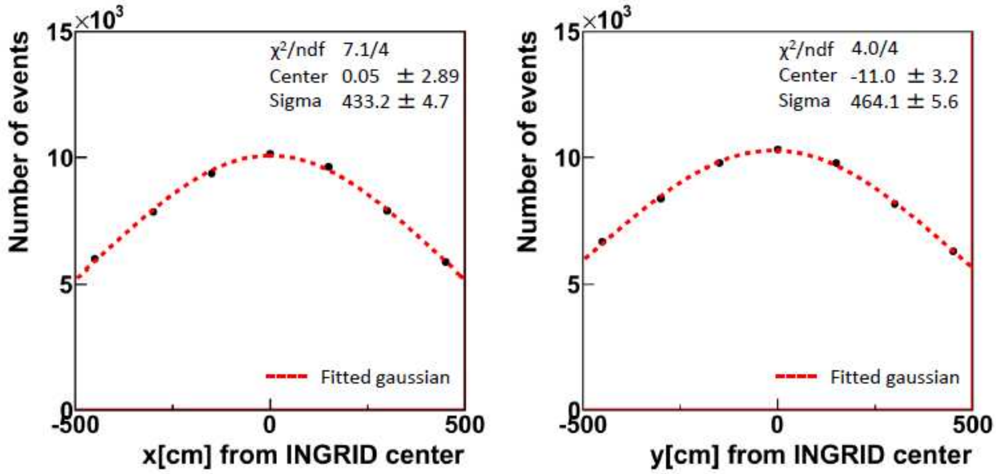

Figure 2.22: The INGRID ν beam profile in both directions (x and y) [63].

2.2.3.2 The Off-axis Near Detector

The goal of the T2K off-axis near detector is the measurement of the flux, the energy spectrum and the ν_e contamination in the direction of the far detector. These measurements allow to characterize signals and background in the Super-Kamiokande detector [48]. The off-axis ND280 consists mainly of five different parts (as shown in figure 2.23):

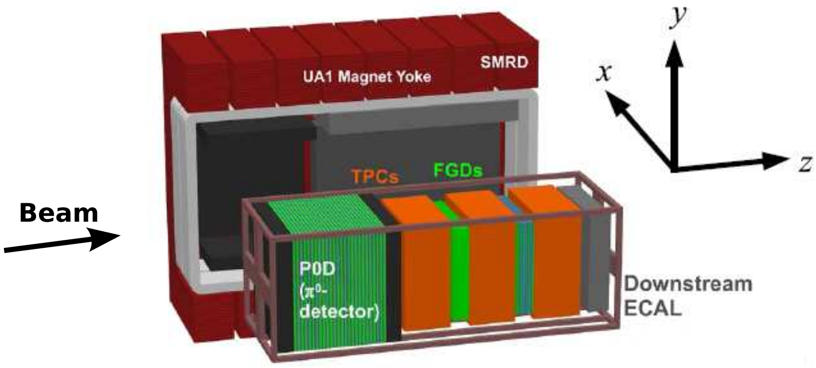

Figure 2.23: Schematic view of the ND280 off-axis detector: all the sub-detectors are indicated [48].

- the UA1 magnet providing a dipole magnetic field of 0.2 T allows to measure the charged particle momenta with a good resolution and determine the sign of the particle produced in the neutrino interactions;

- the Pi-Zero Detector (P0D) designed to measure the rate of the neutral current process (in which a π^0 is produced):

$$\nu_\mu + N \rightarrow \nu_\mu + N + \pi^0 + X \quad (2.6)$$

This detector is composed by 40 scintillator modules, each made of two scintillating bars layers in a $x - y$ configuration, and interleaved with water target layers as shown in figure 2.24(a). The P0D scintillating bars have an isosceles triangle cross-section with a base of 3.3 cm base and a height of 1.7 cm: in the middle they have a hole with a diameter of 1.5 mm where WLS fibers can be inserted;

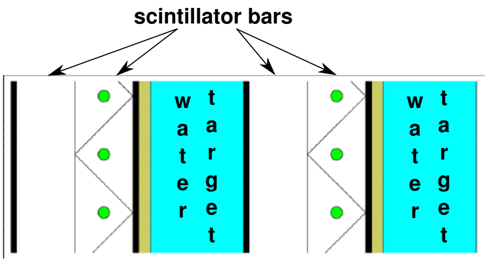

(a)

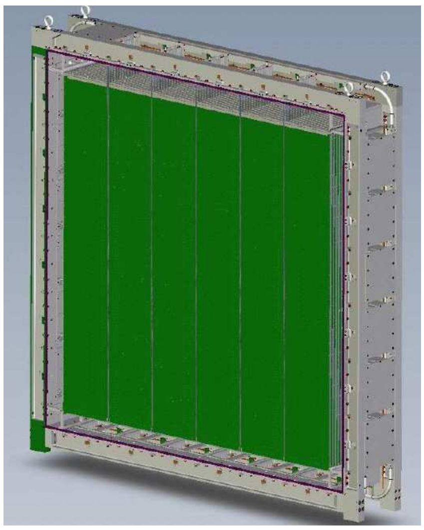

(b)

Figure 2.24: A schematic view of a) the P0D (with triangular bars and a water target) and b) the FGD where the green area is the scintillator detector [48].

- the ND280 tracker which consists of 3 Time Projection Chambers (TPCs) and 2 Fine Grained Detectors (FGDs): the main goal of this system is to measure the ν_μ and ν_e beam flux and energy spectra. The main reason of the choice of the TPCs is their capability to perform the 3D imaging of the particle tracks, the measurement of the momenta of the charged particles produced by the neutrino interactions (occurred in other parts of the detector) and also the identification of the different types of charged particles through dE/dx measurements.

The two fine grained detectors consist of finely segmented scintillating bars which provide the target mass for the neutrino interaction as well as the tracking of the charged particles. The first FGD is a totally active scintillating detector (similar to the SciBar detector [64]) which consists of about 5760 extruded Polystyrene scintillating bars (with a dimension of 0.96×0.96×186.4 cm^3) arranged into 30 layers oriented in either the x or y direction. In each bar there is a hole for the insertion of a WLS fiber: one end of the fiber is readout by a MPPC (see section 2.2.3.3) while the other end is mirrored by the vacuum deposit of aluminum in order to increase the light yield [48]. The second FGD is a water-rich detector consisting of 7 $x - y$ modules of plastic scintillator alternating with six layers of water which is maintained under sub-atmospheric pressure by a vacuum pump system.

Figure 2.25 presents an event display (reconstructed by the ND280 tracker) of a muon which enters into the P0D and crosses the tracker region producing secondary particles which are stopped in the ECal;

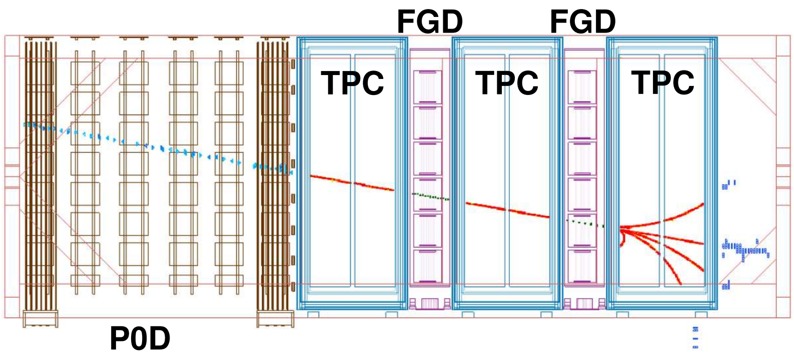

Figure 2.25: A muon event in the ND280 tracker: the muon crosses the P0D continuing to the tracker region and producing secondary particles (which are stopped in the ECal) [48].

- the ECal is a sampling electromagnetic calorimeter surrounding the inner detectors (P0D, TPCs and FGDs): it is made of plastic scintillating bars (with a 4×1 cm^2 cross-section) arranged in 32 layers (the calorimeter active area) and separated by 31 layers of 1.75 mm thick lead sheets. As in the INGRID bars, a 1 mm diameter fiber runs along the hole in the center of each bar, but in the ECal case the fibers are readout in two different ways: with a double-end readout if the fiber has a MPPC at each end or with a single-end readout if one end of the fiber is readout by a MPPC and the other end is mirrored. Its main purpose is to measure those photons produced and not stopped in the inner detectors and its energy resolution has been measured to be about $7.5\%/\sqrt{E(\mathrm{GeV})}$ for energies up to 5 GeV;

- the Side Muon Range Detector (SMRD) which detects muons (created in the neutrino interactions) escaped at large angles with respect to the neutrino beam and it is also used as a trigger for cosmic ray muons that cross the ND280 detector. The SMRD consists of a total of 440 scintillator modules which are inserted in the air gaps between the steel plates of the UA1 magnet yoke. As shown in figure 2.26, the SMRD scintillating bars are char-

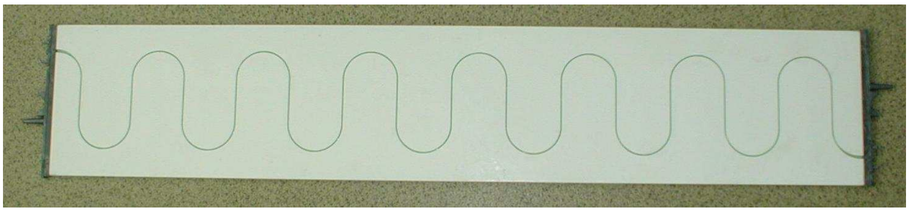

Figure 2.26: Scintillating bar of the ND280 SMRD: the S-shaped groove with embedded the WLS fiber (needed for the light collection) is visible.

acterized by a S-shaped groove for the insertion of the WLS fiber which is coupled with a MPPC at both ends.

2.2.3.3 The T2K Photodetectors

In the ND280 detectors, the scintillation light is collected by WLS fibers and carried out to photodetectors: MAPMTs (successfully used in other scintillator based neutrino experiments) are not suitable for ND280 because of the presence of the magnetic field and also because of the limited space (considering that ND280 has $\sim$50,000 channels). A particular type of silicon photomultiplier, the Multi Pixel

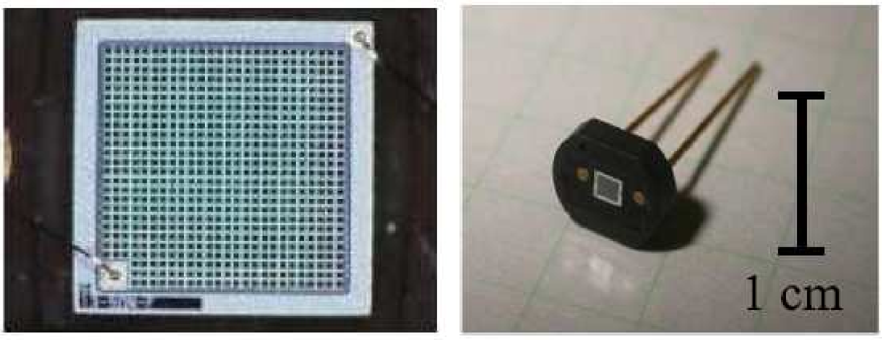

Figure 2.27: The Hamamatsu MPPC used for the readout of all the ND280 scintillating detectors.

Photon Counter (MPPC), has been designed specifically for the T2K experiment by Hamamatsu Photonics [65]. Figure 2.27 presents an example of the MPPC while table 2.4 summarizes its main features.

Number of Pixel	667
Pixel Size	$50\times50\ \mu\text{m}^2$
Active Area	$1.3\times1.3\ \text{cm}^2$
Operating Voltage	68-71 V
Gain	$\sim10^6$
Photo Detection Efficiency	$\geq$25%
Dark Rate	$\sim$1 MHz

Table 2.4: Main features of the MPPCs used in the ND280 detectors [48].

2.3 A Different Approach to the SiPM Readout

As already stated, the T2K collaboration has developed an experiment based on scintillating bars detectors readout by Hamamatsu Silicon PhotoMultipliers.

A different approach has been chosen by an Italian R&D project called FACTOR (Fiber Apparatus for Calorimetry and Tracking with Optoelectronic Readout) [66] which has evolved in TWICE (Techniques for Wide-Range Instrumentation in Calorimetry Experiments). The FACTOR/TWICE goal is the development of a new type of SiPM and its use in several physics fields. The project is funded by the Italian Institute for Nuclear Physics (INFN, Istituto Nazionale di Fisica Nucleare) and actively collaborates with FBK-irst[5] (Fondazione Bruno Kessler) for the SiPM design and production. The large dynamic range and low noise SiPMs are readout by commercially available ASICs to develop a readout system for calorimetry applications.

This thesis work intends to evaluate the readout system performance based on SiPMs with respect to the one exploiting MAPMTs: in order to compare the results, both the systems are readout with the same frontend board. In particular, the tests have been performed using two prototypes of the MICE Electron Muon Ranger (EMR) detector: the small one has been tested with cosmic rays (the results are presented in chapter 3) while the second one (the Large EMR Prototype, LEP) has been used to detect both cosmic rays and a particle beam at CERN (see chapter 4 and 5 for further details). The spatial resolution, the detection efficiency and the timing resolution of the first prototype have been measured exploiting a small number of SiPMs, while the performance of a large number ($\sim$200) of these devices has been evaluated with LEP.

[5] Fondazione Bruno Kessler, now Advansid (Trento-Italy): *http://www.fbk.eu*

Chapter 3

The Small EMR Prototype with a SiPM readout

The comparison of the SiPM performance with the MAPMT one has been studied with two detectors. Both the systems are prototypes of the MICE Electron Muon Ranger developed by the Como/Trieste group to study either the EMR performance as a tracker (with the small scale EMR prototype [67]) or as a calorimeter (with the Large EMR Prototype [50]). The two detectors are based on scintillating bars whose light is carried out by WLS fibers and have been tested with cosmic rays and particle beams.

This chapter deals with the description of the small EMR prototype and its performance: the first part is devoted to a brief review of the MICE experiment, its goals and its different components (focusing in particular on EMR) to move then to the prototype features. In the second part the evaluation of the spatial resolution, the detection efficiency and the timing resolution obtained with cosmic rays is provided.

The LEP description and the results obtained with this prototype are presented in chapter 4 and 5.

3.1 The MICE Experiment

Neutrino physics has a fundamental role in modern physics given the study of oscillation phenomena may lead to an evidence of new physics beyond the Standard Model. Both natural and artificial neutrino sources exist: from the sun and the cosmic rays to nuclear reactors and particle accelerators.

In recent years a new artificial neutrino source has been proposed: the Neutrino Factory. In a Neutrino Factory the ν beam is produced by the decay of stored muons: since the muon decay is a well-understood decay, the neutrino beam of a

Neutrino Factory would have well-known features in terms of energy and intensity allowing the optimization of the detector (which is one of the hard tasks given the very small interaction cross-section of neutrinos).

The international Muon Ionization Cooling Experiment (MICE) is being commissioned at the Rutherford Appleton Laboratory (RAL, UK); its main goal is to evaluate the possibility of producing a muon beam with adequate features for a Neutrino Factory based on a muon storage ring. The muon beam of the MICE experiment is produced by the ISIS synchrotron protons (with an energy of 800 MeV) which hit a titanium target and produce pions that in turn decay generating muons (with a momentum in the 140-240 MeV/c range) [68]. The beam obtained from the pion decay has a large emittance (that is defined as the volume of the beam in the phase-space): the MICE experiment intends to demonstrate the possibility of using the ionization cooling to reduce the muon beam emittance. In fact, because of the muon short lifetime ($\tau_\mu = 2.2 \times 10^{-6}$ s), the standard cooling techniques (for example the electron or stochastic cooling) are not effective if applied to muon beams. The ionization cooling, which represents the only possible solution, consists of two different phases: the muon beam with a large emittance crosses an absorber section and loses momentum (both the transversal and longitudinal one) through the ionization interactions with atomic electrons. The lost energy longitudinal component is then restored by accelerating cavities: the net result is a reduction of the transversal momentum which reduces the particle emittance [69].

In order to achieve its goals, the MICE experiment has to design and build a cooling section and characterize the muon beam before and after this section. Its main elements are (figure 3.1):

- the muon beam $cooling\ channel$, based on a liquid hydrogen absorber and RF structures;
- the scintillating fibers $spectrometers$ placed in solenoids of 4 T and used to measure the emittance before and after the cooling channel (tracking each muon track);
- the $particle\ ID\ section$ with its $calorimeter\ station$ (placed at the end of the MICE line) which allows to distinguish muons from other particles (i.e. the background consisting mainly of pions and electrons).

The experiment intends to reduce the beam transverse emittance by a factor larger than 10% which requires to measure the emittance before and after the cooling section with an absolute precision of 0.1% [68]. To achieve this precision, a very high muon identification purity (equal to 99.99%) is required both upstream and downstream of the cooling channel: for this reason, at the end of the MICE line

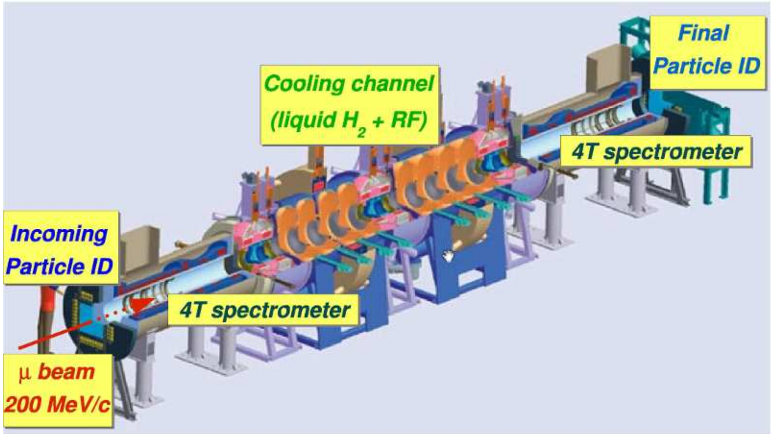

Figure 3.1: The MICE layout: the muon beam comes from the left and crosses the upstream particle ID and spectrometer, the cooling channel, the downstream spectrometer and particle ID [67].

(i.e. after the cooling section) a particle ID has been foreseen mainly to discriminate muons from electrons (produced in the decay of the muons themselves). This detector consists of an electromagnetic Pb-scintillating fiber pre-shower calorimeter [70] (KLOE-Light) and a totally active scintillating bar tracker-calorimeter (the Electron Muon Ranger EMR, described in the next section) [71].

3.1.1 The EMR Detector

Figure 3.2 shows a schematic view of the EMR detector, which consists of 48 layers arranged in a $x - y$ geometry.

As shown in figure 3.3(a), each layer is made of 59 1.1 m long scintillating bars with a triangular shape[1] (base of 3.3 cm and height of 1.7 cm, figure 3.3(b)). The bars are made of blue-emitting DOW Styron 663 Polystyrene with 1% PPO and 0.03% POPOP dopants and characterized by an emission cut-off of 400 nm and an emission peak of 430 nm.

The light produced in each bar is collected by one 1.2 mm BCF-92 WLS fiber, that is a double-cladding fiber with an emission peak at 492 nm (i.e. it is a blue to green shifter). Each fiber is inserted in the bar hole, glued with transparent glue and fixed at the ends of the scintillator bar itself with two particular connectors. The light is carried out to the PMTs by two separate clear fibers which are covered with a dark plastic to avoid the fiber crosstalk effect and to protect the fibers

[1] After the study performed with the prototype bars [72], the triangular shape has been preferred to the rectangular one to reduce the inefficiency effects due to the non perfect planarity of the contiguous edges of the bars.

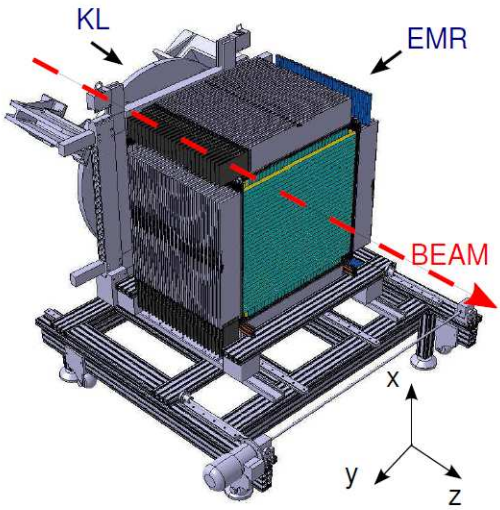

Figure 3.2: a) A schematic view of the Electron Muon Ranger which consists of 48 layers (in a $x-y$ geometry): the beam direction is defined along the z axis [50].

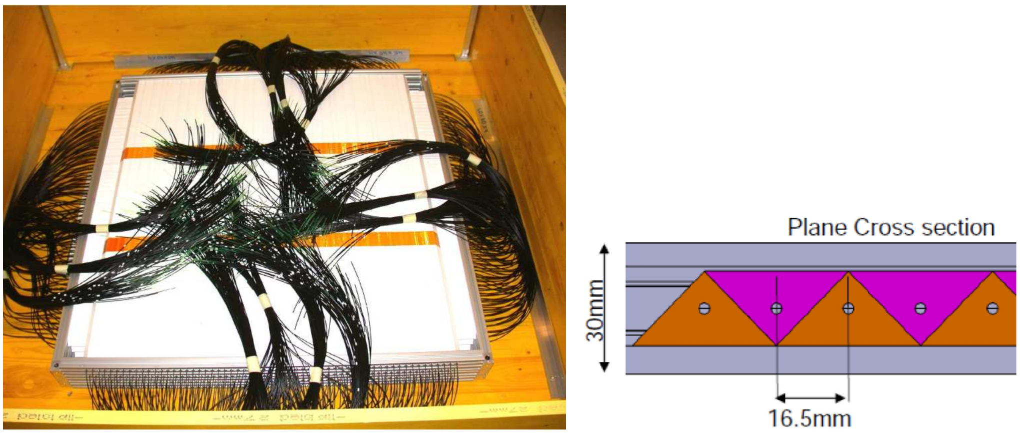

(a) (b)

Figure 3.3: a) The EMR layers organized in the $x-y$ geometry: the clear fibers are covered with a dark plastic to avoid the fiber crosstalk effect; b) the scintillating bars which have a triangular cross-section to reduce the inefficiency in the dead region between the bars themselves.

themselves (figure 3.3(a)).

The scintillation light of each layer bars is readout on both sides, as shown in figure 3.4(a): on one side, the fibers are grouped together and connected to a single anode PMT in order to measure the energy released in the whole plane (figure 3.4(b)) and on the other side the fiber of each bar is connected to a single channel of a 64-channel multi-anode PMT (figure 3.4(c)) allowing to measure the energy loss in each single bar.

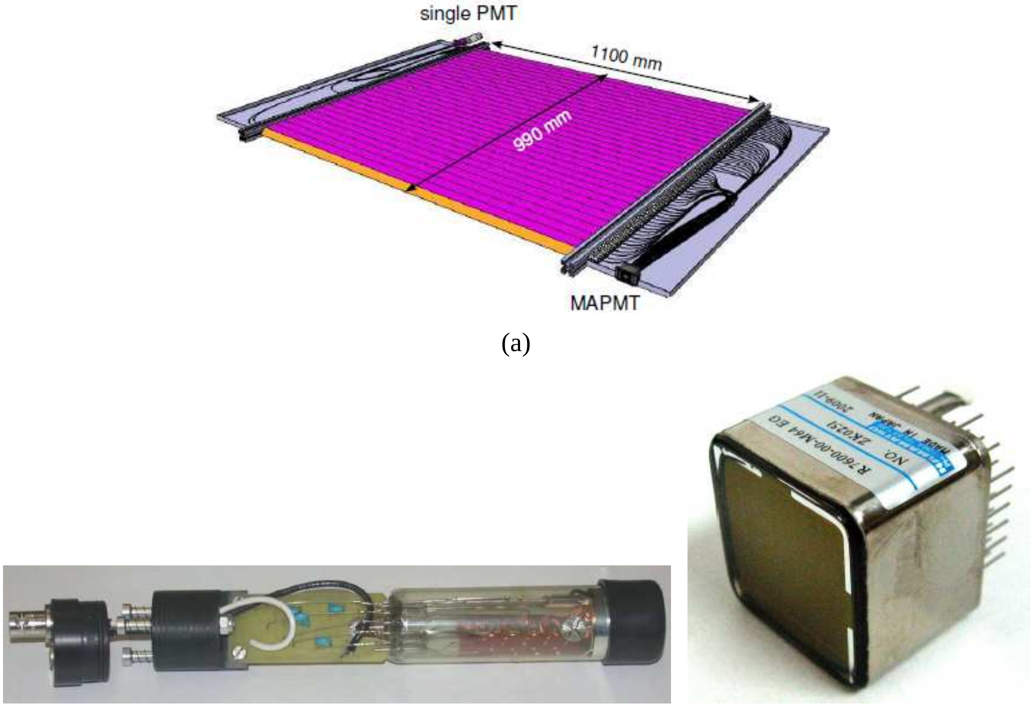

(a)

(b) (c)

Figure 3.4: a) The EMR layers have a double readout: b) on one side the bars are readout by a single anode PMT (for the overall energy measurement) and c) on the other one by a 64-channel MAPMT (for the measurement of the energy deposited in each single bar) [50].

The single-channel PMTs signals are digitized by six 8-channel WaveForm Digitizers (WFD 1731, CAEN[2]) while the MAPMTs ones are processed by the FrontEnd Boards (FEBs) and sampled, buffered in a local memory and sent by the Digitizer and Buffer Boards (DBBs) to a readout board. For a more detailed description of the EMR electronics see [50]. The FrontEnd Board used in the EMR detector is the final version of the one used during the prototypes tests (described in section 3.2.1.4).

[2]CAEN Spa; *www.caen.it*

3.2 The SiPM Readout Test

A new type of scintillating bars detector readout system based on SiPMs interfaced with a MAROC3 board has been tested using cosmic rays. In this section the small EMR prototype (used to perform the tests) is described together with the setup, the readout electronics and the DAQ features. The last part of this section presents the results (mainly in terms of spatial resolution, detection efficiency and timing resolution) obtained during this cosmic ray test.

3.2.1 The Setup

Figure 3.5 presents the experimental setup for the cosmic ray test. It mainly consists of:

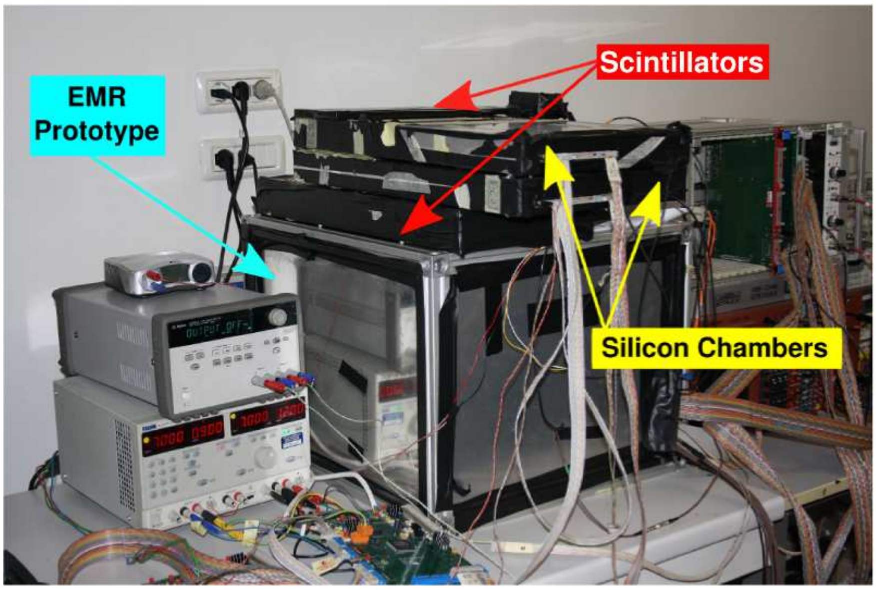

Figure 3.5: The experimental setup for the cosmic ray test, which consists of two plastic scintillators, two Si BCs and the small EMR prototype.

- two plastic scintillators which provide the trigger signal;
- two Silicon Beam Chambers (Si BCs) for the particle track reconstruction;
- the small scale EMR prototype.

3.2.1.1 The Plastic Scintillators

The two plastic scintillators used in coincidence to provide the trigger signal are:

- a $10\times20\times1$ cm^3 scintillator placed above the BCs: it is made of polystyrene (figure 3.6(a)) and readout by a 931B Hamamatsu PMT;

(a)

(b)

Figure 3.6: The two scintillators for the trigger generation.

- a $20\times30\times1$ cm^3 NE120 (Nuclear Enterprises) scintillator, which during this test was placed below the Silicon beam chambers. It is readout by a P30CW5 photomultiplier (Electron Tubes[3]) directly coupled to the scintillator [73] and, as shown in figure 3.6(b), the module is hosted in a PVC box.

3.2.1.2 The Silicon Beam Chambers

The Silicon Beam Chambers represent the tracking system of the setup: they are a pair of large area Silicon detectors developed for the AGILE satellite [74]. Each chamber consists of two 9.5×9.5 cm^2 410 μm thick single side Silicon microstrip detectors arranged in a $x-y$ geometry and glued on an epoxy fiberglass support, as shown in figure 3.7(a). The physical pitch is 121 μm, but the readout one is 242 μm because a floating strip readout is adopted: a spatial resolution of 30 μm has been obtained in this way [74].

The two Silicon tiles are housed in an aluminum box (figure 3.7(b)) together with a part of the frontend electronics: a printed-circuit board (PCB) for the three readout ASICs (which are 128-channel self-triggering TA1 ASICs, Gamma Medica - IDEAS[4]) and a repeater board which generates the bias voltages both for

[3] Now Sens-Tech Ltd.; *www.senstech.com*
[4] Gamma Medica - IDEAS; *http://www.gm-ideas,com*

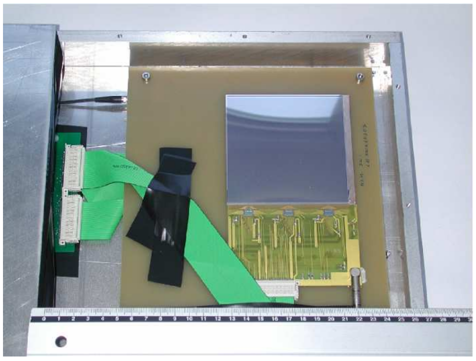

(a)

(b)

Figure 3.7: The Silicon beam chamber: a) one of the Silicon tiles with its frontend electronics and b) the aluminum box which houses the tracking system and a part of the readout electronics [74].

the ASICs and the Silicon detectors (typically ∼54 V), transforms the digital inputs from a standard RS422 to single ended and amplifies the multiplexed analog output with a NE592 [74].

3.2.1.3 The Small Scale EMR Prototype

Figure 3.8 presents the small scale EMR prototype (initially assembled to study the tracking performance of the EMR detector [50]) which consists of 8 layers, arranged in two blocks (separated by a 3 cm air gap) and organized in a $x - y$ configuration. Each layer is composed of 10 19.1 cm long extruded scintillating

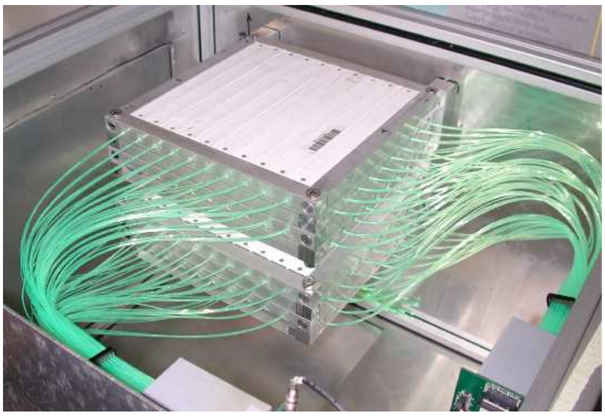

Figure 3.8: a) A photo of the small scale EMR prototype: it consists of 8 layers arranged in a $x - y$ geometry readout by two MAPMTs.

bars with a rectangular cross-section of 1.9 cm×1.5 cm.

The light produced by a particle in the scintillator is carried out by four 0.8 mm diameter WLS fibers to two R7600-00-M64 Hamamatsu 64 channel MAPMTs (whose main properties are summarized in table 3.1): the four x layers are read-

Spectral Response	300-650 nm
Wavelength Peak	420 nm
Quantum Efficiency at 390 nm	21%
Photocathode Material	Bialkali
Photocathode Effective Area	18.1×18.1 mm^2
Anode Size	2×2 mm^2
Window Material	Borosilicate glass
Maximum Supply Voltage	-1000 V
Gain	3.0×10^5
Crosstalk	2%

Table 3.1: Main features of the R7600-00-M64 Hamamatsu 64 channel photomultiplier.

out by one MAPMT, while the layers along the y direction are readout by a second MAPMT, as shown in figure 3.8. For the cosmic ray test, this readout configuration has been modified: as shown in figure 3.9(a), 8 bars of the first layer are equipped with a double readout system. In other words, these bars are readout on one side by a MAPMT biased with a voltage of 850 V and on the other side by 8 circular SiPMs manufactured by FBK-irst (figure 3.9(b)), which have been biased at 38 V. Table 3.2 presents the main features of the FBK-irst SiPMs used in this test.

Diameter	1 mm
Number of Pixels	688
Pixel Area	40×40 μm^2
Breakdown Voltage	31 V
Gain	$\sim10^6$
QE (at 380-530 nm)	90%
PDE	$\sim$40%
Fill Factor	44%

Table 3.2: The main features of the FBK-irst SiPM used as a readout system in the small scale EMR prototype.

The interface between the fibers coming out from the bars and the readout sys-

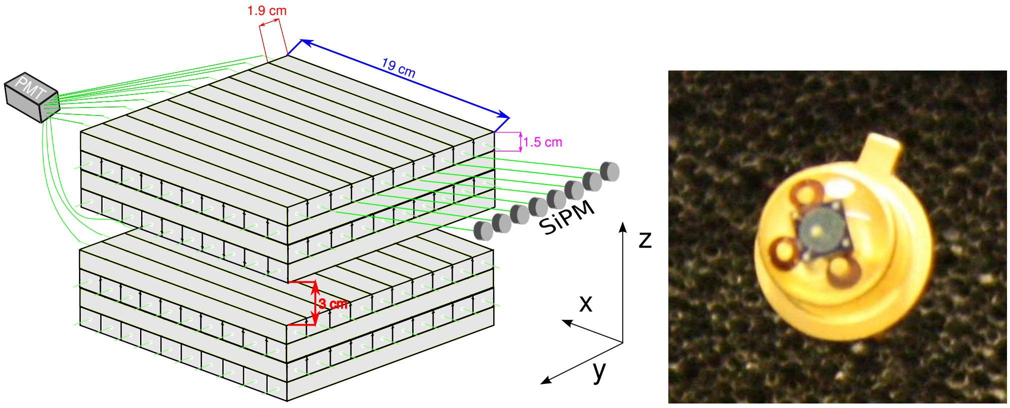

(a) (b)

Figure 3.9: a) The schematic view of the double readout system of the small scale EMR detector first layer: it has been equipped with a double readout system based on a MAPMT and 8 SiPMs. b) A photo of the FBK-irst SiPM.

tems is provided by two different coupling plastic masks shown in figure 3.10(a) and 3.10(b): in both cases the mask is divided in two parts, one that holds the

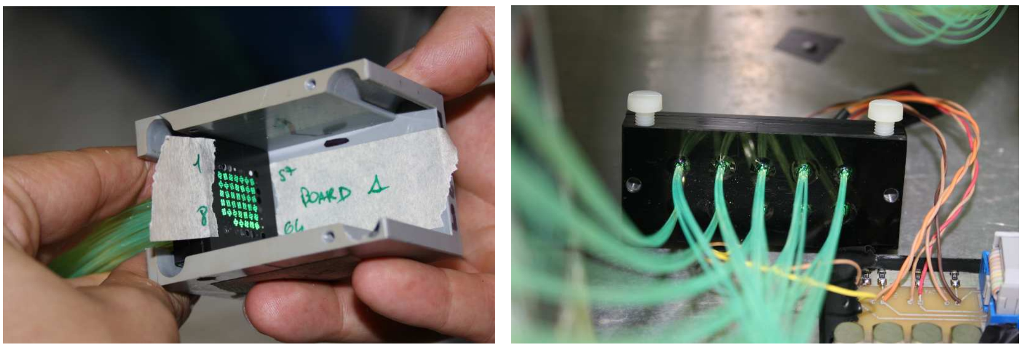

(a) (b)

Figure 3.10: The coupling mask for the readout system of the small EMR prototype based on a) the MAPMT and b) the SiPMs.

device in position and the other where the fibers are glued with an optical glue.

3.2.1.4 The MAROC Board

Both the MAPMT and the SiPMs signals are processed by a prototype of the EMR detector FrontEnd Board (figure 3.11), whose main elements are:

- the 64-channel Multi Anode Read-Out Chip 3 (MAROC3) ASIC, which represents the heart of the board. The ASIC is able to process 64 channels

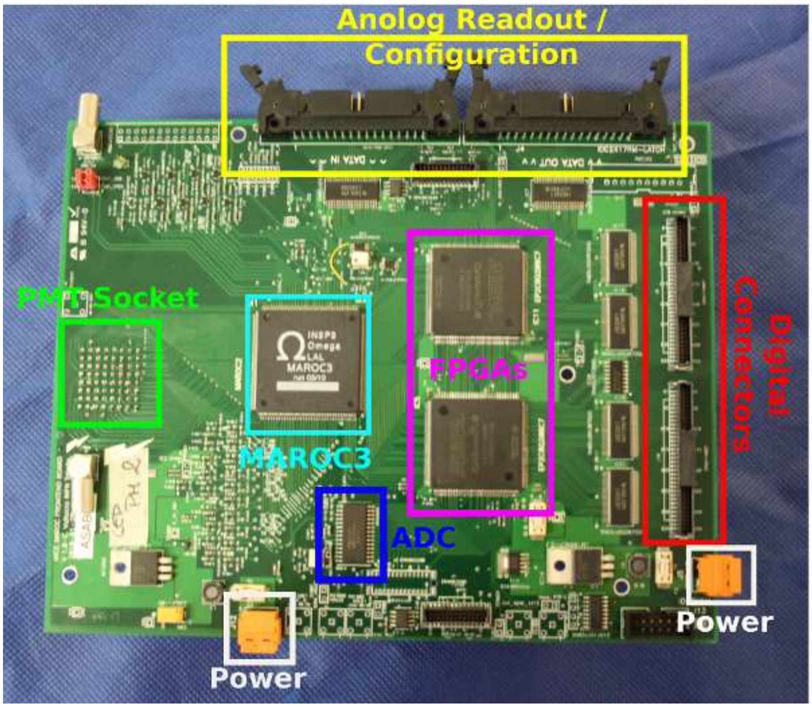

Figure 3.11: The EMR FEB prototype used for the tests with cosmic rays.

in parallel: each MAROC3 channel consists of a pre-amplifier with a variable gain (which for this test has been set to 64, i.e. the unitary gain, both for the MAPMT and the SiPMs), two shapers (a slow one for the analog readout and a fast shaper for the digital output), a sample&hold circuit and a discriminator;

- two Plastic Quad Flat Pack (PQFP) FPGAs (ALTERA Cyclone II[5]), which perform the configuration and the readout of the MAROC ASIC;

- a socket providing the photodetector connection on the FEB: as far as the MAPMT is concerned, it has been connected directly to the socket, while the 8 SiPMs have been connected using 8 ns long LEMO cables;

- the analog and digital connectors.

A more detailed description of the MAROC3 board and the results of the bench tests are presented in appendix A.

[5]Altera Corporation; *www.altera.com*

3.2.1.5 The DAQ System

Figure 3.12 presents a schematic view of the Data AcQuisition (DAQ) chain. It is based on a standard VME system controlled by a SBS Bit3 model 620 board optically connected to a Linux PC. The VME crate hosts the following boards:

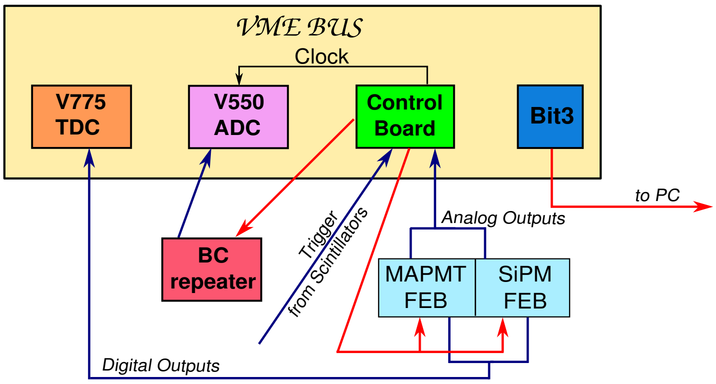

Figure 3.12: The DAQ scheme of the small scale EMR prototype cosmic ray test: the red lines represent the output signals from the control board, while the blue ones are the outputs from the detectors.

- a VME I/O control board which receives the trigger signal (generated by the coincidence of the two scintillators) and provides the start signal to the the beam chambers readout system. The control board is responsible also of the configuration and the readout of the analog outputs of the two MAROC3 boards;

- a CAEN 10 bit V550 ADC (Analog to Digital Converter) to convert the analog signals of the BCs. This ADC can work in zero-suppression mode, so that only the beam chambers strips above a threshold value are readout: each channel signal is compared to a threshold and only if the signal is above this threshold the value is stored. The threshold is set considering the noise of the channel as computed in the pedestal run. Since less than 5 strips are typically above the threshold and the time needed to transfer the data from the VME to the PC is around 2-3 μs per channel, the zero-suppression reduces dramatically the readout time. This feature has been used only during the tests with particle beams at CERN;

- a CAEN 12 bit V775 TDC (Time to Digital Converter) to sample the digital outputs of the MAROC boards to obtain the timing information.

The DAQ software is written in C while Tcl/Tk[6] [75] is used for the graphical interface. The raw data are stored in binary files (PAW ntuples) which have been processed off-line to obtain ASCII DST (Data Summary Tape) files.

The data used for this analysis were pre-analyzed during the off-line processing. When a particle crosses the silicon detector of a chamber, it deposits an energy which may be detected by several neighboring strips that form the so called cluster. To decide if a strip belongs to a cluster, a threshold is set in terms of the noise RMS. The distribution of the signal to noise ratio (the so called $pull$ distribution) has been computed for the strip with the maximum signal in the event. A typical value of the threshold is 15, that is the signal detected by the strip has to be larger than $15 \times noise\ RMS$. Two clusters are considered separated if there is a gap of at least two below-threshold strips among them. In the analysis described in the next section (performed with ROOT), only the one cluster events (in all the BCs) have been selected and written in the DST files.

In the off-line processing the pedestal, defined as the baseline of each ASIC channel when no signal is present, has to be subtracted from the raw data. The pedestal has been evaluated acquiring a run of 200 events with a random trigger. Figure 3.13(a) presents an example of the pedestal profile for the SiPM board of

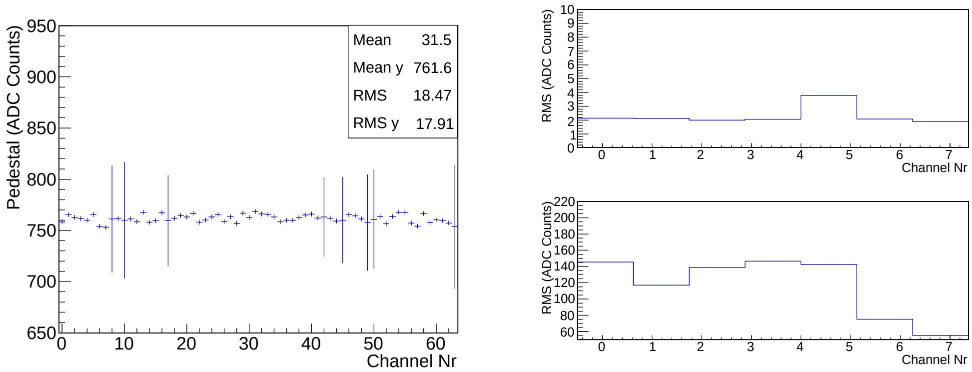

(a) (b)

Figure 3.13: a) An example of the pedestal profile of the SiPM channels and b) the noise RMS for the eight bars readout both by the MAPMT (top) and the SiPMs (bottom): the values are much larger in the SiPM case.

the small scale EMR prototype: the mean value of the SiPM baseline is 760 ADC and the 8 channels connected to the SiPMs are clearly visible.

The noise RMS of the 8 bars with the double readout is plotted as a function of the channel number in figure 3.13(b). It is possible to note that the values of

[6]Tcl (Tool Command Language) is a dynamic programming language and Tk is its graphical user interface toolkit.

the MAPMT noise RMS are smaller than 2 ADC, while the mean of the SiPMs RMS is of the order of 100 ADC. This result has to take into account the different gain of the two readout systems: figure 3.14 shows the pulse heights of a selected bar when this is the one with the maximum signal in the event for the MAPMT and the SiPM. The distributions have been fitted with the convolution of a Landau

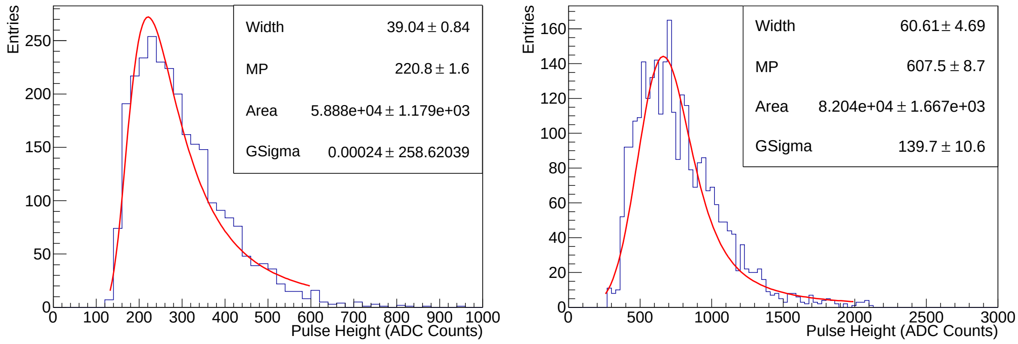

(a) (b)

Figure 3.14: The pulse height distributions for a) a MAPMT bar and b) a SiPM one computed requiring that the bar is the one with the maximum signal. A fit with a Landau convoluted with a gaussian has been performed.

and a gaussian function[7] in order to extract the most probable value, which in the MAPMT case (220 ADC) is smaller than in the SiPM one (608 ADC) of a factor 3. Even taking into account this factor, the SiPM is much more noisier than the MAPMT (a factor 25-30).

3.2.2 The Analysis Results

The main goal of the data analysis is the evaluation of the performance of the SiPM based readout system, which is presented in terms of spatial resolution, detection efficiency and timing resolution.

The analysis procedure consists of the following steps:

- the evaluation of the signal to noise ratio;
- the cluster identification in order to reconstruct the particle hit on the prototype layer;
- the evaluation of the spatial resolution, that is the precision with which the detector is able to reconstruct the hit position;

[7]CERN-Root package reference: *http://root.cern.ch/root/html/tutorials/fit/langaus.C.html*

- the evaluation of the detection efficiency;
- the evaluation of the timing resolution.

3.2.2.1 The Signal to Noise Ratio

Figure 3.15 presents the beam profile in both the x and y directions obtained with one of the Silicon beam chambers: as expected the incident cosmic rays cover the whole active area of the detector.

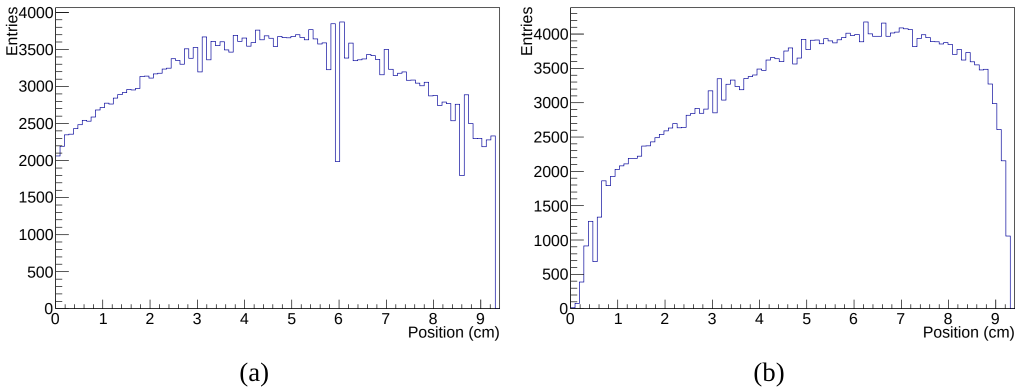

Figure 3.15: The cosmic rays profile in a) the x direction and b) in the y one as reconstructed by one of the Silicon beam chambers.

The first step of the analysis consists in the evaluation of the Signal to Noise Ratio performed considering the pull distribution: the pull is defined as the ratio between the pulse height of the bar with the maximum signal in the event and its noise RMS (obtained from the pedestal analysis and written in the DST file). Figure 3.16(a) presents the pull distribution for the 8 MAPMT bars, while figure 3.16(b) the one of the 8 SiPM bars. The MAPMT pull is much larger than the SiPMs one and a mean value of 109.33 in the MAPMT case and 6.85 in the SiPMs one has been obtained fitting the distributions with a Landau + gaussian function.

The pull distributions allow to set a threshold to distinguish the noise events from the signal ones, which is 45 for the MAPMT case and 5 for the SiPMs.

3.2.2.2 The Spatial Resolution

Even if only the BCs one-cluster events are selected, it can happen that different particles hit the prototype but not the trigger and the tracking system: in order to avoid taking into account these events and to select only the one-cluster events in

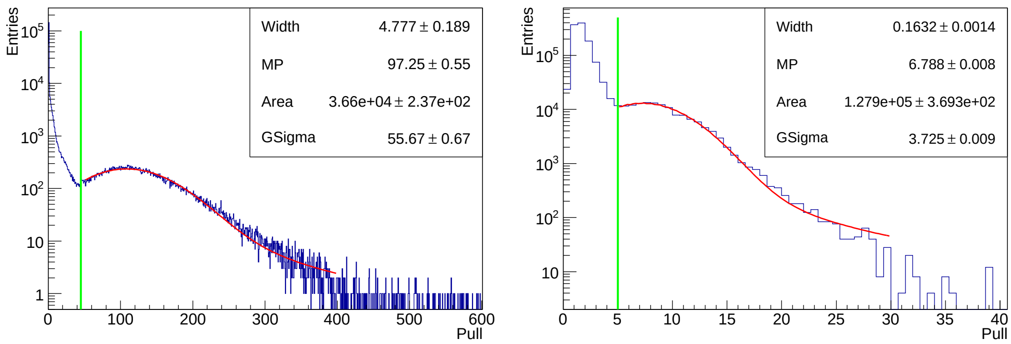

Figure 3.16: The pull distribution of a) the MAPMT and b) the SiPM bars. The green lines represent the threshold to distinguish the noise from the signal events.

the prototype, a cluster identification algorithm has been used to find the particle hit position measured by the prototype layer.

As mentioned before, a cluster is defined as a group of contiguous bars with a signal larger than a given threshold (defined in section 3.2.2.1). The cluster identification algorithm consists of the following steps:

- the pulse height of the 8 bars has been compared with the threshold;
- if the signal is larger than the threshold, the bar has been considered as one which forms the cluster and its number has been identified: in this case the first cluster is identified and a counter is increased of one;
- the bar number difference between each couple of hit bars is computed in order to identify the number of clusters and the number of bars composing each cluster. If the difference is larger than 1, the two bars belong to two different clusters: the cluster counter is increased of one. If the difference is smaller (or equal) than 1 the two bars belong to the same cluster and another counter, defined as the number of bars per cluster, is increased of one;
- the hit position, or, in other words, the position of each cluster, has been obtained as the center of gravity of the deposited charge:

$$position_{measured} = \frac{\sum PH_i * n_{bar} * pitch}{\sum PH_i} \tag{3.1}$$

where i is the index of the number of the bars composing the cluster, PH_i is the pulse height of each cluster bar, n_{bar} is the bar number in the plane and $pitch$ is the bar pitch (1.9 cm).

The cluster identification has been performed independently for the MAPMT and the SiPM readout system. The distributions of the number of clusters are presented in figure 3.17, while figure 3.18 shows the distributions of the number of bars per cluster. In most of the events there is only one cluster: both for the spatial resolution and the efficiency evaluation, only the events with a single cluster have been selected. Also the number of bars per cluster is one in most of the events: larger numbers are due to the particles which are not perpendicular to the prototype layer.

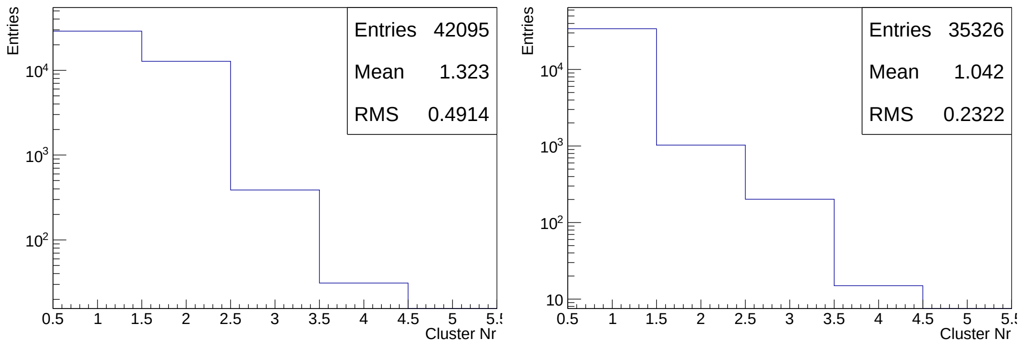

(a) (b)

Figure 3.17: The distributions of the number of clusters for a) the MAPMT and b) the SiPM readout system: most of the events are one-cluster.

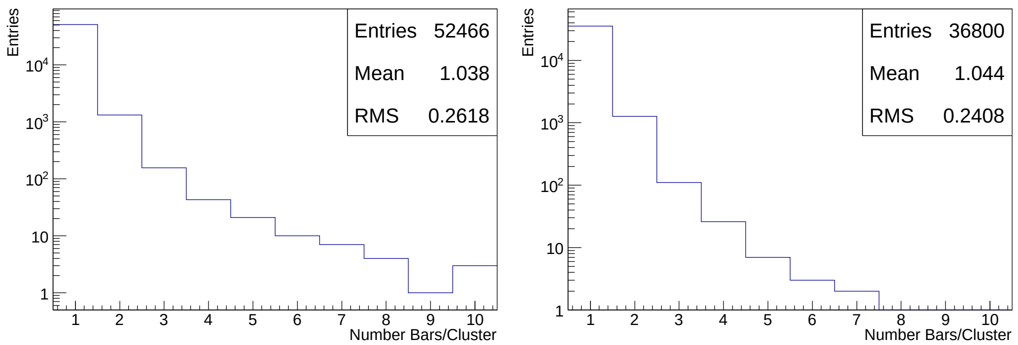

(a) (b)

Figure 3.18: The distributions of the number of bars per cluster for a) the MAPMT and b) the SiPM readout system: it is one in most of the events.

The spatial resolution has been computed using the residual method. The following procedure has been applied:

- the one-cluster events have been selected;

- the particle tracks have been reconstructed with the silicon detectors and projected on the surface of the layer prototype, as shown in figure 3.19.

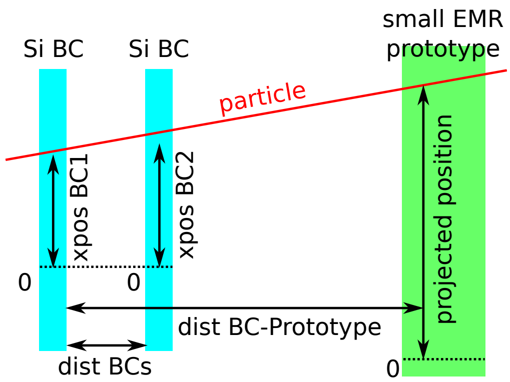

Figure 3.19: The residual method principle: the residual is defined as the difference between the hit position projected by the silicon detectors on the prototype surface (equation 3.2) and the one measured by the prototype itself (equation 3.1).

The expected position of the cluster is found with the following relation:

$$position_{projected} = \frac{xpos_{BC1} - xpos_{BC2}}{dist_{BCs}} \cdot dist_{BC-Proto} + xpos_{BC1} \quad (3.2)$$

where $xpos_{BC1}$ and $xpos_{BC2}$ are the hit positions in the first and second beam chamber, while $dist_{BCs}$ is the distance between the two silicon detectors and $dist_{BC-Proto}$ the distance between the first beam chamber and the small EMR prototype layer;

- the residual has been evaluated as:

$$residual = position_{projected} - position_{measured} \quad (3.3)$$

where $position_{measured}$ is the cluster position as measured by the prototype itself (equation 3.1);

- the distribution of the residual values has been fitted with a gaussian function and its sigma represents the spatial resolution.

The residual has been minimized considering the distance between the first BC and the prototype as a free parameter. This step is necessary because $dist_{BC-Proto}$ was not known with a very high accuracy. The residual has been evaluated for several distances and the spatial resolution has been plotted as a function of the distance, as shown in figure 3.20. The scan has been fitted with a power-of-2

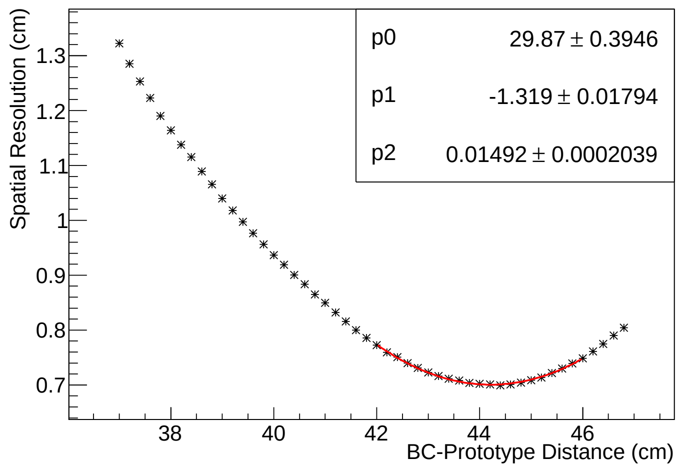

Figure 3.20: The spatial resolution as a function of the distance between the first silicon detector and the prototype, fitted with a power-of-2 function. The minimum corresponds to 44.2 cm.

function: the ratio $-\frac{p1}{2 \cdot p2}$ represents the correct distance (which in this case was equal to ∼44.2 cm), that is the distance minimizing the residual.

Figure 3.21(a) and 3.21(b) present the residual distribution for the readout system based on the MAPMT and the SiPMs. In particular, in the MAPMT case, a second peak due to the crosstalk is clearly visible. As expected, the values are comparable: for the MAPMT σ is equal to 6.9 mm while for the SiPM 6.8 mm.

3.2.2.3 The Efficiency

The efficiency of the detector is defined as:

$$\epsilon = \frac{\text{good events}}{\text{target events}} \tag{3.4}$$

where the "$good\ events$" are the particles detected by the detector, while the "$target\ events$" are the ones theoretically crossing the detector. In particular, only the EMR one-cluster events are tagged as "$target\ events$" (to ensure that the particle crosses the detector), while to identify an event as "$good$" the cluster position measured by the prototype has to be within 3σ from the projected position.

To compute the efficiency a profile histogram has been filled with 0 or 1: if an event is tagged as a "$target\ event$" the profile histogram has been filled with 0, while if the event is tagged also as a "$good\ event$" the profile has been filled with 1. The error on the efficiency is evaluated using the error computation of the

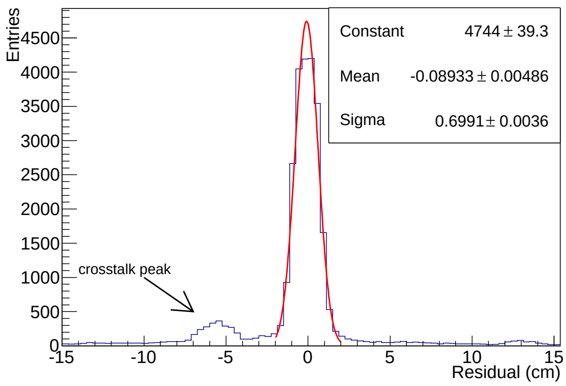

(a)

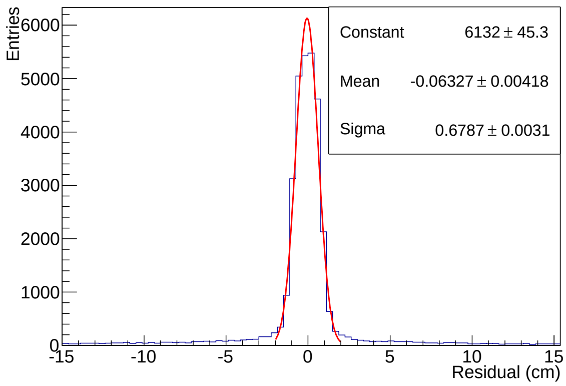

(b)

Figure 3.21: a) The MAPMT and b) SiPM residual distribution fitted with a gaussian function: the σ value represents the spatial resolution.

ROOT TProfile[8]; the error is defined as:

$$\sigma_\epsilon = \frac{\mathrm{RMS}_\epsilon}{\sqrt{\mathrm{N}}} \tag{3.5}$$

where N is the number of entries of a bin of the profile while RMS_ϵ is the spread of the entries of that bin (i.e. the spread of the efficiency values).

Figure 3.22 presents the two dimensional efficiency profiles for the MAPMT and the SiPM. The MAPMT spot in the x direction is larger because all the 10 bars of the layer are connected with the photodetector, while on the SiPM side only the central 8 bars are readout.

In order to extract an efficiency value, the projection along the x direction of these two dimensional profiles has been performed: as shown in figure 3.23

[8]CERN-Root package reference: *http://root.cern.ch/root/html/TProfile.html/TProfile:SetError Option*.

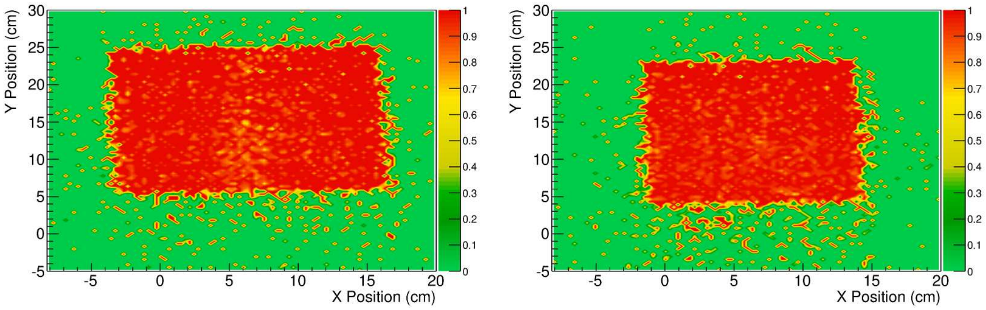

(a) (b)

Figure 3.22: The two-dimensional efficiency profile histograms of the layer readout both by a) the MAPMT and b) the SiPMs.

the plots have been fitted with a constant function, obtaining an efficiency equal

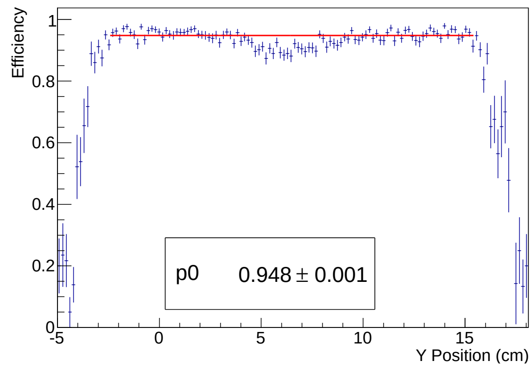

(a)

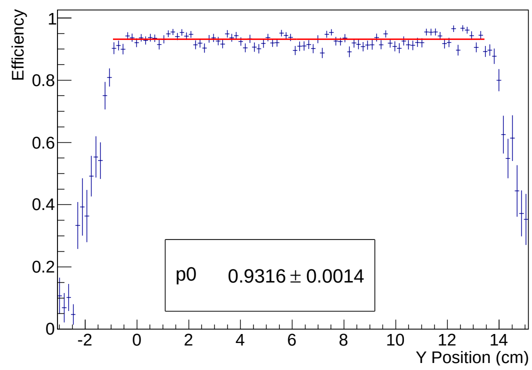

(b)

Figure 3.23: The x projections of the 2D efficiency plots fitted with a constant for a) the MAPMT and b) the SiPMs.

to 94.8±0.1% for the MAPMT (figure 3.23(a), where an efficiency drop in the middle of the layer is visible) and to 93.2±0.1% for the SiPMs (figure 3.23(b)).

3.2.2.4 The Timing Resolution

The time resolution has been computed considering the TDC data, which give the time interval between the scintillators trigger and the MAROC digital outputs (that is the time the analog signal crosses the discriminator threshold) [76]. Figure 3.24 presents an example of the TDC values distributions obtained with a MAPMT bar (figure 3.24(a)) and a SiPM one (figure 3.24(b)): in both cases, a tail in the left part of the distribution due to the timewalk is present. The distributions have been fitted with a gaussian function in order to obtain the timing resolution represented by the $sigma$ parameter of the fit. In particular, for this selected bar the MAPMT

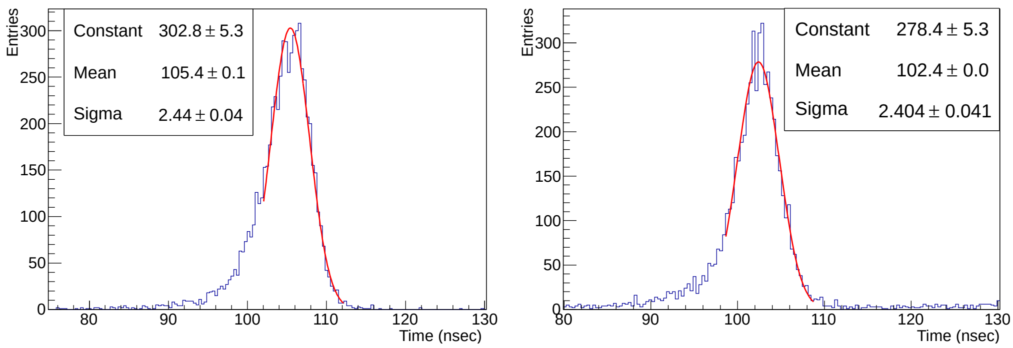

(a) (b)

Figure 3.24: The timing resolution of a) a MAPMT and b) a SiPM bar: the TDC value distribution has been fitted with a gaussian function and its $sigma$ parameter corresponds to the timing resolution.

timing resolution is equal to 2.44 ns while the SiPM one is 2.40 ns. This analysis has been performed for all the 8 bars with the double readout system obtaining an average value of 2.54±0.02 ns for the MAPMT and of 2.56±0.02 ns for the SiPMs.

The two results are comparable and they have to be considered an upper limit: in fact, they are the sum of different effects such as the intrinsic timing resolution of the photodetector, the characteristic timing of the scintillator and the WLS fibers light emission and the timewalk of the electronics chain.

3.2.2.5 The Position Dependence

Using the TDC data, the travel time of the scintillation light in the scintillating bar has been computed. Since the bars are made of Polystyrene, which has a refractive index of n=1.60, the light speed in the bar should be 18.7 cm/ns: thus, the light should need $\sim$1 ns to cross the 19 cm long bar.

Considering the BCs information, just the events in which the particle hits a small area on the two opposite bar ends have been selected: the selected regions are $\sim$1 cm wide. The distributions of the TDC values have been computed separately for the signals coming from the SiPM side (the blue histogram in figure 3.25(a)) and for the ones coming from the other side (the red histogram). The

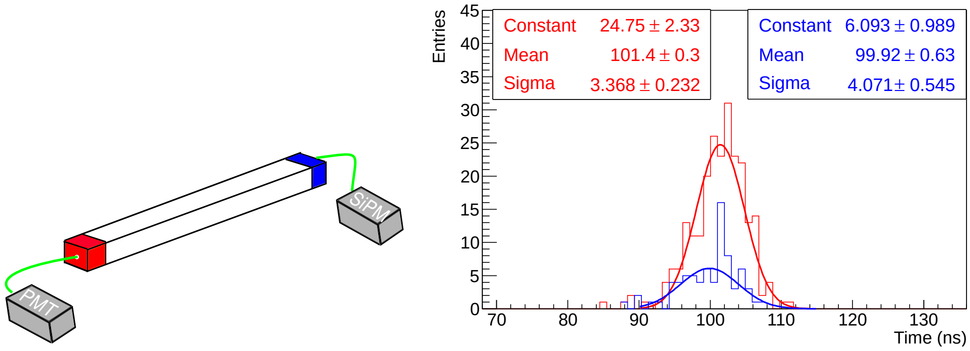

(a) (b)

Figure 3.25: Measurement of the light travel time through the 19 cm long bar: a) a schematic view of the event selection; b) the TDC histograms for the two sides of the bar.

two histograms have been fitted with a gaussian function and the two peaks are in fact separated by 1 ns: in other words, since the light produced in the region opposite to the SiPM has to cross the whole bar length, its signal is delayed of $\sim$1 ns with respect to the one coming from the SiPM side. This analysis is possible thanks to the intrinsic timing resolution of the SiPM (smaller than 1 ns, as described in section 1.3.6.6), while it cannot be performed considering the MAPMT signals: its timing resolution is not good enough to identify the timing separation between the two peaks.

Given the tracking capability of the setup, it has also been possible to study the pulse height of the signal as a function of the hit position on the bar: in principle, the pulse height should not depend on the incident position because the scintillator is homogeneous. The analysis procedure is similar to the one described before:

- a bar has been selected and its length divided into 10 different regions, as shown in figure 3.26(a);
- the particle hit position has been reconstructed by the BCs;

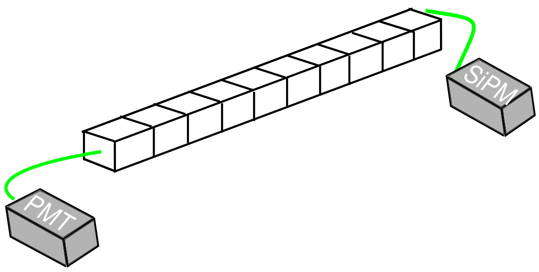

(a)

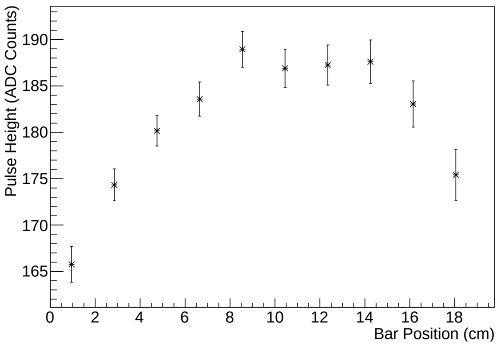

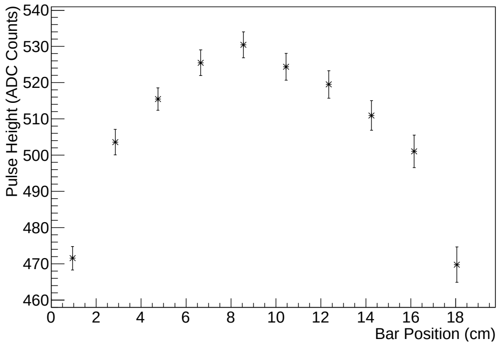

(b) (c)

Figure 3.26: Study of the pulse height dependence on the hit position: a) a scheme of the event selection method; the mean value of the pulse height gaussian fit as a function of the position in the bar for the b) MAPMT and c) the SiPM readout system.

- selecting just the events in each of these areas, the pulse height distribution has been computed and fitted with a gaussian;
- the $mean$ value of each fit has been plotted as a function of the incident position.

The resulting plot is quite similar for both the MAPMT (figure 3.26(b)) and the SiPM (figure 3.26(c)) case: the trend of the pulse height is not constant for the whole bar length. In particular, in the regions corresponding to the ends of the bar a signal attenuation is clearly visible and it is probably due to a loss of light in the holes for the fibers insertion (which are not painted with the reflective material).

Chapter 4

The Large EMR Prototype: Assembly and Commissioning

The Large EMR Prototype (LEP) is a totally active scintillating bars detector made of 48 layers of 4 scintillating plastic bars: the light is carried out by two WLS fibers (inserted and glued in the hole bar) and readout by a double system based on MAPMTs (on one side) and SiPMs (on the other side). The detector has been developed to test the EMR performance as a calorimeter; for this thesis work it has been used to evaluate the performance of a large number ($\sim$200) of SiPMs and compare their behavior to the MAPMTs one.

This chapter presents the Large EMR Prototype and its commissioning with cosmic rays. In the first part a detailed overview of the detector is given together with its assembly procedure and its electronics.

The second part of the chapter introduces the experimental setup and the analysis results of the preliminary tests performed with cosmic rays, whose main goals were the choice of the MAROC ASIC parameters that optimize the SiPMs performance and the evaluation of the system overall stability.

4.1 The Prototype

The Large EMR Prototype (figure 4.1) consists of 48 planes of scintillating bars in a single orientation (the x direction). The detector is organized in three blocks of 16 layers each with a 1 cm air gap between the blocks themselves. Each layer is made of 4 19 cm long extruded bars with a rectangular cross-section of 1.5×1.9 cm^2, as the small scale EMR prototype.

The light produced in each bar is carried out by two 0.8 mm diameter Wave-Length Shifter fibers (Y11(200)MSJ, KURARAY) which have been glued in the bar hole; the assembly and gluing procedure is the following:

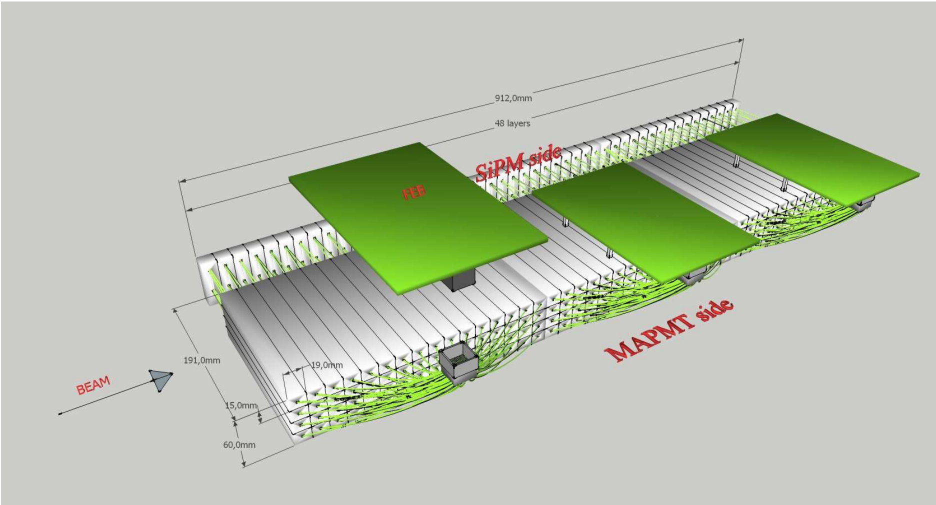

Figure 4.1: Schematic drawing of the Large EMR Prototype: the detector consists of 48 layers of 4 extruded scintillating bars readout on both sides either by MAPMTs or SiPMs.

- the fibers have been cut with a length of about 70 cm;
- a hole has been drilled on both ends of the top face of the bar;
- the two fibers have been inserted in the extruded bar hole and blocked at the ends with silicone glue;
- two syringes, one full of glue (the E-30 epoxy resin from Prochima) and the other empty, have been inserted in the bar holes;
- using the filled syringe, the glue has been pushed in the central extrusion of the bar until it came out in the empty syringe (figure 4.2). During the gluing procedure, particular attention was paid not to leave air inside the bar hole;
- the glued bars have been dried for one night and then the syringes have been extracted from the holes.

On one side the fibers have been interfaced with three R7600-00-M64 Hamamatsu 64 channel MAPMTs (the same of the small scale EMR prototype, and whose main properties are presented in table 3.1), while on the other side with 192 SiPMs with a diameter of 2.8 mm (described in detail in section 4.1.1).

Two different mask systems have been developed to align both MAPMTs and SiPMs with the fibers. In the first case, the fibers of 64 bars (corresponding to one scintillating block) have been glued in a plastic mask which allowed a direct

Figure 4.2: The WLS fiber gluing procedure.

connection between the fibers and the MAPMT (placed in a plastic holder), as shown in figure 4.3(a). Once glued, the fibers have been cut and polished. As far

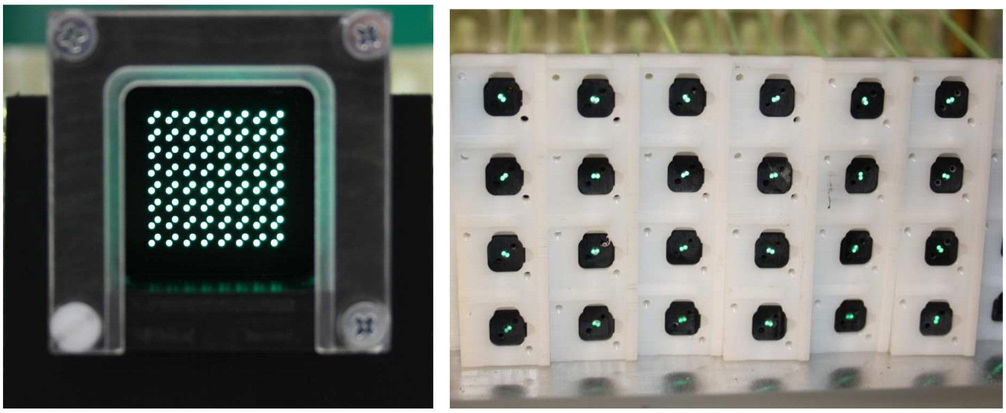

Figure 4.3: The alignment system (plastic masks) for a) the MAPMTs and b) the SiPMs.

as the SiPMs are concerned, the fibers coming out from the 4 bars of each layer have been glued in a teflon holder, cut and polished. On the other side of the holder two holes were drilled to position the PCBs with the SiPMs (figure 4.3(b)).

4.1.1 The LEP SiPMs

As in the small scale EMR prototype case (section 3.2.1.3), the SiPMs assembled on the large EMR prototype have been developed by FBK-irst (figure 4.4(a)):

table 4.1 presents their main features.

Diameter	Cell Number	Cell Dimension	Fill Factor	PDE
2.8 mm	2450	$50 \times 50\ \mu\text{m}^2$	50%	20-25%

Table 4.1: The FBK-irst SiPMs features.

As previously mentioned in chapter 1, each SiPM has typically a different breakdown voltage. In order to find the operation voltage, a $I-V$ measurement has been performed for each of the 207 SiPMs (192 for LEP and 15 spare ones). Figure 4.4(b) presents the biasing scheme of the SiPM; the current value has been computed measuring the voltage drop across the 100 kΩ resistor.

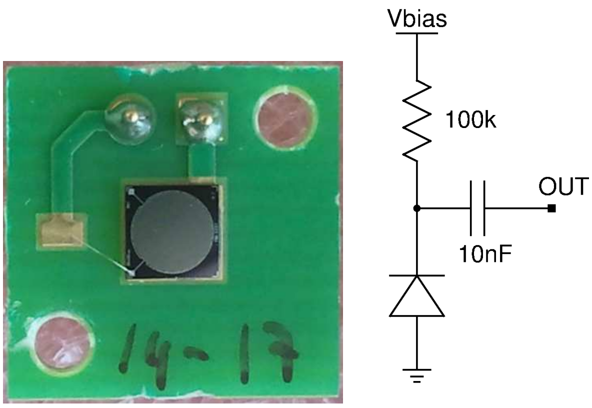

(a) (b)

Figure 4.4: a) A photo of the LEP SiPM and b) the SiPM readout scheme: the current consumption is computed measuring the voltage drop across the 100 kΩ resistor.

An example of a characteristic curve is presented in figure 4.5(a): in this case, the breakdown point is defined as the voltage value corresponding to the current threshold value, set at 0.5 μA and represented in the plot by the dotted violet line. For instance, for the SiPM in the figure the breakdown voltage is 31.1 V.

As stated before a total of 207 SiPMs have been tested and 6 of them were not working: their current consumption was larger than 30 μA for the first step of the voltage scan (equal to 29 V). Figure 4.5(b) presents the working SiPMs voltage for different values of the current: the black points correspond to 0.5 μA (the SiPMs breakdown point) while the red and blue ones to a current of 2μA and 5μA (two possible operation voltages for the data taking).

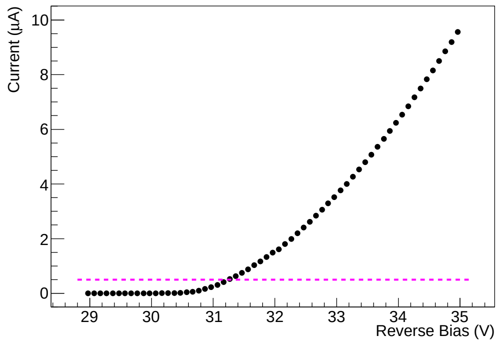

(a)

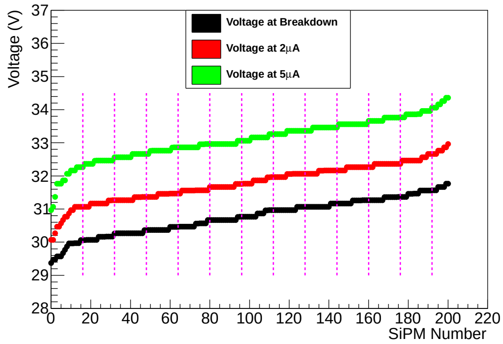

(b)

Figure 4.5: a) The I-V curve to compute the breakdown point (identified as the voltage corresponding to the crossing of the dotted violet line with the curve). b) The 201 working SiPMs voltage for a current of 0.5μA (in black), 2μA (in red) and 5μA (in blue); the SiPMs have been divided into 12 groups.

Starting from these measurements, the 192 SiPMs have been divided in 12 groups (the dotted violet lines in the plot) that have been biased independently using an adapter board.

4.1.2 The LEP Readout Electronics

Both the prototype sides are interfaced with three MAROC3 Boards (described in section 3.2.1.4) to process the signal coming from the photodetectors. All the prototype boards have been tested on bench (before the final assembly) in order to evaluate the ASIC performance: the results of the bench test are presented in appendix A.

While the MAPMTs have been plugged directly on the back of the board, as shown in figure 4.6 which presents the bottom face of the board with the MAPMT in place, the interface between the SiPM PCBs and the board socket is provided by the adapter board (figure 4.7(a)). These adapter boards have been used also to provide the different biases to the SiPMs groups. Figure 4.7(b) presents a photo of the prototype with all the six MAROC3 boards assembled.

4.2 The Cosmic Ray Test

The first Large EMR Prototype test has been performed at the INSULAB laboratory with cosmic rays in order to make a preliminary study of the MAROC ASIC parameters setting and the detector performance. In the next sections the experimental setup and the DAQ system are described and the results in terms of spatial

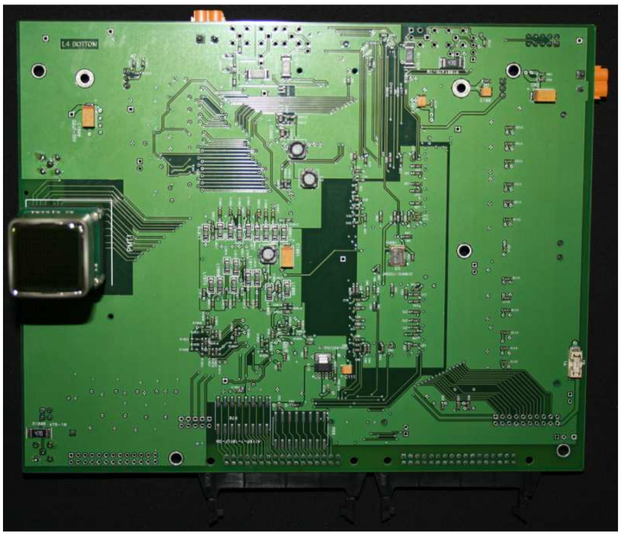

Figure 4.6: The bottom face of the FrontEnd Board with the MAPMT plugged on the board itself (on the left of the board).

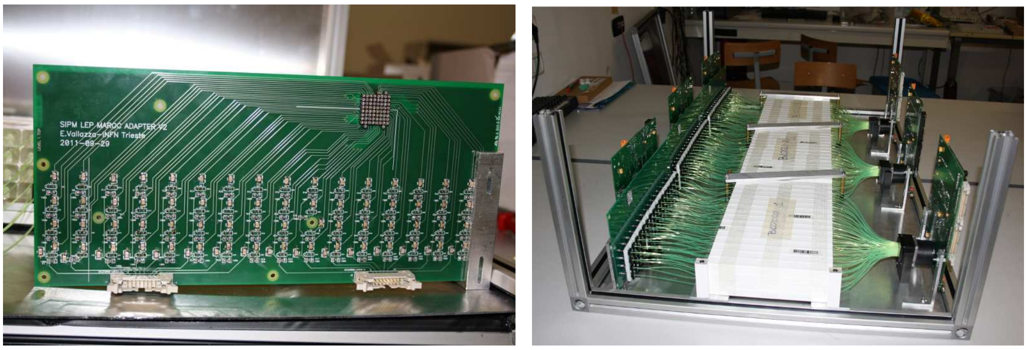

(a) (b)

Figure 4.7: a) The adapter board used to connect the MAROC3 board to the SiPMs. b) The prototype with the six MAROC3 boards in place.

resolution and detection efficiency are presented.

4.2.1 The Setup and the DAQ

Figure 4.8 presents the experimental setup of the cosmic ray test and the DAQ system (which is quite similar to the one used for the small scale EMR prototype test, described in section 3.2.1.5).

The setup consists of:

- a 10×10 cm^2 1 cm thick plastic scintillator (figure 4.9) made of Polystyrene:

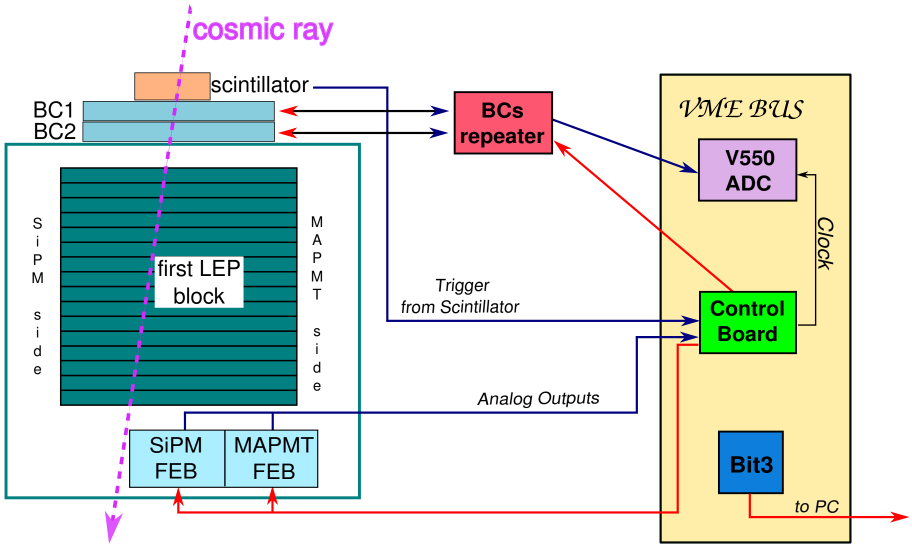

Figure 4.8: A schematic view of the experimental setup and the DAQ system of the cosmic ray LEP test. The setup consists of a plastic scintillator, which provides the trigger signal, a couple of BCs and the prototype under test; while the DAQ is based on a standard VME system.

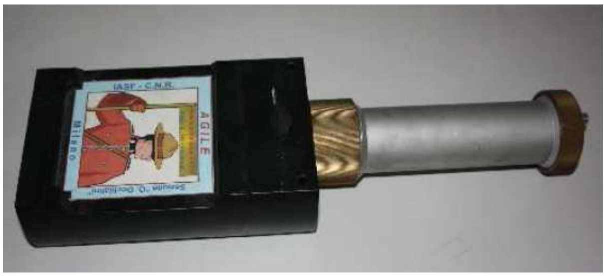

Figure 4.9: A photo of the scintillator for the trigger signal in the cosmic ray test of LEP.

the light produced by the incident particle is readout by a photomultiplier tube directly connected to the scintillator tile providing the trigger signal to the VME I/O control board;

- a couple of Silicon Beam Chambers (described in section 3.2.1.2) to reconstruct the particles tracks. The readout start signal is generated by the control board once the trigger has been processed; their analog outputs are converted by the V550 ADCs (see section 3.2.1.5);

- the LEP detector: just the first block (i.e. the first 16 layers) of the prototype has been tested. The MAPMT bias voltage has been set at 750 V, while the

SiPMs one (all the 64 SiPMs have been biased with the same bias) at 34.5 V, corresponding to a bias current of $\sim$8 μA. The two MAROC boards process the signals coming from the different readout systems and are configured and readout by the control board. Although the ASIC provides both an analog and digital response (as described in chapter 3), the data have been acquired only in the analog mode for all the LEP tests;

- a SBS Bit3 620 board which provides the optical connection to a PC.

4.2.2 The Test Procedure and the Results

The main goal of the preliminary test on LEP was to study the performance of the 64 SiPMs under test and compare their behaviour with the MAPMTs one. The test procedure was the same described in chapter 3:

- a pedestal run is acquired with 200 random triggers;
- different cosmic ray runs are acquired changing the MAROC parameters;
- a high statistics cosmic ray run is acquired with the best configuration.

In the off-line processing, only the BCs one cluster events are stored in the DST files.

4.2.2.1 The MAROC Parameters Setting

The MAROC ASIC can be tuned depending on the application: the pre-amplifier and shaper features (gain and peaking time) can be varied to find the best signal to noise configuration. The MAROC configuration is performed loading a string of 829 bits in the ASIC itself (as described in appendix A): depending on the analog signal shape, the readout electronics has to choose a correct value for the hold signal, that is for the time when the signal has to be sampled. The test on the ASIC settings has been performed varying the parameters that determine the shaper signal features (which are set with three capacitors) and the readout hold. The pre-amplifier gain has been fixed to a constant value of 64 (corresponding to the unitary gain).

The slow shaper circuit (figure 4.10(a)) consists of three capacitors called C_0, C_1 and C_2 whose values are 1200 fF, 600 fF and 300 fF: they can be set independently in the on (indicated with 1) or the off (0) mode thus changing the shaping time and the gain (as shown in figure 4.10(b)).

Figure 4.11(a) presents an example of the pulse height distribution of one of the LEP SiPMs used to evaluate the Signal to Noise Ratio for different MAROC parameter configurations: the plot has been computed with all the capacitors in

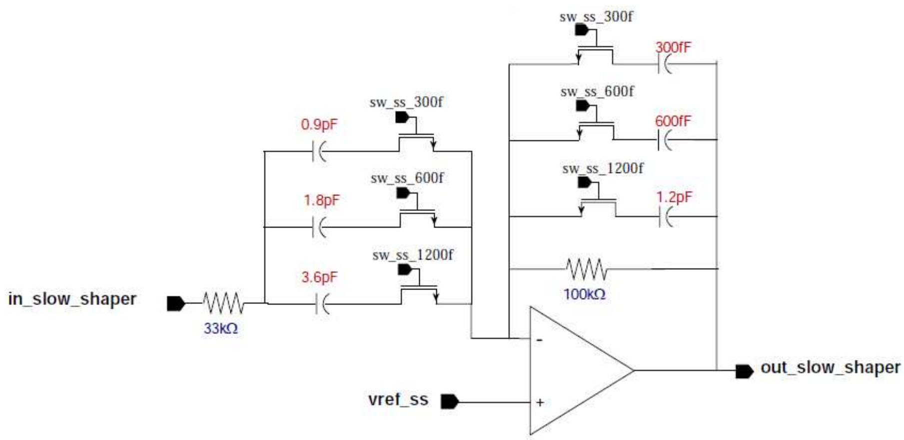

(a)

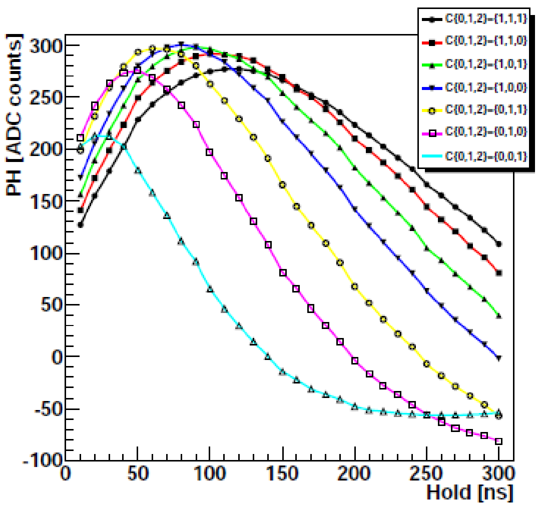

(b)

Figure 4.10: a) The slow shaper circuit with its capacitors (C_0=1200 fF, C_1=600 fF and C_2=300 fF) and b) the hold scan with different shaper settings [50].

the on mode (the so called {1,1,1} configuration) corresponding to the longest possible shaping time and a hold value of 10 ns. The noise peak has been fitted with a gaussian (the red line) while the signal one with the convolution of a Landau and a gaussian function (the green one); the Signal to Noise Ratio has been computed dividing the mean value of the signal fit by the RMS of the noise gaussian distribution. This procedure has been also performed with a faster slow shaper configuration characterized by only the 600 fF capacitor in the on mode (the {0,1,0} configuration) and a hold value equal to 2 ns (the smallest possible value). The obtained SNR values are equal to 5.05 for the slowest tested configuration and 6.67 for the fastest one.

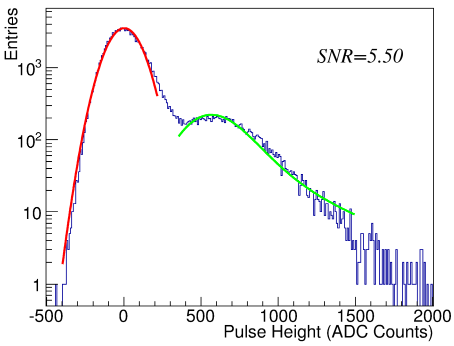

(a)

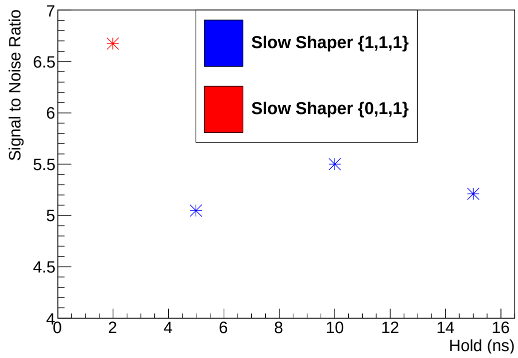

(b)

Figure 4.11: The computation of the SNR for different MAROC parameters settings: a) the pulse height distribution performed with the $\{1,1,1\}$ slow shaper configuration and a hold value of 10 ns with the noise gaussian fit and the signal Landau + gaussian one. b) The SNR as a function of the hold value for the two different slow shaper configurations.

The hold setting has been also tested: the hold is defined as the interval between the trigger signal and the sampling one (for further details see appendix A) and typically its value has to be chosen in order to sample the peak of the slow shaper output signal. This choice allows to optimize the Signal to Noise Ratio (evaluated also in this case considering and fitting the pulse height distribution). The hold test has been computed in the $\{1,1,1\}$ slow shaper configuration with two different hold values (5 ns and 15 ns): the SNR values are respectively 5.21 and 5.04. The hold test value has been performed only in the slow shaper configuration: in the $\{0,1,0\}$ one the hold has been set to the smallest possible value given the time needed by the trigger logic to generate the trigger is already long enough.

Figure 4.11(b) presents the SNR values for all the different parameter settings considered in this test: the $\{0,1,0\}$ configuration (with a hold of 2 ns) is the one chosen for the tests given its better SNR.

4.2.2.2 The Pedestal Analysis

The first step of the analysis is the subtraction of the pedestal value (i.e. the baseline) from the raw data. Figure 4.12 presents the pedestal profile for the LEP boards: the average value for the MAPMT channels is of the order of 630 ADC, while the one of the SiPMs is around 900 ADC.

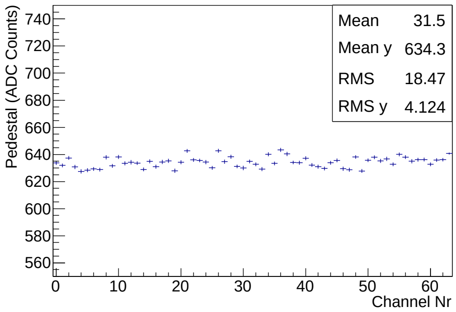

(a)

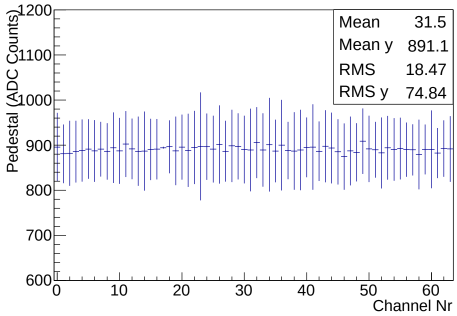

(b)

Figure 4.12: The pedestal profile of the a) MAPMT board and b) the SiPM one.

As far as the noise RMS is concerned (figure 4.13(a)), in the MAPMT case (top) the average value is about 1.5 ADC while in the SiPM case (bottom) it is around 80 ADC: the SiPMs are clearly noisier than the MAPMTs even if they have a factor 10 larger gain.

The noise RMS is the sum in quadrature of the intrinsic noise component and the so called *common mode*, which corresponds to an overall movement of the baseline common to all the ASIC channels due to the noise on the bias line. The common mode noise is computed on an event by event basis; figure 4.13(b) presents the distributions of the common mode values for the MAPMT (top) and the SiPMs (bottom). The common mode value has to be subtracted, event by event, from the raw data and the pedestal and the noise values have to be re-computed. The red lines in figure 4.13(a) represent the noise RMS once the common mode has been subtracted: as far as the SiPM plot is concerned (bottom), it seems that in the SiPM case the common mode is very small. On the other hand, the noise RMS is so large that the evaluation of the CM is masked by this RMS. For this reason, the MAPMTs data written in the DST files are both pedestal and common mode subtracted, while the SiPM data are only pedestal subtracted.

4.2.2.3 The Working and the “Bad” SiPMs

The typical pulse height distribution obtained with a LEP SiPM has been presented in figure 4.11(a): the noise peak, due to the events where no particle has hit the detector or the particle has not been detected, is separated from the signal one.

Figure 4.14(a) presents the pulse height distribution computed with a SiPM which is a working device but not interfaced to the two WLS fibers coming out from the bar. As expected, the distribution is comparable to the pedestal one. On the other hand (figure 4.14(b)), the pulse height distribution of a broken SiPM

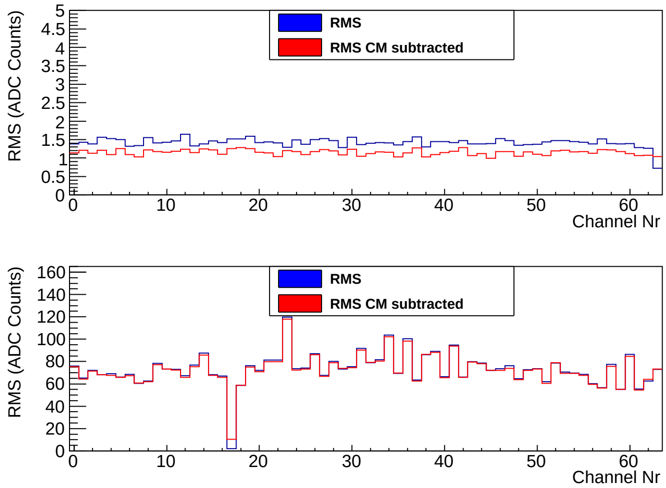

(a)

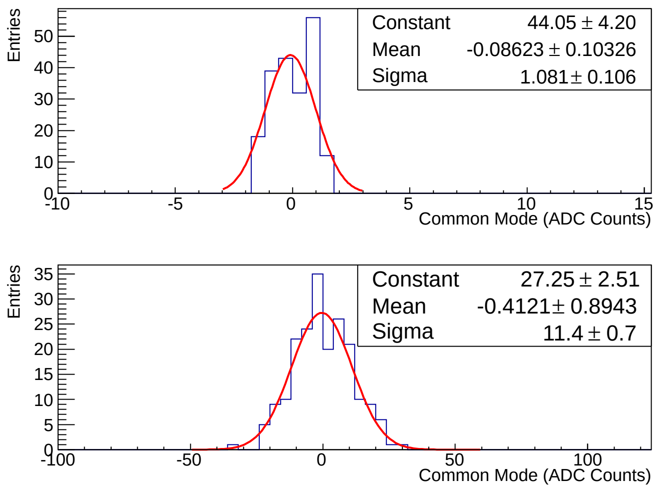

(b)

Figure 4.13: a) The noise RMS (in blue) and the common mode subtracted noise RMS (in red) for each ASIC channel and b) the common mode distributions. The MAPMT board is the one in the top plots while the SiPM one the one in the bottom plots.

(the so called “bad” SiPM) is narrow and peaked on zero (in practice it is the noise RMS of a MAROC channel).

In the LEP first block there are 4 SiPMs not connected to the fibers and just a broken one (over a total of 64 SiPMs); in other words, the percentage of working devices in the first LEP 16 layers is 98%.

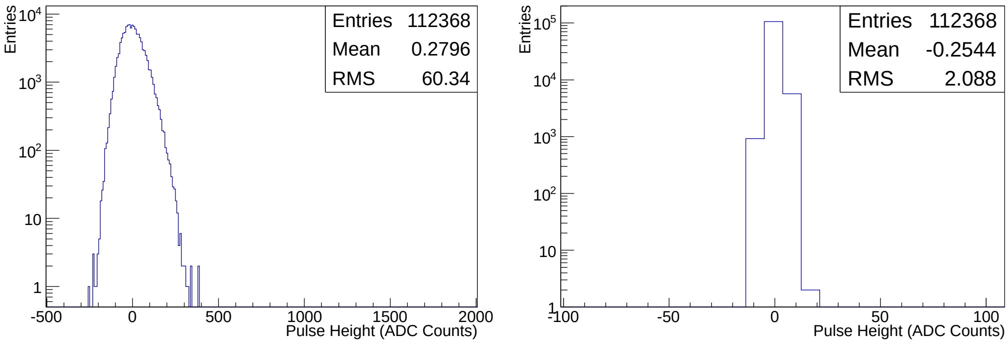

(a) (b)

Figure 4.14: The pulse height distribution of a) a working SiPM not connected to the fibers coming out from the bar and b) a “bad” device. In the first LEP block 4 SiPMs are not connected to the fibers and one is broken.

4.2.2.4 The Pulse Height Equalization

The analog output may vary from bar to bar for several reasons such as the fact that the scintillating light could not reach the MAPMT channel because of the bad gluing of the WLS fibers in the bar hole (thus producing light loss), the not good alignment between the fibers and the photodetectors could introduce crosstalk problems and the intrinsic non uniformity of the MAPMT channels or the different SiPMs in terms of gain.

To set a threshold to distinguish noise from signal events, an equalization is needed:

- the pulse height distribution of each of the 64 bars under test is filled requiring that the bar has the maximum signal in the event for the MAPMT, while in the SiPM case the bar has to be the maximum one and the corresponding MAPMT channel has to be above a given threshold (30 ADC) in order to reduce the noise peak;

- all the distributions have been fitted (excluding the noise peak) with a Landau + gaussian function to extract the most probable value of the distribution (represented by the MP fit parameter, figure 4.15);

- the 64 pulse heights have been re-computed rescaling each peak value to the first bar one;

- the distributions of the rescaled pulse heights have been fitted as a cross-check (figure 4.16).

Once completed this procedure, the pulse height of the bar of each layer with the maximum signal in the event has been considered as shown in figure 4.17 to set

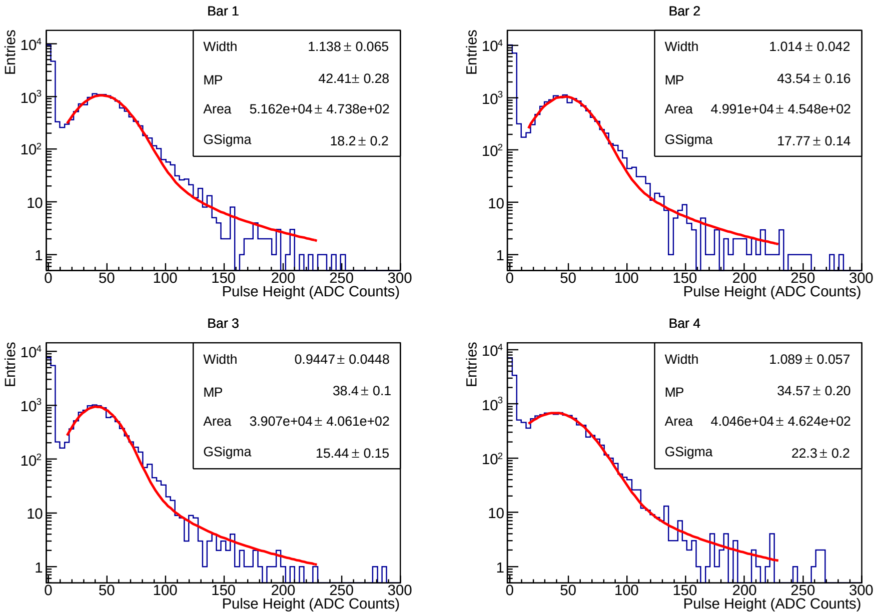

(a)

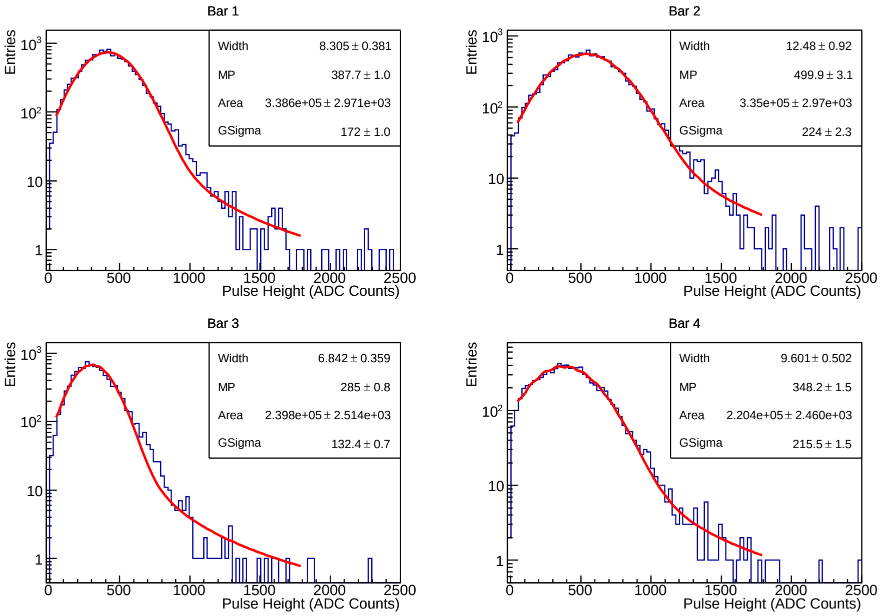

(b)

Figure 4.15: The pulse height distribution of the first LEP layer bars readout by a) the MAPMT and b) the SiPMs. The distributions have been fitted with a Landau + gaussian function to extract the mean value for the signals equalization.

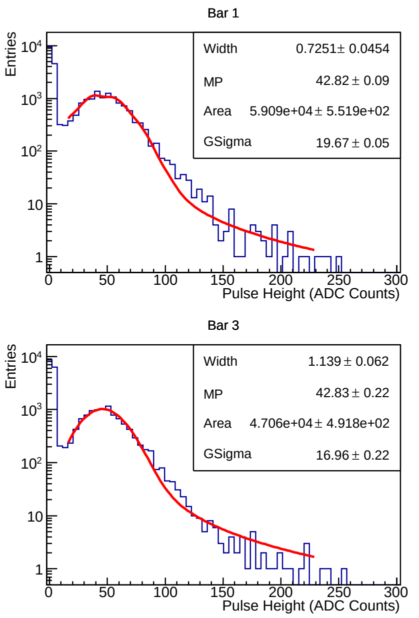

(a)

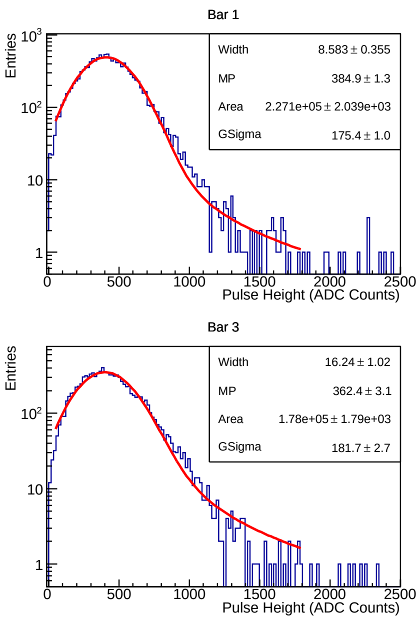

(b)

Figure 4.16: The distributions of the rescaled pulse height for the first four a) MAPMT and b) SiPM bars.

the signal threshold; the final values are 15 ADC for the MAPMTs and 270 ADC

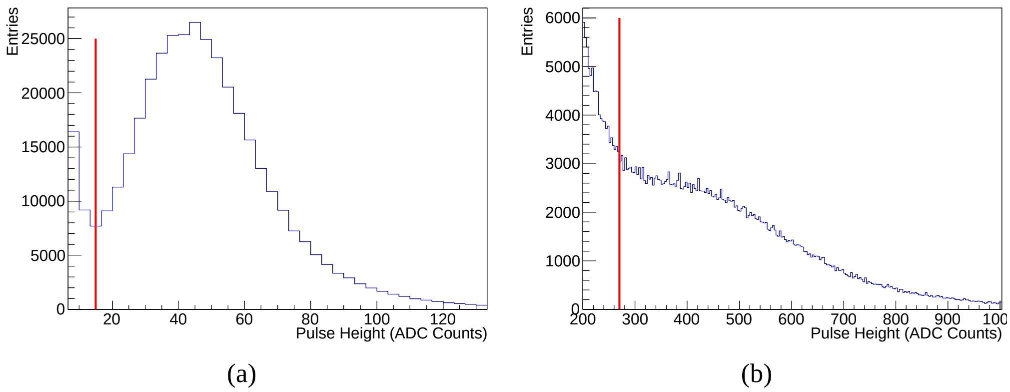

Figure 4.17: a) The MAPMT and b) the SiPM threshold value to distinguish the noise from the signal (the red lines): the pulse height distributions have been computed with the equalized signals and the bar with the maximum signal in the event.

for the SiPMs.

4.2.2.5 The Spatial Resolution and the Efficiency

To identify the particle hit position on the different prototype layers, the cluster identification has been performed (with the algorithm described in section 3.2.2.2) independently for the MAPMT and the SiPM readout system. As shown in figure 4.18, in most of the events there is one cluster with a single bar. Larger numbers of bars per cluster are mainly due to the particles which are not perpendicular to the layer or to different particles which hit the prototype but not the trigger and the tracking system.

The spatial resolution has been evaluated using the same residual method presented in section 3.2.2.2: just the one-cluster events have been selected and the differences between the position reconstructed by the tracking system (i.e the projection from the BCs to the surface of the layer prototype) and the one measured by the prototype layers themselves (defined as the cluster position) have been evaluated. Figure 4.19 presents the distribution of the residuals of the first layer of the LEP detector with the gaussian fit for the MAPMT and SiPM case: the MAPMT σ is 5.1 mm while the SiPM one is 4.6 mm.

The efficiency has been computed with equation 3.4 where the $target$ and the $good$ events are defined separately for each layer. An event is tagged as a $target\ event$ if the surrounding layers (like in a sandwich) have a single cluster with a residual smaller than $3\times\sigma_{layer}$. For the first and the second-last LEP layers, the sandwich condition is applied to the two following or preceding layers. An event is identified as $good$ if there is one cluster in the layer under test within 3

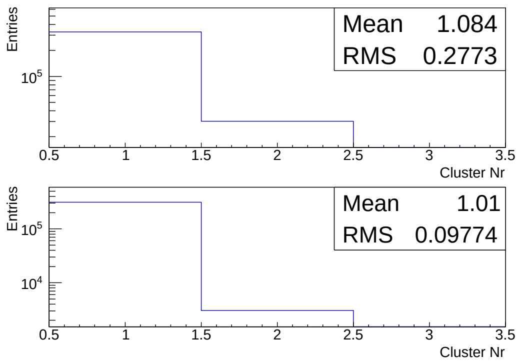

(a)

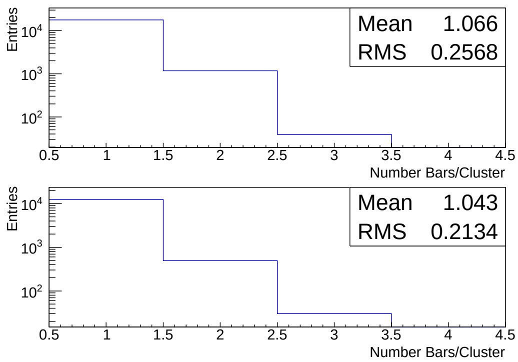

(b)

Figure 4.18: The distributions of the number a) of clusters and b) of bars per cluster for the MAPMT (top) and the SiPM (bottom).

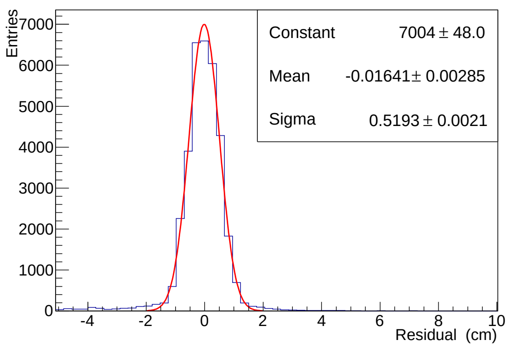

(a)

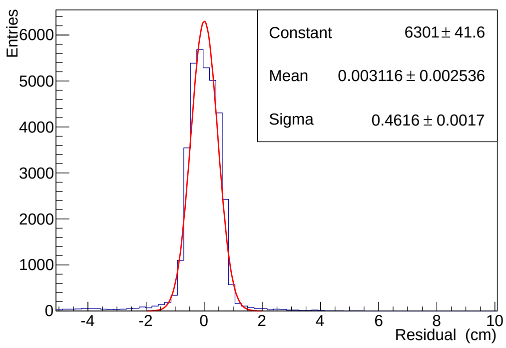

(b)

Figure 4.19: a) The MAPMT and b) the SiPM first layer residual distribution fitted with a gaussian function to evaluate the spatial resolution (i.e. the σ parameter).

times the sigma resolution.

Figure 4.20 presents the two dimensional efficiency plots of the first LEP layer for the MAPMT and the SiPMs, while figure 4.21 shows the projections along the

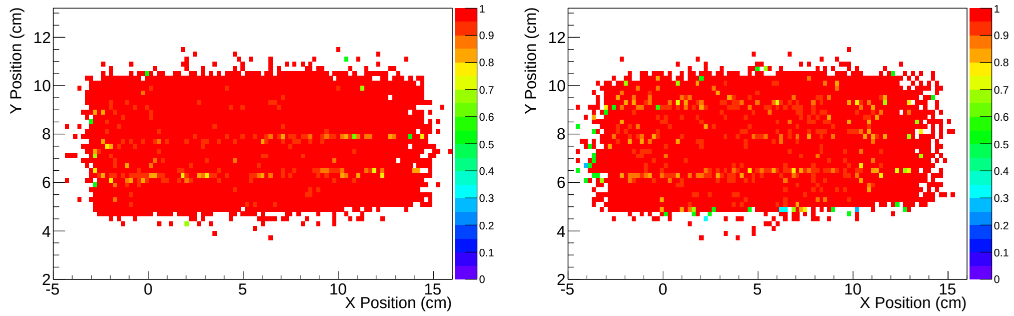

(a) (b)

Figure 4.20: The two-dimensional efficiency profile histograms of the LEP first layer readout by a) the MAPMT and b) the SiPMs.

y direction: the drops in the efficiency mark the boundary regions of the bars. The

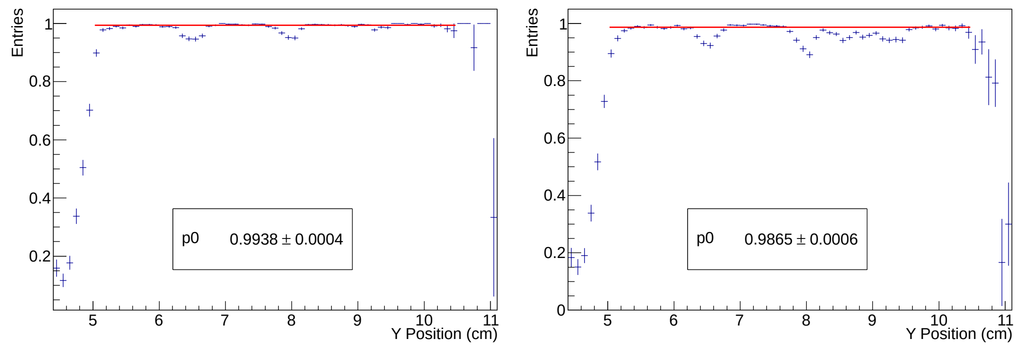

(a) (b)

Figure 4.21: The projections along the y direction of the 2D efficiency profiles for the first LEP layer readout by a) the MAPMT and b) the SiPMs.

fit with a constant function gives a value of 99.38±0.04% for the MAPMT and 98.65±0.06% for the SiPMs.

Considering the efficiency value of each layer as presented in figure 4.22, the MAPMT one is constant (larger than 90%) while the SiPMs one indicates that the small Signal to Noise Ratio limits the performance of the system: in fact, an increase of the inefficiency is visible in the last layers of the LEP block under test. The same result has been obtained during the test at CERN (as will be presented in section 5.1.4.2), where the LEP efficiency has been measured with two different methods.

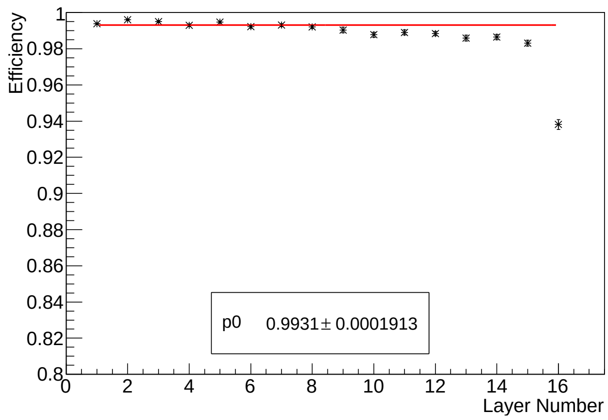

(a)

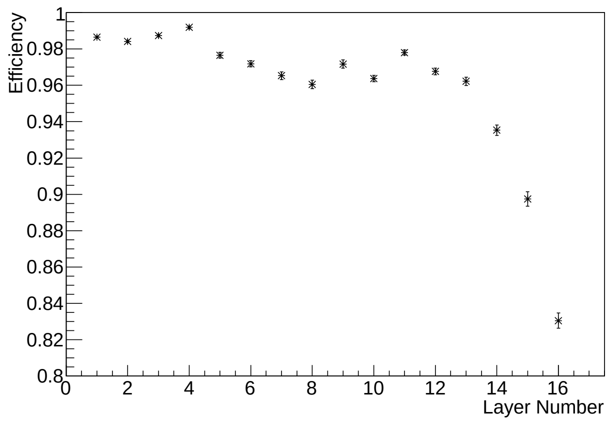

(b)

Figure 4.22: The efficiency of the layers readout by a) the MAPMT and b) the SiPMs.

Chapter 5

The LEP Beamtest Results

As already described in chapter 4, the Large EMR Prototype has been tested for the first time with cosmic rays obtaining good results about the system overall stability. After the commissioning phase, the prototype has been also tested with particle beams at one of the extracted lines of the European Organization for Nuclear Research (CERN).

The first part of this chapter describes the beam and the experimental setup. In the second part of the chapter, a presentation of the data taking procedure and the analysis results is given. The results are presented in terms of spatial resolution and detection efficiency for both the readout systems based on MAPMTs and SiPMs.

5.1 The T9 Beamtest

The Large EMR Prototype has been tested on the T9 beamline at the CERN PS East Area. The T9 beam is a charged particle secondary beam produced by the ProtoSynchroton (PS) primary 24 GeV/c proton beam hitting a target. The resulting beam is a mixed negative or positive beam (typically μ, π and e) in the 1-15 GeV/c momentum range [77] and has typical intensities of the order of 10^4 particles per bunch (the so called $spill$). The spill lasts around 400 ms with a period of 45 s; depending on the users, between 1 and 3 spills are available to the beamline for each period. The selection of the particles momentum is performed by a horizontal collimator placed at the beginning of the line, while the beam intensity can be adjusted with a vertical collimator. The beamtest has been performed using particles with a momentum of 6 GeV/c, so that the beam was mainly composed by pions which cross the whole detector (i.e. all the 48 LEP layers) as Minimum Ionizing Particles (MIPs).

An example of the beam profile both in the horizontal and vertical direction as measured by the Silicon Beam Chambers is presented in figure 5.1. The RMS

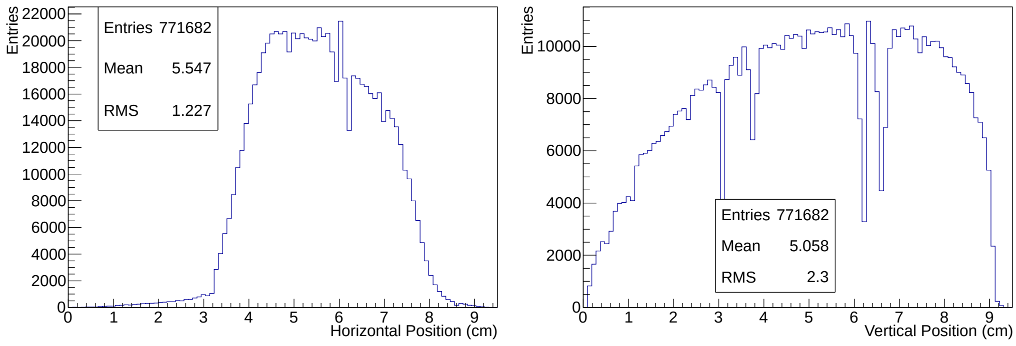

(a) (b)

Figure 5.1: The beam profile in the a) horizontal and b) vertical direction as measured by the BCs.

of the horizontal profile is 1.22 cm, while the shape of the beam in the vertical direction is due to the settings of the collimators chosen to cover the whole LEP extension: the RMS of the vertical profile is in fact ∼2.3 cm. The entries drops visible in the plots are due to non working strips, which were disabled and not taken into account in the analysis.

The beam divergence is shown in figure 5.2. The angular distribution of the beam particles (whose peak is not centered on 0 because of the alignment of the BCs in the horizontal direction) has been fitted and the divergence is given by the $sigma$ parameter. The values are 4.33±0.01 mrad for the horizontal direction

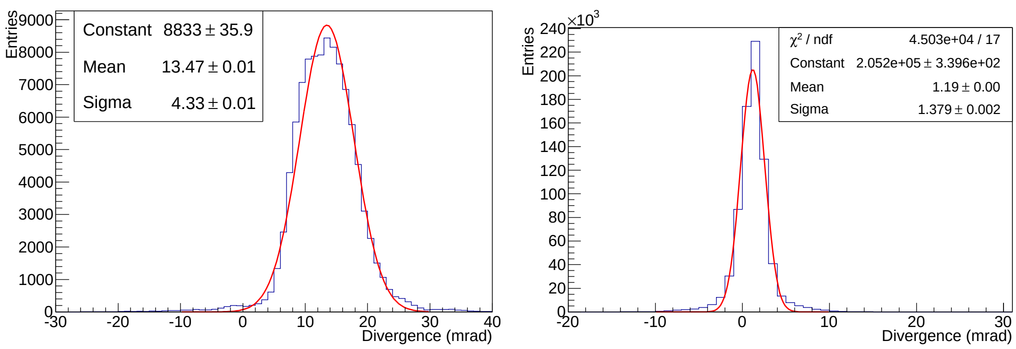

(a) (b)

Figure 5.2: The beam a) horizontal and b) vertical divergence.

and 1.48±0.02 mrad for the vertical one: for these tests there was no particular requirement on the beam divergence.

The main goal of the T9 beamtest is to evaluate the performance of such a large number of SiPMs used as the readout system of the scintillating bars. Although initially the Large EMR Prototype has been developed to test the Electron Muon Ranger calorimetry capability, in this beamtest only the tracker performance has been evaluated and the results are presented in terms of spatial resolution and detection efficiency for each layer of the prototype.

5.1.1 The Experimental Setup and the DAQ System

As shown in figure 5.3, the beamtest experimental setup consists of:

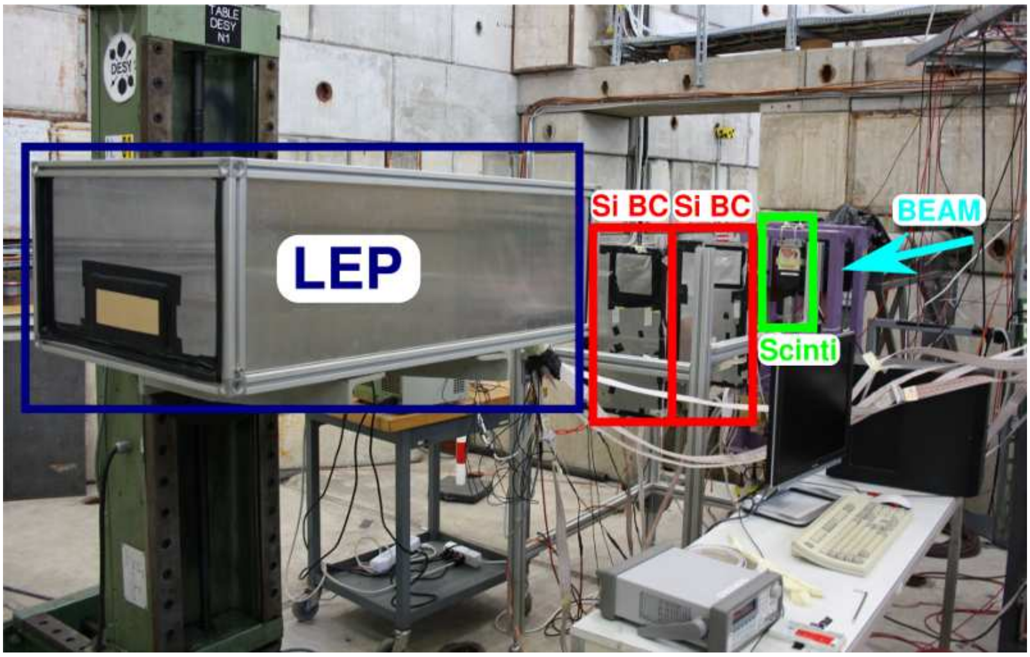

Figure 5.3: The experimental setup at the T9 beamline: it consists of a scintillator providing the trigger signal, a couple of BCs for the particles tracking and LEP (the tracker under test).

- the 10×10 cm^2 scintillator (section 4.2.1) placed at the beginning of the line for the trigger generation;
- a couple of Silicon Beam Chambers (section 3.2.1.2) for the particle track reconstruction;
- the Large EMR Prototype. The bias voltage of the LEP MAPMTs has been set at 850 V, while the 192 SiPMs have been biased with three different

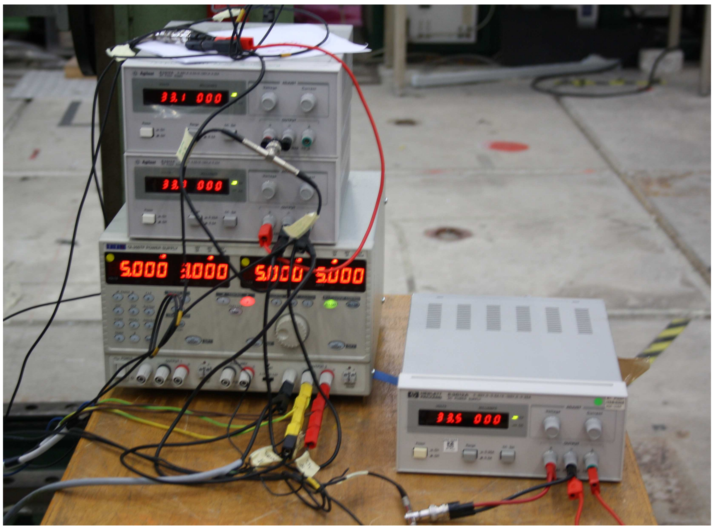

Figure 5.4: A photo of the three power supplies used to bias the 192 LEP SiPMs.

(one for each block) power supplies (figure 5.4), whose values (presented in table 5.1) have been chosen in order to obtain an overvoltage of about 3 V.

Block	**Bars Number**	**Voltage (V)**
1	1→64	34.00
2	65→128	34.00
3	129→192	34.55

Table 5.1: The three different bias values of the LEP SiPMs.

The Data AcQuisition system is similar to the one used for the cosmic ray tests performed both with the small scale EMR prototype and the Large one (see section 3.2.1.5 and 4.2.1). As shown in figure 5.5, it is based on a standard VME system (controlled by a SBS Bit 3), which hosts several boards:

- 4 VME Readout Boards (VRB, developed for EMR) that are responsible of the MAROC configuration, the readout sequence generation and the during-spill data storage;
- a trigger board which generates the trigger and sends it to the Master VRB which in turn distributes it to the other VRBs.

The VRBs generate the readout sequence for the MAROC boards and the BCs repeater + ADC system. The data are stored in 2 32-bit Mword memories in the

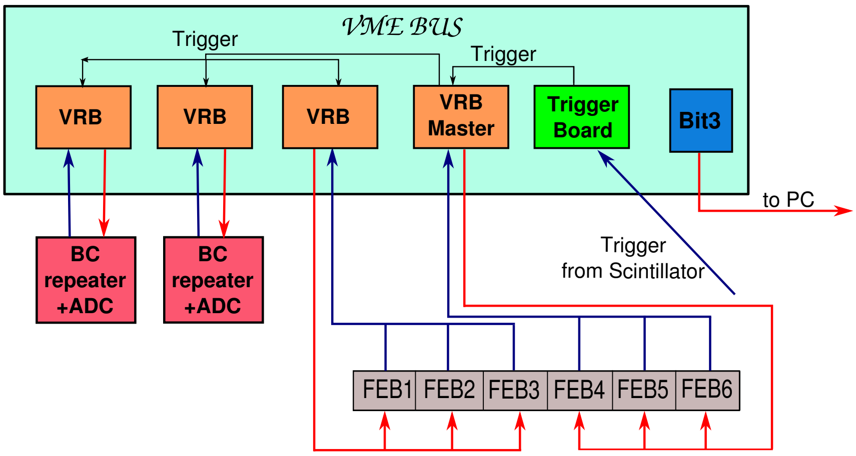

Figure 5.5: The scheme of the T9 beamtest DAQ system: the red lines represent the output signals of the control boards in the VME crate, while the blue lines are the outputs from the detectors.

VRBs during the spill; this readout system has allowed a maximum theoretical speed of 4 kHz, which could not be completely exploited due to the beam intensity: around 1200 events per spill were acquired with respect to the possible 1600 events.

As in the previous tests, the DAQ software is written in C while Tcl/Tk is used for the graphical interface; the raw data were stored in PAW ntuples which have been processed to obtain the DST files, where only the one-cluster events of the BCs are selected.

The test procedure (which is quite similar to the ones described in chapter 3 and 4) consists of the following steps:

- pedestal runs (acquired with 200 random triggers) and low statistics particle runs are acquired changing the settings of the MAROC parameters: the detector performance has been evaluated in terms of noise RMS and SNR in order to find the best configuration optimizing the SiPMs performance;

- a pedestal run to evaluate the ASIC channels baseline and a high statistics run are acquired with the best configuration.

5.1.2 The Slow Shaper Performance

Once the MAROC gain has been set at 40 to avoid a lot of events in saturation for the SiPMs and at 64 for the MAPMTs, the first step of the test has been performed using the slow shaper.

As presented in section 4.2.2.1, the longest shaping time is obtained setting the three slow shaper capacitors in the *on* mode ({1,1,1}). Figure 5.6 presents the pedestal profile of the six LEP boards in this slow shaper configuration for the

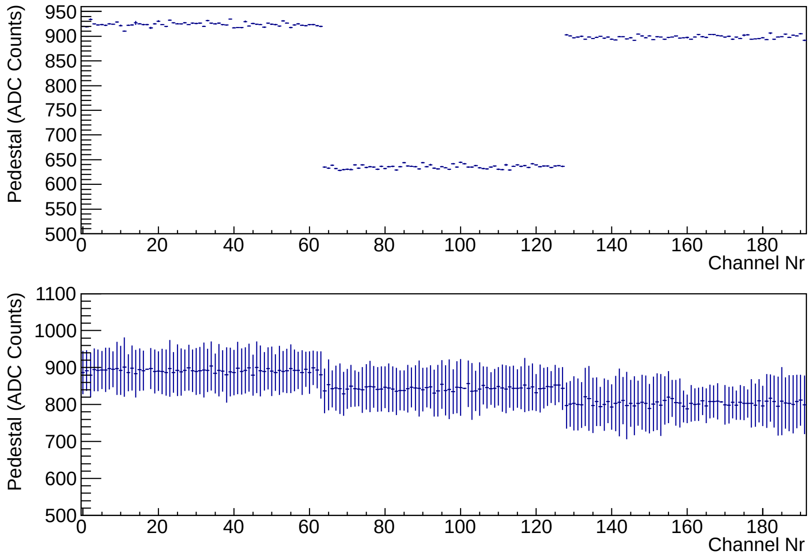

Figure 5.6: The pedestal profile of the six LEP boards: the top plot is obtained with the MAPMTs while the bottom plot with the SiPMs.

MAPMTs (top) and the SiPMs (bottom): the pedestal value is different for each board.

The noise RMS plotted as a function of the channel number for the MAPMTs is presented in figure 5.7(a) (the blue histogram) and has an average value of about 1.5 ADC, while in figure 5.7(b) the blue histogram shows the same plot for the SiPMs with a mean value of the order of 80 ADC. Considering the results presented in section 4.2.2.2, the evaluation of the noise RMS once the subtraction of the common mode (which represents the overall movement of the baseline common to all the ASIC channels) has been performed only for the MAPMT channels (the red histogram).

The green histogram in figure 5.7(b) presents the noise RMS distribution with a different setting of the slow shaper capacitors corresponding to a faster shaping time ({0,1,1}). The net result is a decrease of the RMS value for the SiPMs channels: the average value is around 60 ADC, while in the MAPMT case it is already so small that the difference cannot be appreciated.

In order to determine the best slow shaper configuration the gain of both settings has been evaluated. Figure 5.8 shows the pulse heights of a bar (performed when this is the one with the maximum signal in the event) fitted with a Landau + gaussian function for the {1,1,1} configuration (plot 5.8(a)) and the {0,1,1} one

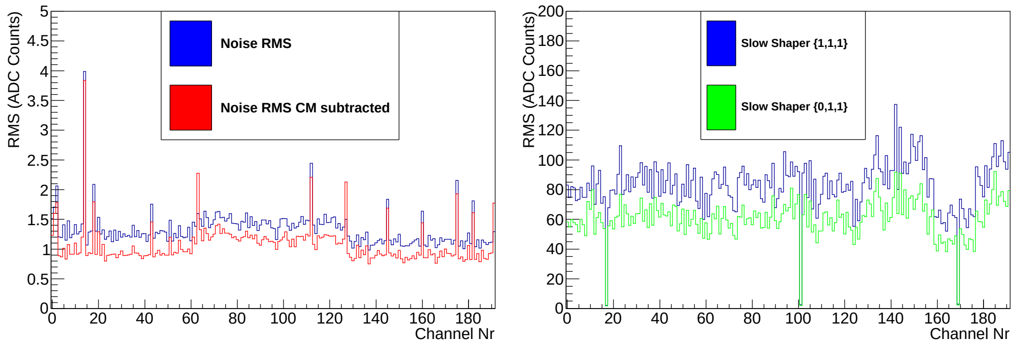

(a) (b)

Figure 5.7: The noise RMS (blue histogram) for each ASIC channel for a) the MAPMTs and b) the SiPMs in the $\{1,1,1\}$ slow shaper configuration. The green histogram for the SiPMs corresponds to the $\{0,1,1\}$ configuration, while the measurement of the common mode subtracted noise RMS has been performed only in the MAPMT case (the red histogram).

(plot 5.8(a)). The MP parameters extracted from the fits are 387 ADC for the first

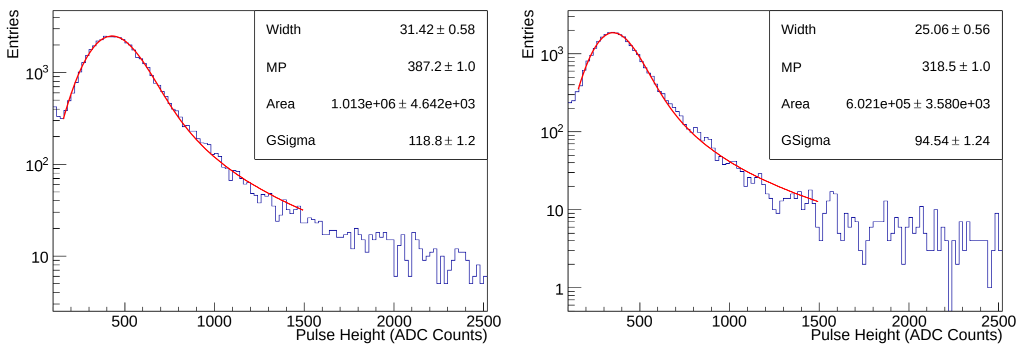

(a) (b)

Figure 5.8: The pulse height distribution in a) the $\{1,1,1\}$ and b) the $\{0,1,1\}$ slow shaper configuration.

case and 318 ADC for the second one. Thus, the best configuration of the slow shaper capacitors (i.e the one which optimizes the SiPM SNR) is the $\{0,1,1\}$ one: even being the gains of the two configurations similar ($\sim$1.2), the $\{0,1,1\}$ noise RMS is a factor 0.75 smaller than the one obtained with the $\{0,1,1\}$ configuration.

5.1.3 The Hold Setting

A study to optimize the SiPMs SNR varying the hold has also been performed. Considering the best configuration of the slow shaper capacitors ({0,1,1}) and the gain at 40, the pull distribution of each LEP layer has been computed for three different hold values: 5 ns, 8 ns and 10 ns.

Figure 5.9(a) presents an example of the pull distribution of the first LEP layer for a hold of 5 ns with the fit with a Landau + gaussian function. Figure 5.9(b)

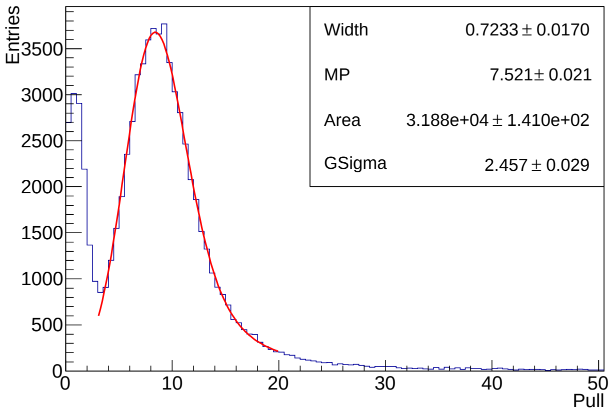

(a)

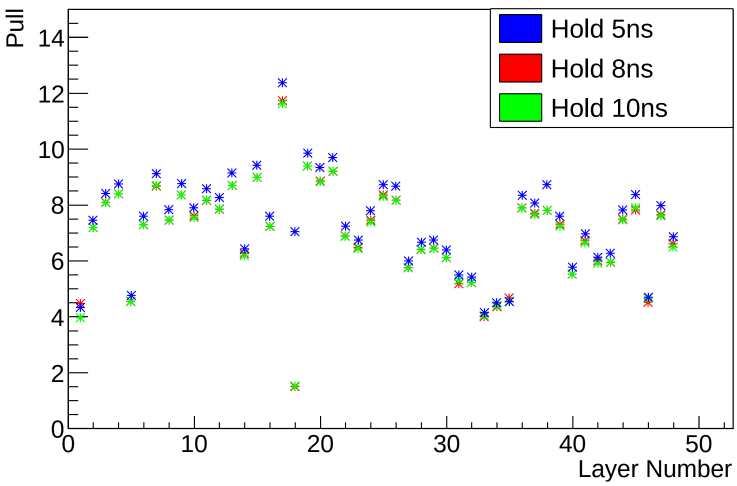

(b)

Figure 5.9: a) The first SiPM layer pull distribution and b) the pull values as a function of the layer number for three different hold values.

shows the pull most probable values for the 48 layers which are summarized in table 5.2. The best hold configuration (i.e. the one with the largest pull values)

Hold (ns)	Signal to Noise Ratio
5	7.39
8	6.90
10	6.88

Table 5.2: The average of the pull for three different hold values.

corresponds to a hold of 5 ns (the blue points in the plot).

Thus, the data taking configuration was the following:

- a slow shaper configuration of $\{0,1,1\}$;
- a hold value of 5 ns;
- a SiPM gain of 40;
- a MAPMT gain of 64.

5.1.4 The Analysis Results

As in the cosmic ray test, the first step of the data analysis is the equalization of the bars outputs (with the same procedure described in chapter 4), to be able to set a single threshold to distinguish noise from signal events.

Figure 5.10 presents the distribution of the pulse height (once the subtraction of the pedestal and the common mode value (if needed) has been performed) of two MAPMT layers (figure 5.10(a)) and two SiPMs ones (figure 5.10(b)): the plots have been computed selecting, event by event, the bar of these layers with the maximum signal.

As previously described in section 4.2.2.4, the bar equalization has been performed considering the pulse height distribution of each single bar and rescaling each mean value to the first bar one, separately for both readout systems. The same distributions of figure 5.10, once rescaled, are shown in figure 5.11. A threshold (represented by the red lines in the plots) to distinguish the noise events from the signal ones has been set at 80 ADC for the MAPMTs and at 150 ADC for the SiPMs.

The analysis has allowed to identify the non working SiPMs that is the ones not interfaced to the two WLS fibers coming out from the bars and the broken ones, as summarized in table 5.3. Less than 7% of the 192 LEP SiPMs have been considered as “bad” devices.

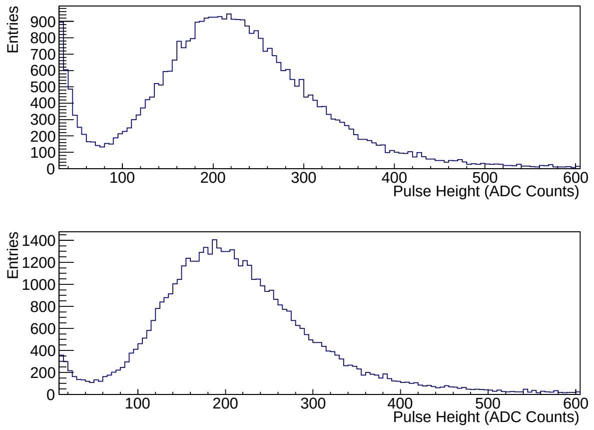

(a)

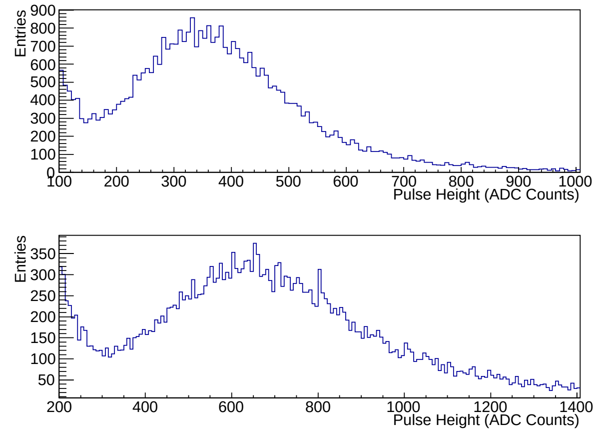

(b)

Figure 5.10: The pulse height distributions of two a) MAPMT layers and b) SiPM ones before the signal equalization.

LEP Block	Not Connected SiPMs	Not Working SiPMs	Working SiPMs (%)
1	4	1	92.2
2	2	1	95.3
3	4	1	92.2
Total	10	3	93.2

Table 5.3: The number and the percentage of the working SiPMs for each LEP block and for the overall detector.

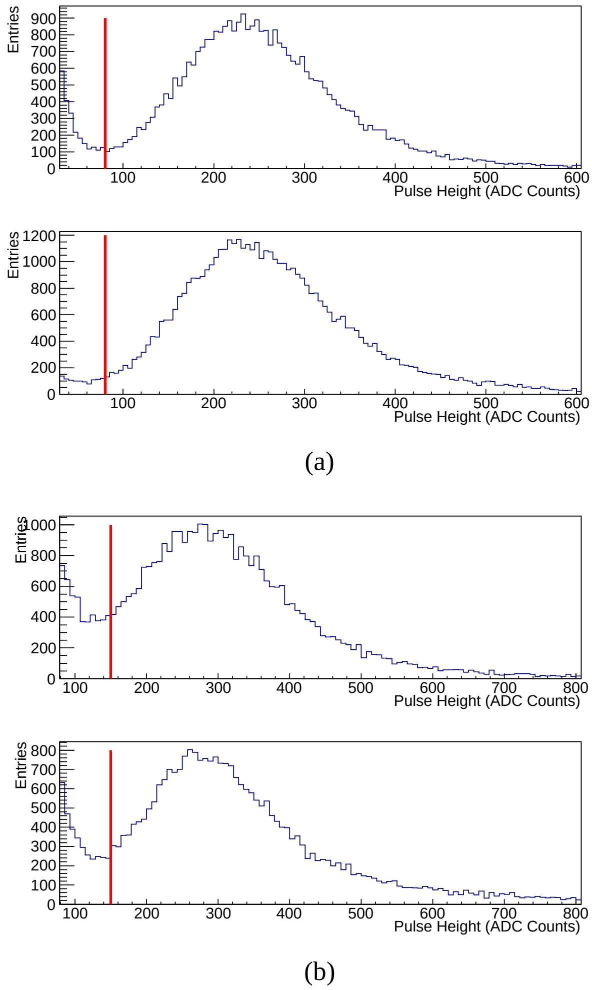

Figure 5.11: The rescaled pulse height distributions of two layers readout by a) the MAPMTs and b) the SiPMs: the red lines represent the threshold to distinguish the signal from the noise.

5.1.4.1 The Spatial Resolution

Once the outputs have been equalized, the cluster identification algorithm (described in section 3.2.2.2) has been used to identify the particle hit position on the different LEP layers. The cluster identification has been performed independently for each of the 48 LEP layers and for the MAPMTs and the SiPMs. Figure 5.12 presents the number of clusters in each of the three LEP blocks, while figure 5.13 shows the distributions of the number of bars per cluster. As in the previous tests, also in this case in most of the events there is one cluster with a single bar.

Figure 5.14(a) and 5.14(b) present the residual distribution for the MAPMT

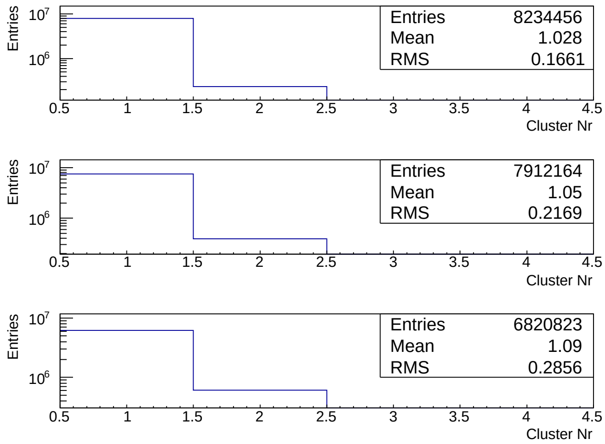

(a)

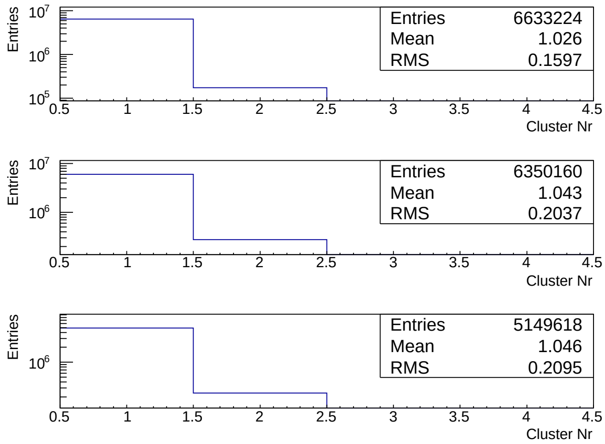

(b)

Figure 5.12: The distributions of the number of clusters for a) the MAPMT and b) the SiPM LEP blocks.

and the SiPM first layer fitted with a gaussian function. As expected, the $sigma$ values of the fits (i.e. the spatial resolution) are comparable: for the MAPMTs σ is equal to 4.16 mm while for the SiPMs 3.92 mm.

The spatial resolution has been evaluated independently for the 48 MAPMTs and SiPMs layers as shown in figure 5.15. In both cases, the spatial resolution gets larger with the increase of the layer number because of the multiple scattering and the energy loss during the particle travel; however, the MAPMTs have σ values larger than the SiPMs ones. This is due to the cross-talk effect which may cause the misidentification of the hit position increasing thus the residual.

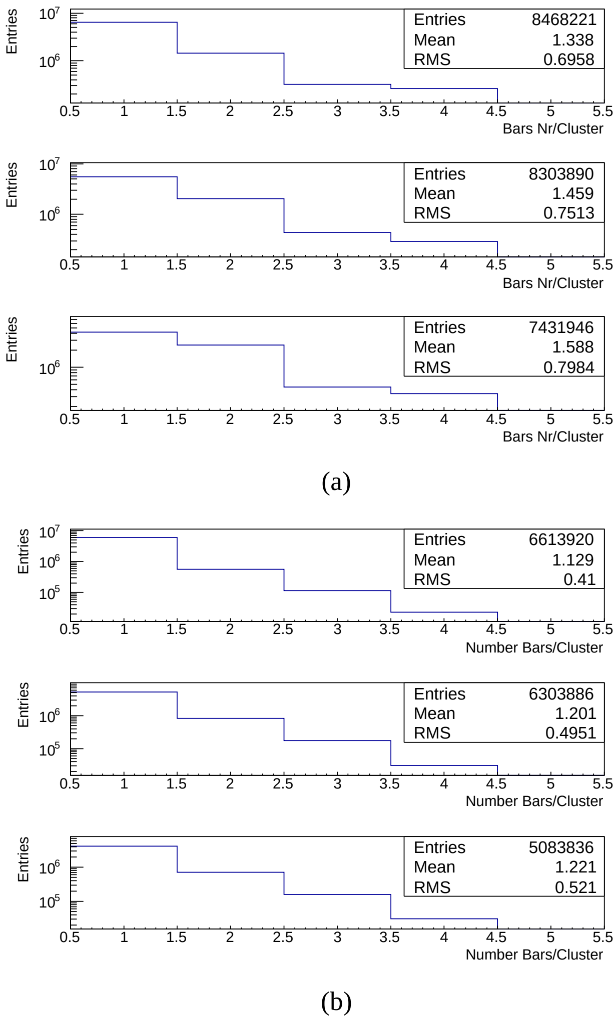

Figure 5.13: The distributions of the number of bars per cluster for a) the MAPMT and d) the SiPM LEP blocks.

5.1.4.2 The Detection Efficiency

The procedure to evaluate the detection efficiency for all the LEP layers is the one presented in section 4.2.2.5.

Figure 5.16(a) and 5.16(b) present the 2D efficiency profile of the first LEP layer for the MAPMT and the SiPMs. In both cases, the whole layer is very efficient. As already performed in the commissioning phase, the projections along the y-direction of the two-dimensional plots have been computed to give a precise measurement of the LEP efficiency. Figure 5.18 presents the projections of one of the first LEP layers fitted with a constant function obtaining an efficiency equal to

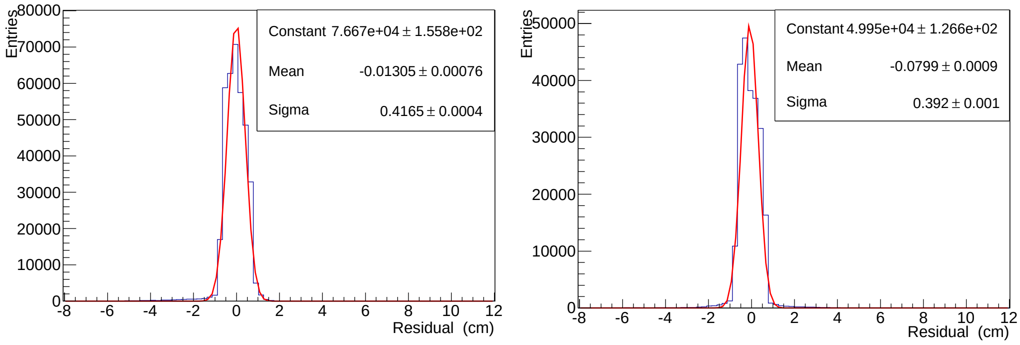

(a) (b)

Figure 5.14: a) The MAPMT and b) SiPM first LEP layer residual distribution fitted with a gaussian function: the σ value represents the spatial resolution.

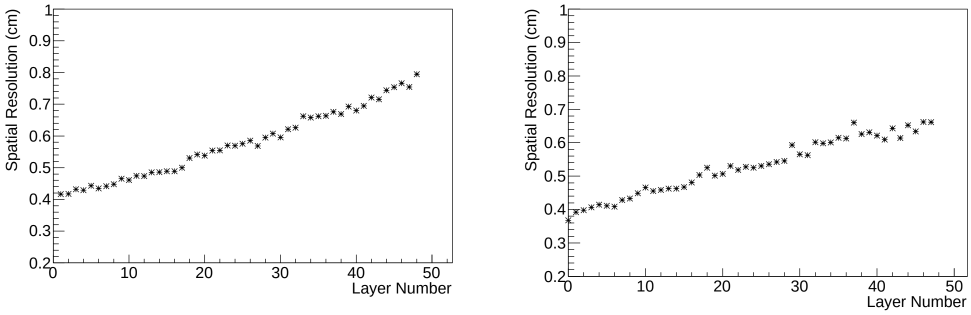

(a) (b)

Figure 5.15: The trend of the spatial resolution for a) the MAPMT and b) the SiPM readout system.

99.73±0.01% for the MAPMT and to 97.98±0.03% for the SiPMs.

Considering the overall efficiency of the detector, as shown in figure 5.18(a), all the MAPMT layers have an efficiency larger than 97% (with an average value equal to 99.5%), while in the SiPMs case a loss of efficiency in the layers belonging to the last LEP block (corresponding to the one tested with cosmic rays, chapter 4) is clearly visible.

The same result has been obtained computing the efficiency of each bar in a self-consistent way, that is not using the tracking system (as presented in figure 5.19). Also in this measurement, the efficiency is defined by the same equation of the previous method (equation 3.4) and the $target$ and the $good$ events are defined separately for each bar: an event is tagged as a $target$ event if the bars in the same vertical position of the layer before and the one after the layer under test have a signal larger than the threshold (150 ADC) and the event is also identified

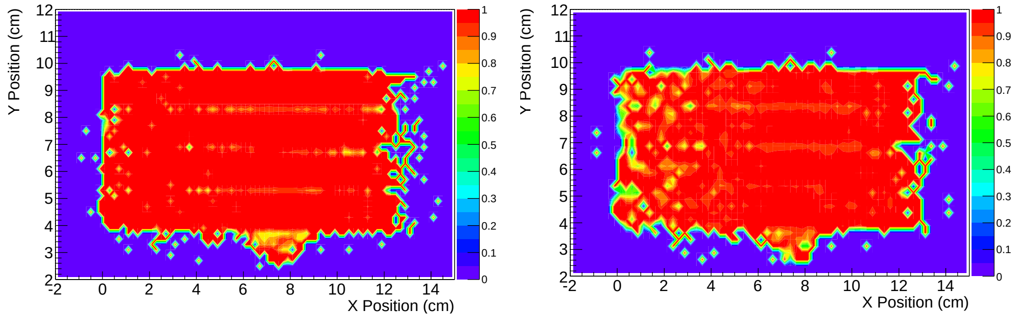

(a) (b)

Figure 5.16: The two-dimensional efficiency profile histogram of the LEP first layer readout by a) the MAPMT and b) the SiPMs.

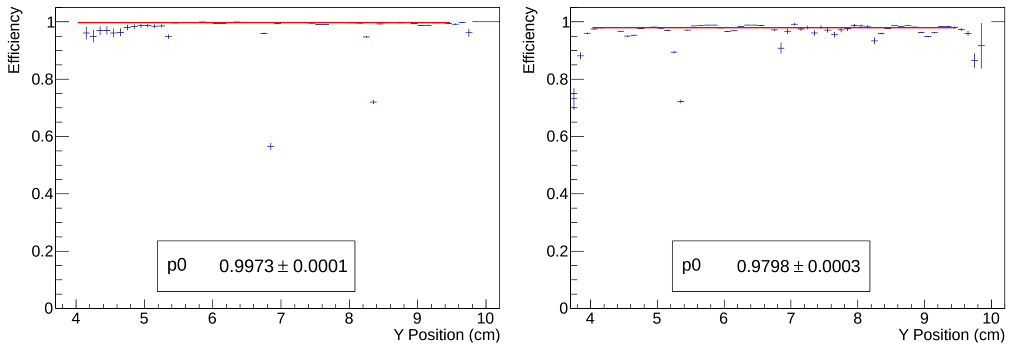

(a) (b)

Figure 5.17: The y-direction profile histogram of the first a) MAPMT and b) SiPM layer fitted with a constant function to evaluate the efficiency.

as $good$ if the signal of the selected bar is larger than the threshold. In this case, the efficiency of the first and the last layers and of the bars sandwiched by a not working SiPM have not been taken into account.

Figure 5.20(a) shows the distribution of the bars efficiency with a mean value larger than 93% while in figure 5.20(b) the same efficiency values as a function of the bar number are presented. This result is in agreement with the first method (figure 5.18(b)) and with the trend of the efficiency obtained during the cosmic rays tests and presented in section 4.2.2.5: in fact, the bars belonging to the third LEP block (from 128 to 192) are clearly less efficient than the other ones.

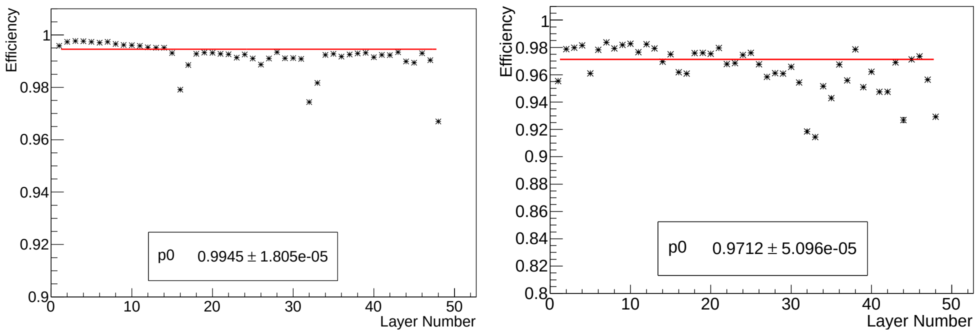

(a) (b)

Figure 5.18: The efficiency of each layer readout by a) the MAPMTs and b) the SiPMs.

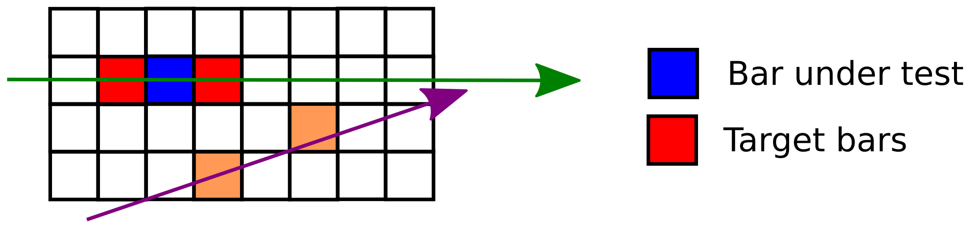

Figure 5.19: The self-consistent method for the measurement of the bar efficiency: an event is tagged as a $target$ event if the signals of the bars (the red ones) before and after the one under test are larger than the threshold and as a *good* one if the bar under test (the blue one) has a signal larger than a threshold. For this measurement only the particles that hit the bars at the same vertical position are taken into account; target events like the orange ones are not considered.

5.1.5 The Results with a Different SiPMs Bias

In the last phase of the beamtest, the SiPMs performance has been evaluated with a lower biasing voltage (table 5.4), the same MAROC parameters and MAPMTs

Block	Bars Number	Voltage (V)
1	1→64	33.00
2	65→128	33.00
3	129→192	33.55

Table 5.4: The values of the SiPMs bias values used in the last beamtest phase.

settings (section 5.1.3).

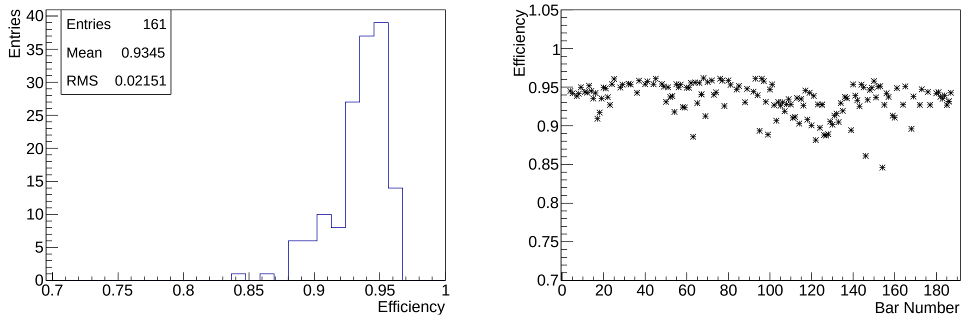

(a) (b)

Figure 5.20: The efficiency of almost all the LEP bars: a) the overall distribution; b) the efficiency as a function of the bar number.

The analysis procedure is the same of the previous section. Figure 5.21(a) and 5.21(b) show the spatial resolution and the efficiency for each of the 48 LEP layers readout by SiPMs. The trend of the spatial resolution is correct while with

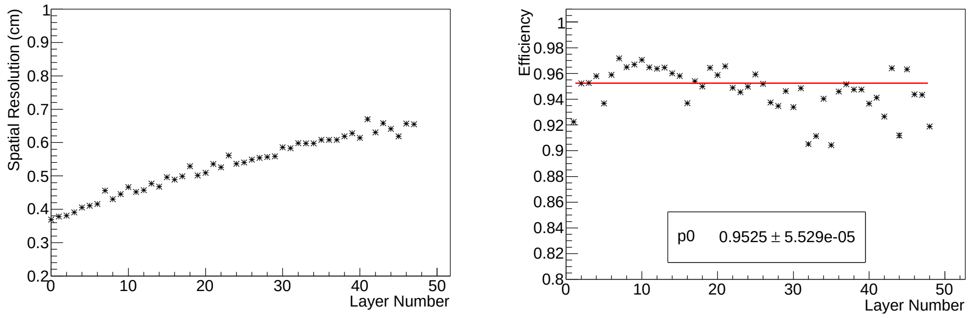

(a) (b)

Figure 5.21: a) The spatial resolution and b) the efficiency of each LEP layer readout by the SiPMs biased with a smaller voltage.

the smaller bias voltage there is a drop in the efficiency (which is of the order of 95% with respect to $\sim$97%).

Conclusions and Outlooks

The PhotoMultiplier Tube can be considered the most widespread photodetector in different physics fields: it has pros such as the capability to detect very low light fluxes, high sensitivity and high gain but also cons as the sensitivity to magnetic fields, a low quantum efficiency and the need of high voltage. For these reasons, in the early ’70s a new type of photodetector based on semiconductors (called solid state photodetector) has been developed as an alternative to the standard PMT. Among these new photodetectors, Silicon PhotoMultipliers (SiPMs) represent one of the most probable alternatives for many experiments in several physics fields (from high energy physics to space physics) which have stringent requirements such as the large number of sensors, low power consumption and insensitivity to magnetic fields.

A SiPM consists of a matrix of pixels (typically 500-4000 pixels/mm^2) with dimensions in the 20-200 μm range and joined together in parallel on a common Silicon substrate. Each pixel works as an independent Single Photon Avalanche Photodiode (SPAD) operated in limited Geiger mode (i.e. as a digital device), while the sum of all the SiPM pixels outputs is proportional to the energy deposited by the particle. The high internal gain (of the order of 10^6), high detection efficiency, low bias voltage, very good time response and the insensitivity to magnetic fields represent the main advantages with respect to MAPMTs. On the other hand, SiPMs have important limits such as the dark count rate (which is of the order of one MHz in comparison to the PMT one which is of the order of one kHz) and the fill factor (defined as the ratio between the active area of the detector and its whole area).

The FACTOR (Fiber Apparatus for Calorimetry and Tracking with Optoelectronic Read-out) collaboration (now TWICE, Techniques for Wide-Range Instrumentation in Calorimetry Experiments) is one of the research groups who intends to improve the SiPM features in terms of noise, detection efficiency and radiation hardness. It is being supported by the Italian Institute of Nuclear Physics and actively collaborates with FBK-irst (Fondazione Bruno Kessler) to develop and optimize a new SiPM technology. The final goal is the assembly and commissioning of scintillator based systems readout by SiPMs for for calorimetric and tracking applications.

This thesis work has been performed in the framework of the FACTOR/TWICE collaboration and its goal was the evaluation of the performance of SiPMs used as a readout system of scintillating bars detectors and the comparison of their behaviour with the MAPMTs one. Two different prototypes of the MICE Electron Muon Ranger detector (developed by the Como/Trieste group) has been used for the tests: they are based on scintillating bars whose light is carried out by Wave-Length Shifter fibers and readout both by MAPMTs and SiPMs. In all the tests performed during this thesis work, the photodetectors signals were processed by a FrontEnd Board whose main element is the MAROC3 ASIC, which in fact has been designed for the readout of 64-channel MAPMTs. Each ASIC channel consists of a preamplifier with a variable gain, two shapers (a slow one for the analog readout and a fast shaper for the digital output), a sample&hold circuit and a discriminator. The MAROC3 ASIC provides one multiplexed analog output and 64 digital ones at the same time: the multiplexed output (with a maximum clock frequency of 10 MHz) is digitized by an external ADC (AD9220, Analog Devices) integrated on the frontend board, while the 64 fast shapers outputs are discriminated to generate 64 independent digital outputs (whose width is a function of the input amplitude). Several characterization tests have been performed on the MAROC boards as presented in Appendix A.

The first tests have been performed with the small scale EMR prototype, which consists of 8 layers of 10 19.1 cm long extruded scintillating bars whose light is carried out by 4 1.2 mm diameter WLS fibers. Eight bars of the first layer have a double readout system: on one side the light produced by the incident particles is readout by a 64-channel MAPMT and on the other side by 8 1 mm diameter FBK-irst SiPMs. The MAPMT performance and the SiPMs one have been compared in terms of Signal to Noise Ratio, spatial resolution, detection efficiency and timing resolution (as shown in chapter 3). The analysis results show that SiPMs have a smaller SNR with respect to the MAPMT because of their large intrinsic noise; on the other hand, comparable results on the spatial resolution ($\sim$6.8 mm) and efficiency (of the order of 94%) have been obtained. As far as the timing resolution is concerned, the measured value is of the order of 2.5 ns for both, which is an upper limit because it is the sum of different effects such as the intrinsic timing resolution of the photodetector, the characteristic timing of the scintillator and the WLS fibers light emission and the timewalk of the electronics chain. A clear demonstration of the better intrinsic timing resolution of SiPMs has been obtained measuring the light travel time in the scintillating bar, which is of the order of 1 ns.

The tests performed with the Large EMR Prototype represent the heart of this thesis work (chapter 4 and 5). LEP is a totally active scintillating detector consisting of 192 rectangular bars arranged along the x direction in 48 layers and divided in three blocks. The light is carried out by two 0.8 mm diameter WLS fibers per bar which have been glued in the bar hole: on one side they have been interfaced with three Hamamatsu 64 channel MAPMTs, while on the other with 192 2.8 mm diameter FBK-irst SiPMs. During the commissioning phase the first 16 layers of the detector have been tested with cosmic rays obtaining a good stability of the overall system. LEP has been also tested at CERN with a 6 GeV/c momentum particle beam and characterized in terms of spatial resolution and detection efficiency. The spatial resolution has been measured for each of the 48 prototype layers using the residual method: both in the MAPMTs and SiPMs case, the spatial resolutions are in the range of 4.0-7.5 mm and get larger with the increase of the layer number because of the multiple scattering and the energy loss during the particle travel. As far as the MAPMTs detection efficiency is concerned, an efficiency value larger than 97% for all the layers has been measured. In the SiPMs case, the efficiency has been evaluated with two different methods one of which does not use the tracking system: in both cases, a loss of efficiency in the layers belonging to the last LEP block has been measured; however, an efficiency larger than 90% has been obtained for all the 48 layers.

The measurement of a smaller efficiency in the SiPM case with respect to the MAPMT one is mainly due to the noise of the device itself interfaced to the readout ASIC. As shown in chapter 4 and 5, the MAROC ASIC can be tuned depending on the application and varying its parameters (i.e. the shaping timing) it is possible to increase the SiPM SNR.

As far as the next future is concerned, a new version of the electronics has to be developed: considering the MAROC features the electronics chain has to be improved to optimize the readout of SiPMs signals. An alternative can be represented by the development of a new frontend board based on a different ASIC: the EASIROC (Extended Analogue Si-pm Integrated ReadOut Chip), which is an ASIC developed specifically for the SiPMs readout. It has 32 channels with a 4.5 V range 8-bit DAC for adjusting the bias (and thus the gain) of the single SiPM and a maximum multiplexed charge up to 320 pC is available (which has to be compared with the MAROC one which is of 5 pC). Each channel is made of 2 variable gain pre-amplifiers followed by 2 tunable shapers and a track and hold. The main advantages of the readout system based on the EASIROC ASIC are represented by:

- the large dynamic range, which will solve the saturation problem;
- the possibility of setting the overvoltage on a SiPM by SiPM basis.

Appendix A

The Tests on the MAROC3 Boards

The readout electronics of the two prototypes, the small scale EMR prototype and the Large EMR Prototype, used to perform the SiPM tests in this thesis work, is based on a prototype of the EMR detector FrontEnd Boards (FEB [78]). In all the tests, the two scintillation light readout systems are interfaced with a MAROC3 board (figure 3.11), whose main element is the 64-channel Multi-Anode Read-Out Chip 3 (MAROC3) ASIC [79].

After a brief introduction on the board and its ASIC, this appendix describes the bench tests of all the LEP MAROC boards before their final assembly on LEP to evaluate the functionality and the uniformity of the boards themselves.

A.1 The MAROC3 ASIC

The MAROC3 is the third version of the ASIC developed by the Omega group (LAL[1], Orsay) for the ATLAS luminometer [79] and it is designed in AMS SiGe 0.35 μm technology with an area of 4×4 mm^2. Each ASIC channel (figure A.1) consists of a preamplifier with a variable gain, two shapers (a slow one for the analog readout and a fast shaper for the digital output), a sample&hold circuit and a discriminator. The MAROC3 provides one multiplexed analog output and 64 digital ones at the same time. The multiplexed output (with a maximum clock frequency of 10 MHz) is digitized by an external ADC (AD9220, Analog Devices[2]) integrated on the frontend board, while the 64 fast shapers outputs are discriminated to generate 64 independent digital outputs (whose width is a function of the input amplitude). The frontend board is equipped with two FPGAs (ALTERA Cyclone II), for the configuration and readout of the MAROC3 ASIC.

[1] Laboratoire de l'accélérateur Linéaire, Orsay: *http://omega.in2p3.fr*
[2] Analog Devices Inc.; *www.analog.com*

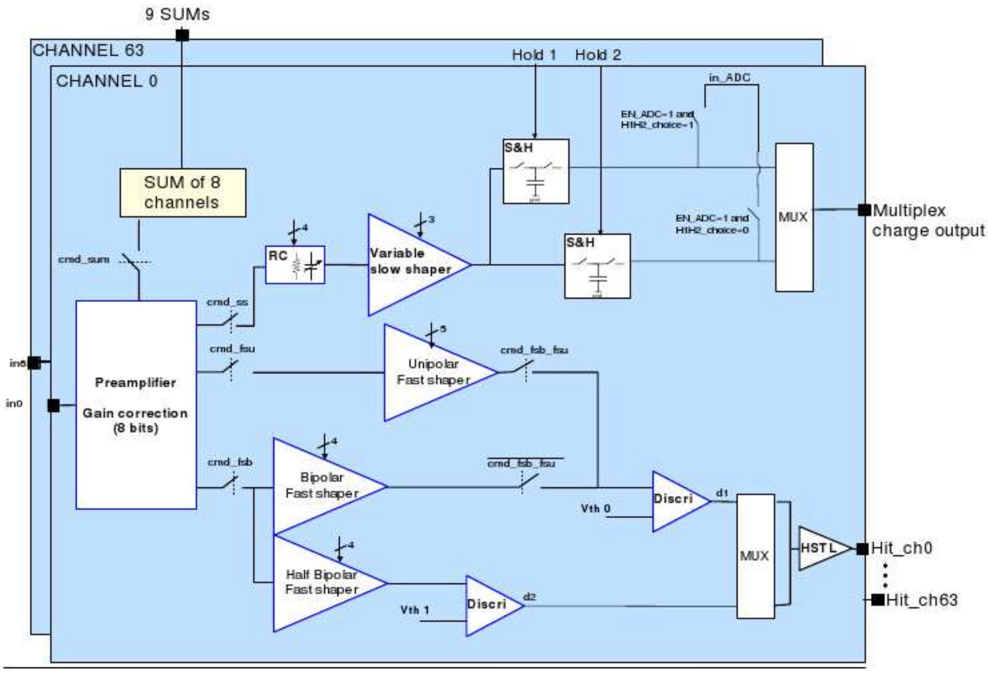

Figure A.1: Scheme of a single channel of the MAROC3 ASIC.

All the channel settings can be selected sending a string of 829 bits to the ASIC during the configuration phase. The bit list is summarized in table A.1

Bit	**Name**	**Description**
1-2	dummy	not used
3	slope DAC	change DAC0 slope
$4 \rightarrow 13$	DAC1 threshold	set the discriminator threshold
$14 \rightarrow 23$	DAC0 threshold	set the discriminator threshold
$24 \rightarrow 27$	ADC parameters	set the internal ADC features
$28 \rightarrow 155$	mask discriminator outputs	enable/disable digital outputs
$156 \rightarrow 190$	general parameters	select shaper and sample&hold circuit
$191 \rightarrow 198$	gain 64	select gain of channel number 64
199	sum 64	enable sum output channel number 63
$200 \rightarrow 765$	gain-sum	select gain and sum of the other 64 channels
$766 \rightarrow 829$	C-test all channels	enable the calibration input

Table A.1: The MAROC3 configuration bits.

Before the final assembly of the MAROC3 boards on the Large EMR Prototype, all the boards have been tested on bench in order to evaluate the ASIC performance and to check the functionalities of the boards themselves. In particular, the linearity of the 64 channels response and their uniformity have been measured both for the ASIC analog output and the digital ones. Finally, the behavior of the 10 MAROC3 boards (six for the prototype plus four spare ones) has been compared.

A.1.1 The Analog Part

The first test of the analog response consisted in the measurement of the ASIC channel noise by means of a pedestal run, which is a run acquired using a random trigger in order to evaluate the baseline of each channel as presented in figure A.2(a). Figures A.2(b) and A.2(c) show respectively the distributions of the pedestal and noise RMS extracted from the pedestal profile: both plots have been fitted with a gaussian function. The spread of the distributions, defined as the $sigma$ over $mean$ ratio, is 4.3‰ for the pedestal and about 2.9% for the noise RMS.

The main test of the analog output is the hold scan, which allows to evaluate the shape of the analog signal varying the “sample&hold” time. The hold is defined as the interval between a start signal (typically the trigger signal) and the sampling one: the idea is explained in figure A.3. The trigger signal is generated by a scintillator whose analog output is discriminated by a NIM discriminator (which requires a few tens of nanoseconds). This signal is processed by a VME trigger board whose output is the start of the hold delay. The scintillator light integrated by a PMT pad is amplified (by the preamplifier), shaped (by the slow shaper) and sampled (by the sample&hold circuit) in the MAROC3 ASIC. The sampling is performed at the time indicated by the hold signal: the sampled value is stored to be sent to the ADC during the readout procedure.

The tests have been performed using a calibration signal which consisted in square pulses with a frequency of 1 kHz and a variable amplitude (1 V, 750 mV and 500 mV). Given that the hold value should be set in order to sample the peak of the signal, the shape of the analog signal can be obtained varying the hold delay in the range 0-840 ns (thus sampling the signal in different places). The goal of these tests was to evaluate the linearity of the output of each single channel of the ASIC as a function of the input amplitude and the uniformity of the 64 MAROC3 channels.

Figure A.4(a) presents the hold scan for a single MAROC3 channel, where the peak has been fitted with a gaussian function.

For each channel, the peak amplitude (the $p0$ of the gaussian fit) has been plotted as a function of the amplitude of the input signal and fitted with a linear function (figure A.4(b)). This fit allowed to extract the offset (the $p0$ value of the fit which should be comparable with the pedestal one) and the gain (the slope of

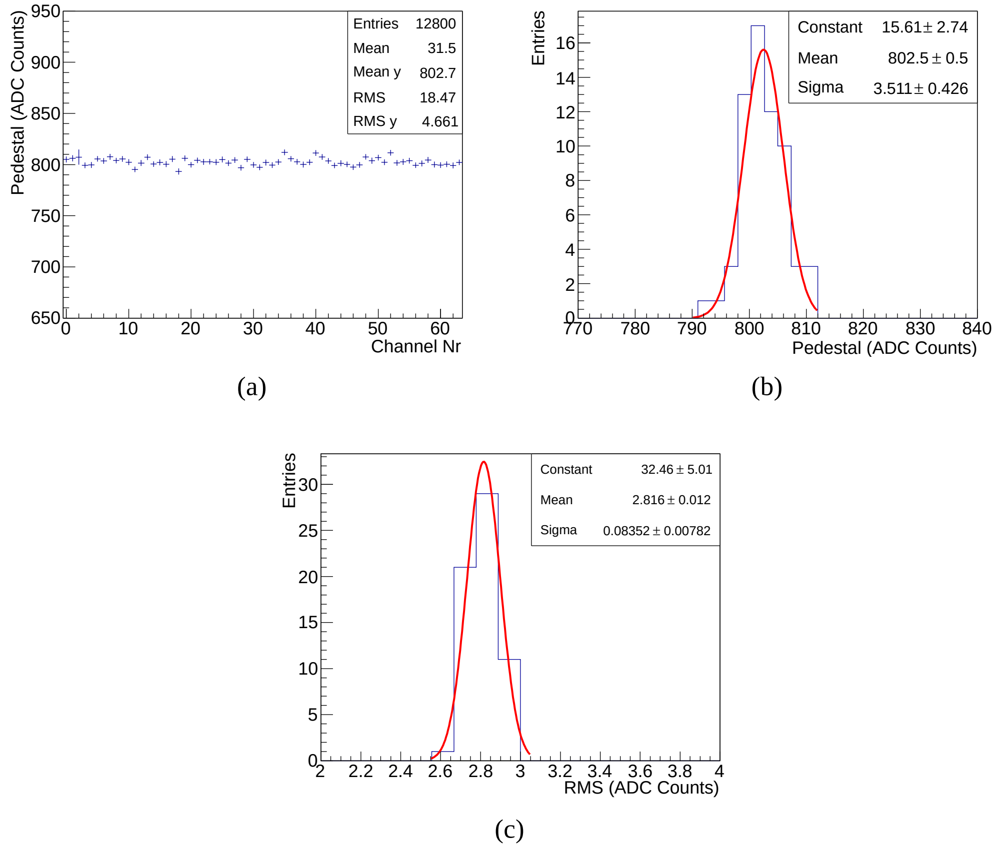

Figure A.2: a) The pedestal profile and the distributions of b) the pedestal and c) the noise RMS values for the 64 MAROC3 channels.

the line, that is the $p1$ value). The overall distributions of these two quantities are shown in figure A.5.

These distributions have been fitted with a gaussian function in order to measure the spread: as far as the offset is concerned, the channels are equal within 4‰ (as expected, a result comparable with the spread of the pedestal), while the spread of the gain distribution is about 3%. Also the mean value of the offset is comparable with the pedestal one (figure A.2(b)).

This procedure has been performed for the 10 MAROC3 boards in order to study their uniformity. As described before, the peaks amplitude of the hold scan have been plotted as a function of the input amplitude and fitted with a straight line. Figure A.6(a) presents the overall distribution of the offset: in this plot seven peaks are clearly visible since the signal baseline (or in other words the pedestal value) of the ASICs is different. Since in this way it is not possible to evaluate the boards uniformity, the peaks have been normalized to 1000 ADC, as shown

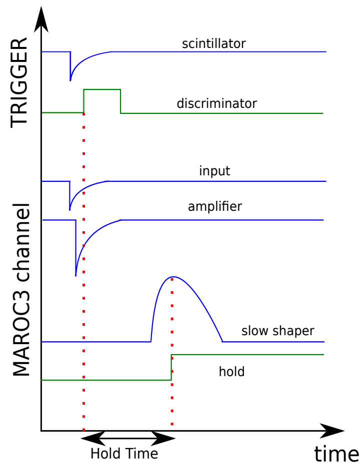

Figure A.3: Scheme of the hold principle: the blue lines represent the analog signals while the green lines the digital ones.

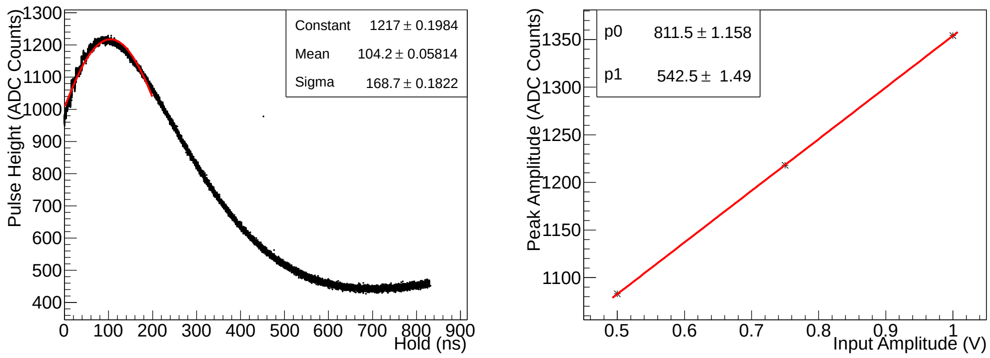

(a) (b)

Figure A.4: a) A MAROC3 channel hold scan performed with a square pulse with a frequency of 1 kHz and an amplitude of 1 V. b) The peak amplitude has been plotted as a function of the input amplitude. The offset and gain values have been extracted from the linear fit.

in figure A.6(b). At this point, the uniformity of the offset of the different boards channels is defined as the spread $\left(\text{the } \frac{sigma}{mean}\right)$ of this distribution and it corresponds to 0.7%.

The result obtained considering the gain of the 640 channels is comparable with the spread of the same distribution for a single board (figure A.5) as shown in figure A.7: the gain spread is about 4%.

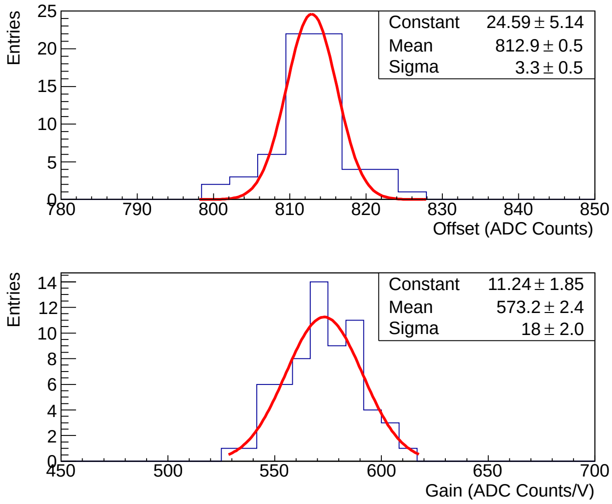

(a)

Figure A.5: a) The hold scan offset (top) and the gain (bottom) distributions for the 64 MAROC3 channels.

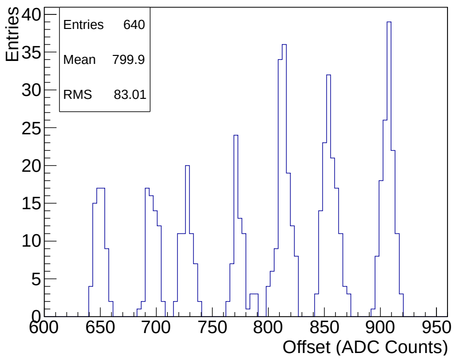

(a)

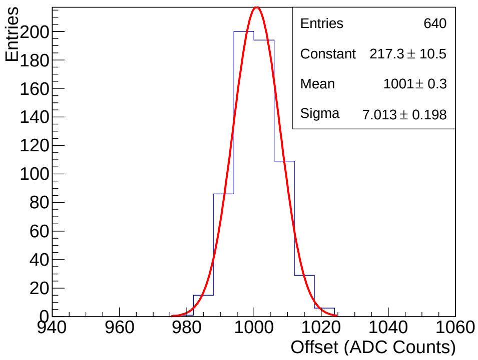

(b)

Figure A.6: The offset distribution of the ten MAROC3 boards under test a) before and b) after the normalization at 1000 ADC.

A.1.2 The Digital Part

The test of the MAROC3 digital part consists in the threshold scan: a calibration signal was sent to the 64 MAROC3 channels varying the discriminator threshold and measuring the corresponding counting rate. The input signals were square pulses with a frequency of 1 kHz and with three different amplitudes: 500 mV, 250 mV and 125 mV.

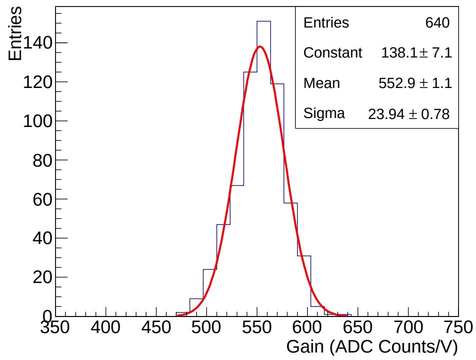

Figure A.7: The 10 MAROC3 boards gain distribution.

Figure A.8(a) explains the principle of the threshold scan: a square pulse is sent to the input capacitor, the injected charge is amplified, shaped and discriminated. The shaper output corresponds to a positive signal with an undershoot for the rising edge of the square pulse and a negative signal with an overshoot for the falling edge (an opposite charge is injected in this case).

Depending on the threshold value, the behavior of the ASIC is different:

- when the threshold is too small, the ASIC counts at a very high rate due mainly to the noise (green line);
- increasing the value of the threshold until the level of the blue line, the ASIC counts twice the number of pulses: one count corresponds to the positive signal of the rising edge and the other to the overshoot of the falling edge. In this case the counting rate is double;
- increasing the threshold (until the red line value), the ASIC counts the effective number of pulses and the counting rate is equal to the frequency of the input signal (1 kHz);
- when the threshold value is higher than the signal amplitude, the shaper signal never crosses the threshold and the system does not count.

An example of a threshold scan of one MAROC3 channel with a calibration signal of 500 mV is presented in figure A.8(b); the plot considers the counting rate instead of the effective number of pulses because the counting interval is generated via software and thus it is not precise.

The threshold scan has been fitted with a step function:

$$rate = p0 * \mathrm{erf}(-(x - p1) * p2) + p3 \tag{A.1}$$

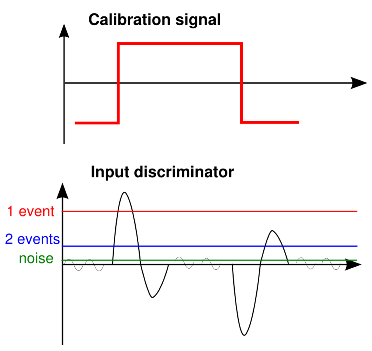

(a)

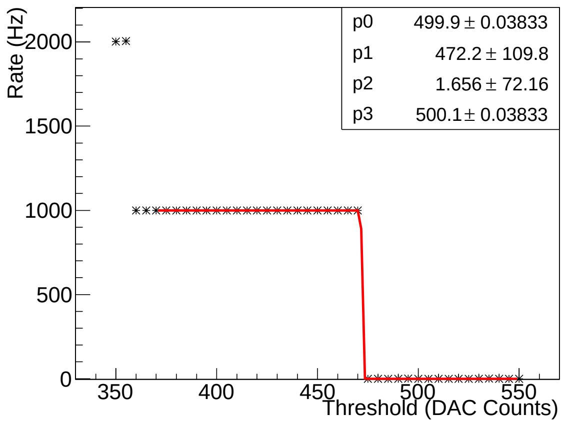

(b)

Figure A.8: a) The threshold scan principle. b) One channel threshold scan performed with a square pulse with a frequency of 1 kHz and an amplitude of 500 mV. The plot has been fitted with equation A.1.

where $erf()$ is the error function defined as

$$erf = \frac{2}{\sqrt{\pi}} \int_0^{\pi} e^{-t^2} dt \tag{A.2}$$

The parameters are defined in the following way: $p0$ is the function range and $p3$ the offset and in this case they are both equal to about 500 Hz; the $p1$ parameter is the position of the inflection of the curve (which represents the threshold value corresponding to the peak of the discriminator input signal), while $p2$ represents the slope of the linear part of the function.

The position of the inflection of the curve is a function of the calibration pulse amplitude as shown in figure A.9. The fit with a linear function allows to obtain the offset (the so called zero-threshold, that is the $p0$ parameter) and the gain (the slope of the line).

This procedure has been performed for the 64 MAROC3 channels: the overall distributions of the zero-threshold and the gain are presented in figure A.10: the offset distribution can be fitted with a gaussian function while the gain one has a long tail. One can conclude that as far as the zero-threshold is concerned the ASIC channels are equal within 0.9%. This is fundamental for the operation of the ASIC in the digital mode: if the zero of the threshold is the same for all the channels, setting one threshold value for all means being able to detect the same input amplitude. The tail of the gain distribution increases the gain spread to 14%.

Figure A.11 summarizes the behavior of the 64 ASIC channels: the zero-threshold is practically the same for all the channels, while the gain value de-

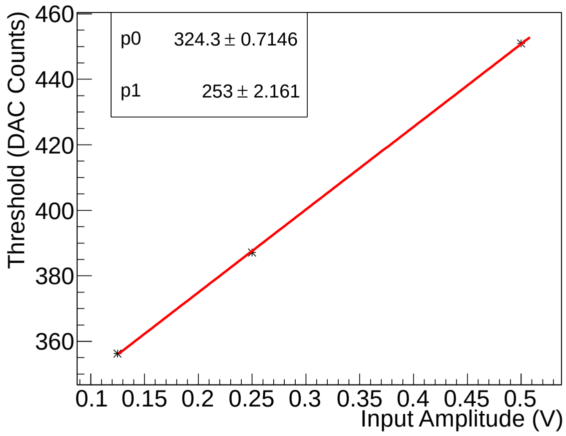

Figure A.9: The inflection position plotted as a function of the input amplitude: the zero-threshold and the gain parameters have been extracted from the linear fit.

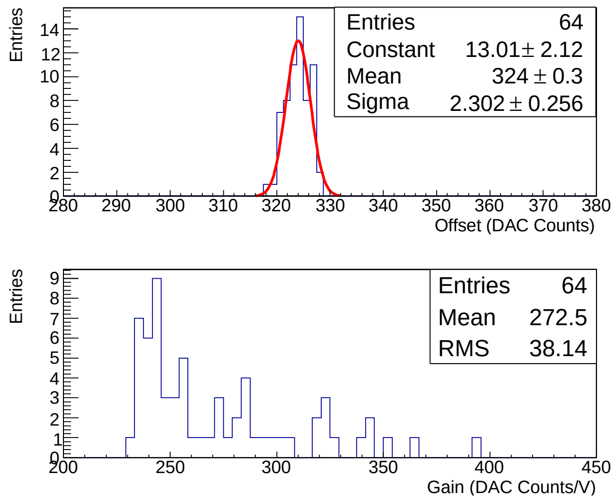

Figure A.10: The threshold scan offset (top) and gain (bottom) distributions for the 64 MAROC3 channels.

creases with the channel number which may indicate the presence of a systematic effect due to the way the discriminators are physically implemented in the ASIC.

As for the analog tests, also for the digital one the uniformity of the ten different boards response has been checked. Figure A.12(a) presents the zero-threshold values distribution: three peaks are clearly visible and they have been fitted with three gaussian functions. Considering the three peaks, the ten boards can be divided into 3 groups: the first and the second one are characterized by a spread of

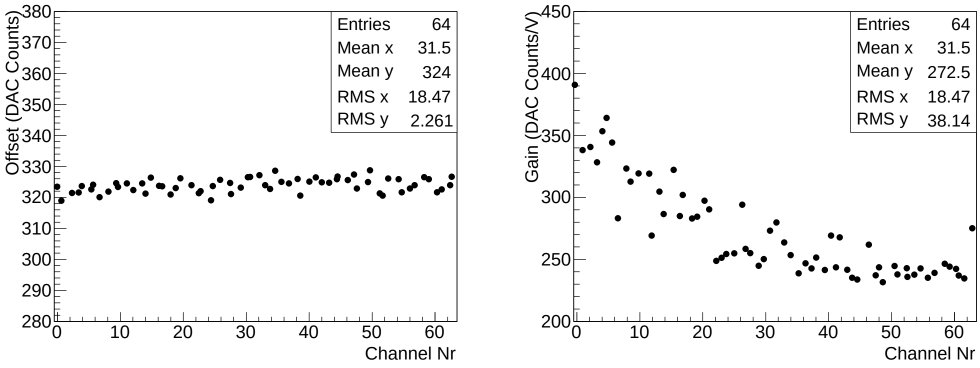

(a) (b)

Figure A.11: The different behavior of the MAROC3 channels in terms of a) zero-threshold and b) gain.

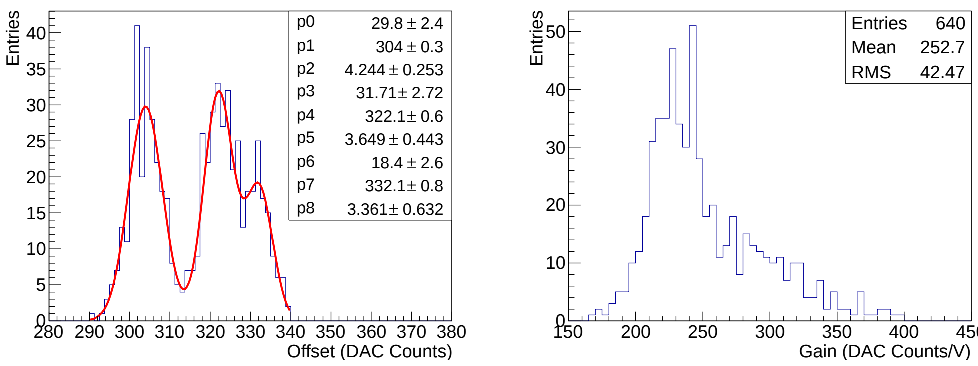

(a) (b)

Figure A.12: The distribution of the a) zero-threshold and the b) gain values for the 10 MAROC3 boards.

1.4% while the last one by a spread equal to 1%. Both these values are comparable with the result obtained with a single board.

Also the gain distribution (figure A.12(b)) is similar to the one obtained with a single board: the spread of the distribution is about 16.8%, because of the presence of a long tail for high gains.

List of acronyms

ADC	Analog to Digital Converter
APD	Avalanche PhotoDiode
ASACUSA	Atomic Spectroscopy and Collision Using Slow Antiprotons
ASCII	American Standard Code for Information Interchange
ASIC	Application Specific Integrated Circuit
ATLAS	A Toroidal LHC ApparatuS
BC	Beam Chamber
BGO	Bismuth Germanate
CERN	European Organization for Nuclear Research
CM	Common Mode
DAC	Digital to Analog Converter
DAQ	Data AcQuisition
DBB	Digitizer and Buffer Board
DCR	Dark Count Rate
DST	Data Summary Tape
EA	Electron Affinity
ECAL	Electromagnetic CALorimeter
EMA	Extra Mural Absorber
EMR	Electron Muon Ranger
FACTOR	Fiber Apparatus for Calorimetry and Tracking with Optoelectronic Read-out
FBK-irst	Fondazione Bruno Kessler
FEB	FrontEnd Board
FGD	Fine Grained Detector
FPGA	Field Programmable Gate Array

FWHM Full Width at Half Maximum

GM-APD Geiger-Mode Avalanche PhotoDiode

HCAL Hadron CALorimeter

ID Inner Detector
INFN Istituto Nazionale di Fisica Nucleare
INGRID Interactive Neutrino GRID
I/O Input/Output

J-PARC Japan Proton Accelerator Research Complex

LEP Large EMR Prototype

MAPMT Multi Anode PhotoMultiplier Tube
MAROC Multi Anode ReadOut Chip
MI Main Injection
MICE Muon Ionization Cooling Experiment
MINERνA Main INjector ExpeRiment for ν-A
MINOS Main Injector Neutrino Oscillation Search
MIP Minimum Ionizing Particle
MP Most Probable
MPPC Multi Pixel Photon Counter
MUSASHI Mono-energetic Ultra Slow Antiproton Source for High-precision Investigations

ND Near Detector
NIM Nuclear Instrumentation Module
NuMI Neutrino Main Injector

OD Outer Detector

particle ID particle IDentification
PAW Physics Analysis Workstation
PC Personal Computer
PCB Printed-Circuit Board
PDE Photon Detection Efficiency
PIN P-type Intrinsic N-type
PMMA PolyMethylMethAcrylate
PMT PhotoMultiplier Tube

PS	Proton Synchrotron
PQFP	Plastic Quad Flat Pack
PVC	PolyVinyl Chloride
PVT	PolyVinylToluene
P0D	Pi-Zero Detector
QE	Quantum Efficiency
RAL	Rutherford Appleton Laboratory
R&D	Research & Development
RF	Radio Frequency
RMS	Root Mean Squared
ROOT	Rapid Object-Oriented Technology
SiPM	Silicon PhotoMultiplier
SMRD	Side Muon Range Detector
SNR	Signal to Noise Ratio
SPAD	Single Photon Avalanche PhotoDiode
TDC	Time to Digital Converter
TPC	Time Projection Chamber
T2K	Tokai to Kamioka
TWICE	Techniques for Wide-Range Instrumentation in Calorimetry Experiments
UA1	Underground Area 1
UK	United Kingdom
UV	Ultra Violet
VME	Versa Module Eurocard
VRB	VME Readout Boards
WFD	WaveForm Digitizer
WLS	WaveLength Shifter

List of Figures

List of Tables

Bibliography

[1] G. F. Knoll, “Radiation Detection and Measurement”, John Wiley & Sons, 1989.

[2] W. Leo, “Techniques for Nuclear and Particle Physics Experiment”, Springer, 1994.

[3] S. Flyckt *et al.*, “Photomultiplier Tubes: Principles and Applications”, Philips Photonics, 2002.

[4] K. Iniewski, “Semiconductor Radiation Detector Systems”, CMOS Emerging Technologies, 2010.

[5] S. Sze, “Semiconductor Devices: Physics and Technology”, John Wiley & Sons, 2001.

[6] D. Renker, “Photosensors”, *Nucl. Instr. and Meth. in Phys. Res. A* 527: 15–20, 2004.

[7] K. H. Photonics, “Photomultiplier Tubes. Basics and Applications”, Hamamatsu Photonics K.K., 2006.

[8] A. Saleh, “Fundamentals of photonics”, Wiley, 2007.

[9] K. Nakamura., “Latest bialkali photocathode with ultra high sensitivity”, *Nucl. Instr. and Meth. in Phys. Res. A* 623: 276–278, 2010.

[10] W. Neumann, “Optical Spectroscopy with dispersive Spectrometers Basics - Building Blocks - Systems - Applications”, Weiler-Simmerberg, 2011.

[11] J. Liu, “Photonic Devices”, Cambridge University, 2005.

[12] Y. Yoshizawa *et al.*, “The latest vacuum photodetector”, *Nucl. Instr. and Meth. in Phys. Res. A* 387: 33–37, 1997.

[13] K. H. Photonics, “Photomultiplier Tubes: Construction and Operating Characteristics, Connections to External Circuits”, Hamamatsu Photonics K.K., 1998.

[14] P. Ranin *et al.*, “Study of the Influence of the Earth’s Magnetic Field on PMTs for Pierre-Auger Surface Detectors”, UCLA-Cosmic, 2001.

[15] R. Cizeron *et al.*, “Some results of PMT studies”, Technical Report LHCb-2000-052, CERN, 2000.

[16] N. Tagg, “Performance of Hamamatsu 64-anode photomultipliers for use with wavelengthshifting optical fibres”, *Nucl. Instr. and Meth. in Phys. Res. A* 539: 668–678, 2005.

[17] G. Lutz, “Semiconductor Radiation Detector”, Springer, 1999.

[18] J. I. Pankove, “Optical Processes in Semiconductors”, Dover, 1971.

[19] D. Renker, “New developments on photosensors for particle physics”, *Nucl. Instr. and Meth. in Phys. Res. A* 598: 207–212, 2009.

[20] D. Neamen, “Semiconductor Physics and Devices”, McGraw-Hill, 2002.

[21] N. Dinu *et al.*, “Development of the first prototypes of Silicon PhotoMultiplier (SiPM) at ITC-irst”, *Nucl. Instr. and Meth. in Phys. Res. A* 572: 422–426, 2007.

[22] C. Piemonte, “A new silicon photomultiplier structure for blue light detection”, *Nucl. Instr. and Meth. in Phys. Res. A* 568: 224–232, 2006.

[23] S. Cova, “Evolution and prospects for single-photon avalanche diodes and quenching circuit”, *J. Modern Optics* 51: 1267–1288, 2004.

[24] B. Dolgoshein, “Silicon photomultipliers in particle physics: Possibilities and limitation”, *Proceedings of the 42nd Workshop on Innovative Detectors for Supercolliders (Erice, Italy):* 442–456, 2003.

[25] G. Bondarenko *et al.*, “Limited geiger-mode microcell silicon photodiode: new results”, *Nucl. Instr. and Meth. in Phys. Res. A* 442: 187–192, 2000.

[26] V. Saveliev *et al.*, Advances in Optical and Photonic Devices, InTech, 2010.

[27] J. Swain *et al.*, “Multi-pixel geiger-mode avalanche photodiodes with high quantum efficiency and low excess noise factor”, *Nucl. Instr. and Meth. in Phys. Res. A* 567: 250–254, 2006.

[28] K. Yamamoto, “Newly developed semiconductor detectors by Hamamatsu”, *Proceedings of the International Workshop on New Photon Detectors PD07,* 4, 2007.

[29] B. Dolgoshein *et al.*, “Status report on silicon photomultiplier development and its applications”, *Nucl. Instr. and Meth. in Phys. Res. A* 563: 368–376, 2006.

[30] M. Ramilli, “Characterization of SiPM: temperature dependencies”, *In Nuclear Science Symposium Conference Record (Dresden, Germany),* 2008.

[31] A. Lacaita *et al.*, “On the bremsstrahlung origin of hot-carrier-induced photons in silicon devices”, *IEEE Trans. Electron Dev.* 40: 557–582, 1993.

[32] E. Garutti, “Silicon photomultipliers for high energy physics detectors”, *Journal of Instrumentation* 6: P10003, 2011.

[33] T. Matsumura, “Radiation damage to MPPCs by irradiation with protons”, *Proceedings of the International Workshop on New Photon Detectors PD07,* 33, 2007.

[34] T. Matsubara, “Radiation damage of MPPC by γ-ray irradiation with ^{60}Co”, *Proceedings of the International Workshop on New Photon Detectors PD07,* 32, 2007.

[35] J. B. Birks, “The Theory and Practice of Scintillation Counting”, Pergamon Press, 1964.

[36] R. C. Fernow, “Introduction to experimental particle physics”, Cambridge University Press, 1986.

[37] P. Lecoq *et al.*, “Inorganic Scintillators for Detector Systems: Physical Principles and Crystal Engineering”, Springer, 2006.

[38] C. van Eijk, “Inorganic scintillators in medical imaging detectors”, *Nucl. Instr. and Meth. in Phys. Res. A* 509: 17–25, 2003.

[39] M. Moszyski *et al.*, “Properties of CsF, a fast inorganic scintillator in energy and time spectroscopy”, *Nucl. Instr. and Meth.* 179: 271–276, 1981.

[40] F. Nessi Tedaldi, “Overview of $PbWO_4$ calorimeter in CMS”, *Nucl. Instr. and Meth. in Phys. Res. A* 408: 266–273, 1998.

[41] G. R. Yearwood, “Development of a high resolution tracking detector with SiPM readout”, Master’s thesis, RWTH Aachen University, 2007.

[42] V. L. Ermolaev *et al.*, “Non-radiative transitions as Forster’s energy transfer to solvent vibrations”, *Journal of Luminescence* 20: 387–395, 1979.

[43] C. Zorn *et al.*, “Preliminary study of radiation damage in liquid scintillators”, *IEEE Trans. Nucl. Sci.* 37: 487–491, 1993.

[44] BICRON, Scintillation Products: Organic scintillation Materials and Detectors, Saint-Gobain Crystals, 2011, *www.detectors.saint_gobain.com*.

[45] A. Pla-Dalmau *et al.*, “Low-cost extruded plastic scintillator”, *Nucl. Instr. and Meth. in Phys. Res. A* 466: 482–491, 2001.

[46] The MINERνa Collaboration, “Proposal to Perform a High-Statistics Neutrino Scattering Experiment Using a Fine-grained Detector in the NuMI Beam”, arXiv:hepex/0405002, 2004.

[47] J. C. Thevenin *et al.*, “Extruded polystyrene, a new scintillator”, *Nucl. Instr. and Meth. in Phys. Res. A* 169: 53–56, 1980.

[48] K. Abe *et al.*, “The T2K experiment”, *Nucl. Instr. and Meth. in Phys. Res. A* 659: 106–135, 2011.

[49] D. Barna *et al.*, “ASACUSA STATUS REPORT - ASACUSA progress during 2008 and plans for 2009”, Technical report, CERN-SPSC-2009-005, CERN, Geneva, 2009.

[50] D. Bolognini, “The MICE Electron Muon Ranger: a fundamental step towards a neutrino factory”, Ph.D. thesis, Università degli Studi dell’Insubria, 2012, *http://insulab.dfm.uninsubria.it/images/download_files/bolognini_thesis_phd.pdf*.

[51] A. Pla-Dalmau *et al.*, “Extruding Plastic Scintillator at Fermilab”, *In Nuclear Science Symposium Conference Record* volume 1: 102–104, 2003.

[52] Y. Xiaoguang, “A study of light collection efficiency in scintillation detectors”, *Nucl. Instr. and Meth. in Phys. Res. A* 228: 101–104, 1984.

[53] S. Zanoletti, “The Characterization of the ASACUSA CUSP-TRAP Tracker”, Master’s thesis, Università degli Studi dell’Insubria, 2011, *http://insulab.dfm.uninsubria.it/images/download_files/thesis_zanoletti.pdf*.

[54] T. O. White, “Scintillating fibres”, *Nucl. Instr. and Meth. in Phys. Res. A* 273: 820–825, 1988.

[55] V. Cavasinni, “A method to study light attenuation effects in wavelength shifting fibres”, *Nucl. Instr. and Meth. in Phys. Res. A* 517: 128–138, 2004.

[56] B. Baumbaugh *et al.*, “Performance of multiclad scintillating and clear waveguide fibers read out with visible light photon counters”, *Nucl. Instr. and Meth. in Phys. Res. A* 345: 271–278, 1994.

[57] T. Kafka *et al.*, “Prospects and status of the MINERA experiment at FNAL”, *Progress in Particle and Nuclear Physics* 64: 181–183, 2010.

[58] V. Mascagna, “A scintillating bar tracking detector for the ASACUSA - ‘trap group’ experiment at the CERN AD”, *Proceedings of the 11th Conference of Astroparticle, Particle and Space Physics, Detectors and Medical Physics Applications (Como, Italy):* 90–95, 2009.

[59] Y. Kudenko, “The near neutrino detector for the T2K experiment”, *Nucl. Instr. and Meth. in Phys. Res. A* 598: 289 – 295, 2009.

[60] T. Kafka, “MINOS experiment at Fermilab”, *Progress in Particle and Nuclear Physics* 64: 184–186, 2010.

[61] J. G. Morfn, “MINERνA: A High-Statistics Neutrino Scattering Experiment using a Fine-Grained Detector in the NuMI Beam”, *Nucl. Phys. B* 143: 139–143, 2005.

[62] S. Fukuda *et al.*, “The SuperKamiokande Detector”, *Nucl. Instr. and Meth. in Phys. Res. A* 501: 418–462, 2003.

[63] M. Otani *et al.*, “Design and construction of INGRID neutrino beam monitor for T2K neutrino experiment”, *Nucl. Instr. and Meth. in Phys. Res. A* 623: 368–370, 2010.

[64] H. Maesaka, “The K2K SciBar Detector”, *Nucl. Phys. B* 139: 289–294, 2005.

[65] M. Yokoyama, “Mass production test of Hamamatsu MPPC for T2K neutrino oscillation experiment”, *Nucl. Instr. and Meth. in Phys. Res. A* 610: 362–365, 2009.

[66] FACTOR Collaboration, *http://webint.ts.infn.it/en/research/exp/factor.html*.

[67] D. Lietti *at al.*, “The prototype of the MICE Electron-Muon Ranger: Design, construction and test”, *Nucl. Instr. and Meth. in Phys. Res. A* 604: 314–318, 2009.

[68] MICE Collaboration, "An International Muon Ionization Cooling Experiment (MICE)", *Proposal to the Rutherford Appleton Laboratory*, 2003.

[69] D. Neuffer, "Introduction to muon cooling", *Nucl. Instr. and Meth. in Phys. Res. A* 532: 26–31, 2004.

[70] M Adinolfi *et al.*, "The KLOE electromagnetic calorimeter", *Nucl. Instr. and Meth. in Phys. Res. A* 482: 364–386, 2002.

[71] D. Orestano, "The detector system of the MICE experiment", *Nucl. Instr. and Meth. in Phys. Res. A* 617: 45–47, 2010.

[72] D. Lietti, "The Electron Muon Ranger for the MICE Experiment", Master's thesis, Università degli Studi dell'Insubria, 2010, *http://insulab.dfm.uninsubria.it/images/download_file/thesis_master_lietti.pdf*.

[73] A. Berra, "MICRO: un mini osservatorio per raggi cosmici", 2005, *http://insulab.dfm.uninsubria.it/images/download_files/tesi_triennale_berra.pdf*.

[74] M. Prest *et al.*, "The AGILE silicon tracker: an innovative γ-ray instrument for space", *Nucl. Instr. and Meth. in Phys. Res. A* 501: 280–287, 2003.

[75] B. Welch *et al.*, "Practical Programming in Tcl and Tk", Prentice Hall PTR, 2003.

[76] S. Rabaioli *et al.*, "Silicon photomultipliers for scintillating trackers", *in press on Nucl. Instr. and Meth. in Phys. Res. A* 2012.

[77] L. Durieu *et al.*, "Optics studies for the T9 beam line in the CERN PS East Area secondary beam facility", CERN-PS-2001-037-AE, 2001.

[78] D. Bolognini *et al.*, "Tests of the MICE Electron Muon Ranger frontend electronics with a small scale prototype", *Nucl. Instr. and Meth. in Phys. Res. A* 646: 108–117, 2011.

[79] S. Franz *et al.*, "ATLAS ALFA measuring absolute luminosity with scintillating fibres", *Nucl. Instr. and Meth. in Phys. Res. A* 610: 35–40, 2009.

Ringraziamenti

Ed eccoci arrivati ai ringraziamenti, che come tutti sanno (ed hanno già scritto) sono le pagine più attese e più lette di tutta la tesi. Devo dire grazie a tutte quelle persone che mi sono state accanto anche quando mi sembrava impossibile riuscire a raggiungere questo obiettivo e che mi hanno incoraggiata e spronata ad andare avanti. Ed ora direi che è proprio giunto il momento di iniziare.

Sicuramente il primo grazie lo devo dedicare al mio relatore, la Dr.ssa Michela Prest, e al Dr. Erik Vallazza (che ormai anche per me sono diventati semplicemente Michela ed Erik). Michela ti ringrazio profondamente per la disponibilità e la pazienza che hai avuto nei miei confronti, per aver letto e riletto infinite volte la tesi e per aver reso quella che all'inizio era una lingua strana e sconosciuta un bell'inglese corretto.

A questo punto devo dire grazie anche a te, Berra, che sei stato il mio correlatore. Grazie perchè non ti sei limitato a darmi consigli per superare i problemi con l'analisi o per capire cosa stesse succedendo a quei "dannati" SiPM, sei stato anche un amico con cui scherzare e ridere. E ti prometto che prima o poi ti inviterò per una bella mangiata di cotolette dalla mia nonna. Grazie anche a Federica, Daniela, Silvia ed Elena per tutti i momenti trascorsi insieme in laboratorio.

Anche se so che non riuscirò mai a trovare le parole giuste, un grazie immenso va alla mia famiglia. La prima che devo ringraziare è la mia mamma, perchè sei una mamma (ormai nonna) speciale sempre pronta ad accettare ogni mia decisione e a sopportare il mio brutto carattere (anche se ultimamente me lo ripeti un po' troppo spesso) e i miei sbalzi d'umore. Grazie a mio papà e a mio fratello perchè so che sono molto orgogliosi di me e grazie anche a mia nonna che in questi sei anni di università mi ha evitato di dover mangiare davanti ad un PC preparandomi ogni giorno un pranzetto diverso (nonna è colpa tua se sono ingrassata). Grazie anche a Roberta e a Yvonne a cui ho sempre raccontato quello che facevo in laboratorio e al CERN. Infine, ringrazio la *new entry* della nostra famiglia, la mia bellissima nipotina Iris (ed anche la tua mamma per averti fatto così fantastica) perchè con i tuoi musini, i tuoi benoni e i tuoi bacini sei riuscita a trasmettermi una gioia immensa.

Un ringraziamento speciale lo devo anche voi Antonella, Gianni, zia Manu, Eleonora, Andrea e nonna Francesca che in questi anni siete stati come una seconda famiglia. Grazie per i consigli, per le parole di incoraggiamento, ma soprattutto grazie per le grigliatine estive.

E come ho già fatto l'altra volta, l'ultimo grazie lo dedico alla persona più importante: questo **GRAZIE** è per te, amore mio. Grazie perchè in questi anni non sei stato semplicemente il mio moroso: a volte sei stato il mio capo (con grande fatica di entrambi, soprattutto mia, e relativi litigi) ed altre un aiuto indispensabile ed una spalla su cui piangere. Ti dedico questa tesi perchè senza di te non ce l'avrei mai fatta e soprattutto perchè mi sei sempre stato accanto sopportando tutti i miei sfoghi e i miei capricci. Purtroppo so che non riuscirò mai a trovare le parole giuste per ringraziarti, posso solo dirti grazie amore mio per essere come sei!